Computer Vision-Guided Virtual Craniofacial Surgery

by

Ananda S. Chowdhury

(Under the direction of Suchendra M. Bhandarkar)

Abstract

Craniofacial fractures are very frequent in the present society, the major causes being gunshot wounds, motor vehicle accidents and sports related injuries. The surgical reconstruction is challenging because the surgeons have to accurately register the broken fragments within a limited amount of time. Detection of the fractures, the other integral component of any surgical process, often becomes difficult because of the fracture pattern, intensity inhomogeneity, and noise.

In this thesis we explore the reconstruction and detection of craniofacial fractures using computer vision. Within the broad class of craniofacial fractures, our emphasis is on mandibular fractures. A typical input for us is a sequence of Computed Tomography (CT) images of a fractured human mandible. In chapter 1, we discuss in detail the overall significance of our work and the lay-out of this thesis. Chapter 2 is devoted to different aspects of virtual single fracture reconstruction, including the use of bipartite graph matching for establishment of correspondence in the Iterative Closest Point (ICP) algorithm, various means of improving the registration error from the ICP algorithm, exploration of anatomical symmetry and biomechanical stability of the human mandible in the reconstruction process, *etc.* In Chapter 3, the problem of virtual multi-fracture reconstruction, which resembles the assembly of a 3D jigsaw puzzle, is shown to have an worst case exponential time complexity. The problem is modeled as one of maximum weight graph matching, which even in the worst case, runs in polynomial time.

Chapter 4 discusses the hairline/minor fracture detection and target pattern generation in a hierarchical Bayesian restoration framework. We use the Markov Random Field (MRF)-Maximum A Posteriori (MAP) approach of Geman and Geman and model the fracture as a local stochastic degradation of an hypothetical intact mandible. The MAP estimate corresponds to the target pattern (reconstructed jaw) and the differences in intensity between the input data and MAP estimate at specific pixel locations mark the occurrence of a fracture. In Chapter 5, we apply traditional scale-space theory for corner detection, followed by Kalman filter within a Bayesian inference paradigm to identify well-displaced/major fracture points. Bayesian credible sets are constructed to establish a spatial consistency check among the 2D corners/fracture points, already identified using the scale space theory. In chapter 6, a fracture is modeled as a minimum cut in an appropriate weighted network. Ford-Fulkerson's algorithm is employed to obtain the minimum cut and the magnitude of the flow is used as an approximate estimate of the extent of the fracture. Chapter 7 summarizes our overall contributions and discusses directions for future research.

INDEX WORDS: Computer Vision, Graph Matching, Max Flow -Min Cut,
Graph Automorphism, Bayesian Inference, Markov Random Field,
Computed Tomography, Virtual Reconstruction, Fracture Detection.

Computer Vision-Guided Virtual Craniofacial Surgery

by

Ananda S. Chowdhury

B.Sc., Presidency College, University of Calcutta, 1996

B.Tech., Institute of Radiophysics and Electronics, University of Calcutta, 1999

M.E., Jadavpur University, 2001

A Thesis Submitted to the Graduate Faculty

of The University of Georgia in Partial Fulfillment

of the

Requirements for the Degree

Doctor of Philosophy

Athens, Georgia

2007

Computer Vision-Guided Virtual Craniofacial Surgery

by

Ananda S. Chowdhury

Approved:

Major Professor: Suchendra M. Bhandarkar

Committee: Robert W. Robinson
Hamid R. Arabnia
Khaled Rasheed
Gauri S. Datta
Ernest W. Tollner

Electronic Version Approved:

Maureen Grasso
Dean of the Graduate School
The University of Georgia
August 2007

Dedication

To my parents, whose blessings are my inspiration ...

Acknowledgments

First and foremost, I would like to express my sincere thanks to my advisor, Professor Suchendra Bhandarkar. His excellent guidance and constant enthusiasm played the most significant role in shaping my dissertation. In addition, the financial support, he provided from his research grants, in form of Research Assistantships (RA-ships) and travel money (for presenting our research in international conferences) were extremely useful. RA-ships enabled me to spend significantly more time on my research. The visit to premier conferences gives an opportunity to meet internationally acclaimed researchers. In one such conference, I interacted with members of a research group at NIH (Bethesda, MD), which initiated the development for a post-doctoral fellowship over there.

I am very grateful to Professor Robert Robinson for his brilliant advice and suggestions, which played a key role in my doctoral research. I consider it as my lifetime experience to come across a person of such a high academic standard. It is with heartfelt joy, I mention that with Professor Robinson as a co-author (in more than one paper), I have now earned an *Erdös Number* : 2 for myself. Without his sincere involvement, various graph theoretic modelings in this thesis would not have been possible. My interactions with Professor Gauri Datta from the department of Statistics, had significant impacts. His guidance led to successful applications of different statistical concepts in this dissertation. The meetings with Professor Jack Yu from the Medical College of Georgia unfolded before me the surgical challenges. The sincere encouragement, which I received throughout my Ph.D. years, from Professor Hamid Arabnia, the present graduate coordinator of our department, deserves special mention. I would express my gratitude to Professor Ernest Tollner from the Biological and Agricultural Engineering department and Professor Khaled Rasheed for extending their help from time-to-time. I would also like to thank Professor Edmond Ritter and Professor Ramon Figueroa from the Medical College of Georgia for their involvement in my doctoral

research. I am also very grateful to Professor Bidyut Baran Chaudhuri of the Indian Statistical Institute, Professor Animesh Maitra of the Institute of Radiophysics and Electronics, Professor Jaya Sil of Bengal Engineering College and Professor Debopriya Shyam of Presidency College for their strong encouragement. The affection and support of Professor Amit Konar and Professor Anup Bandyopadhyay, both from Jadavpur University, are very inspirational.

The environment in the Visual and Parallel Computing Laboratory (VPCL), directed by Professor Bhandarkar was really great. The technical discussions with my past and present labmates Siddhartha Chattopadhyay, Yong Wei and Xingzhi Luo were very interesting. I would take this opportunity to thank Yarong Tang, a MS student in the department of Artificial Intelligence, who started the work on this research project. The department of Computer Science in the University of Georgia, as a whole, provided an excellent ambiance to pursue quality research. It is with great pleasure, I remember my interactions with past and present doctoral students like Gregory Baramidze, Jacob Martin, Semmy Purewal, Chris Bennet, Fred Maier, Pooya Shareghi, Aleman Boanerges, Junfeng Qu and Xiaochuan Yi. In addition, I sincerely acknowledge the help of the administrative and technical support staff in our department which include Nathan Steward, Jean Power, Claudia Sewell, Elizabeth Williams and Ken Powell.

As a doctoral student, one has probably very limited time and opportunity for social interactions. However, I have some fond memories of cordial social evenings in Professor Datta's and Professor Bhandarkar's residences. I like to thank Baishali-di (wife of Professor Datta), Mashima (Baishali-di's mother) and Swati-di (wife of Professor Bhandarkar) for making Athens a home away from home for me. My interactions with Deeya (daughter of Professor Datta), Pranab and Asha (son and daughter of Professor Bhandarkar) have been amazing. I spent enjoyable time in company of Dipankar-Mridula, Archan and Susanta. During one full semester, I almost stopped cooking and enjoyed delicious food in Dipankar-Mridula's place. In addition to being a great friend and a co-author, Archan has been my guide in many non-academic domains which include cooking and driving. Susanta has been another great friend and having food and watching movies at his place is a great relaxation. Archan, Susanta and

I were involved in several great adda-s over the past one year. I enthusiastically remember my interactions at times with other friends in Athens like Hongyu, Sanjay, Siddhartha-Debjani, Shrirang, Gayathri, Hrushikesh, Ravi, Irfan, Desale, Umashanger-Rubi, Debdatta and Dalia. I also fondly recall the long and spirited phone conversations with Samaresh, Yoshodeep, Bhaskar-da, Partha-da and Nilanjan-da. Enthusiasm and support of Senjuti at various times during the Ph.D. years were very refreshing.

My doctoral research would not have been possible without the support and love, I enjoyed from my family and friends in India. My father Satyabrata Chowdhury taught Physics at St. Xaviers' College Calcutta and retired as the principal of Bangabasi Morning College, Calcutta. My mother Dr. Subarna Chowdhury retired as the Head of the Department of Sanskrit from Vidyasagar College for Women, Calcutta. The very fact that both of my parents were in academia, had a huge influence on my decision of choosing academics as a career option. Their blessings remain the most valuable inspiration for my life. My younger brother Subha has always taken more social responsibility and actively supported me for doing a Ph.D. Abir, Debarshi, Subir, Joy, Satyaki, Biswadeep, Arijit, Jaydeb, Sagnik, Ranjan, my close friends from school and college/university days, have always encouraged me to pursue doctoral research. Academic achievements of Anirban and Krishanu, two school-friends of mine, were big sources of motivation. Enthusiasm shown by Pinaki, a childhood friend in my locality, who himself doesn't have any formal academic degree, has also made a great impact. The support from Amit-da, my music teacher and Sahana-di, his wife is tremendous. Last but not the least, I would like to express sincere thanks to Anindita, my *fiancée*, for being extremely patient with my idiosyncrasies and providing me her wonderful support and encouragement.

Table of Contents

List of Figures

List of Tables

Chapter 1

Introduction

1.1 Motivation

Craniofacial fractures are very frequently encountered in the modern society, the principal reasons being gunshot wounds, motor vehicle accidents and sports related injuries [1]. Ogundare *et al.* [2] in their research illustrated that the fracture patterns sometimes imply a single fracture, and, in some other cases, there can be a combination of single fractures. As shown by Zahl *et al.* [3], the cost of surgery becomes prohibitive, in addition to the patient's risk, with the increased operating time necessary to ensure an accurate reconstruction. This is especially true in complex situations with multiple fractures.

Bone is a unique structure found only among members of the Phylum Chordata. It is the only living material in the entire animal kingdom that possesses a compressive modulus in the range of $1.0 - 1.0 \times 10^{10}$ N/m^2 with a volumetric range from 10^{-9} m^3 to 10 m^3. Bone is the rigid element in the body which resists deformation, allows for transmission of forces and protects the internal organs. The craniofacial skeleton consists of high stress-bearing buttresses and low stress-bearing curve planes. When external loads are applied, the craniofacial skeleton undergoes strain. When the strain exceeds the ultimate strain limit, about 1.0×10^4 microstrains, failure occurs (e.g. see Pashley *et al.* [4]). The resulting loss of spatial continuity in the craniofacial skeleton is termed clinically as fracture which causes pain, disfigurement, and functional impairment due to the disruption of force transmission. However, unlike any man-made material, bone, being living tissue, is capable of healing. For this healing to occur, there are two cardinal requirements: sufficient blood supply and relative stability. In clinical treatment of fractures, the realignment of the fragments must be achieved prior to fracture healing. Improper realignment of the fragments results in malunion.

The younger the individual, the more robust the healing and remodeling potential and thus better the tolerance to malunion. In the case of the fracture of the upper and lower jaws, an inherent dilemma exists. Since the maxilla (upper jaw) and mandible (lower jaw) house the 32 permanent teeth, which must fit precisely in a particular orientation known as position of intercuspation, malunion is very poorly tolerated. In order to prevent malunion, extensive dissection must be done to visualize all the fractures. However, the resulting stripping of the periosteum inevitably reduces the amount of blood flow to the bone fragments. Due to the three-dimensional (3D) geometry of the masticatory system, a 1^o angular mal-alignment in the anterior region of the mandible typically results in an $8-10\ mm$ transverse displacement in the area of the secondary molars. This transverse displacement severely disrupts the intercuspation and constitutes a dreaded post-operative condition known as malocclusion. In some extreme cases of malocclusion, the mandibular width can be so altered that the condyles are no longer within the glenoid fossas of the temporal mandibular joints thus severely disrupting the masticatory function.

1.2 Literature review and overall contribution

While there exists recent work published in the literature dealing with simulation of mandibular fractures ([5], [6]), and simulation of dental implantalogy ([7]) there is little reported, in recent years, by way of automated computer-aided surgical reconstruction of the craniofacial skeleton and detection of craniofacial fractures. There has been some recent progress in the design of thoracolumbosacral orthosis braces for postoperative patients needing back correction and/or support using computed tomography (CT)/ Magnetic Resonance (MR) images of the spinal region ([8]). Computer-aided surgical planning has also been explored in the context of orthopedic surgery ([9], [10], [11]) and rhinoplasty ([12]). Previous research in surgical planning using computer visualization in the context of oral, maxillofacial, craniofacial, orthodontic or orthgnathic surgery includes the works of Ayoub *et al.* [13], Gerbo *et al.* [14] and Hassfeld *et al.* [15]. Patel *et al.* [16] have examined the issues involved in computer-assisted craniofacial surgical planning and simulation using CT,

computer visualization and graphical simulation techniques. They discussed a quantitative assessment of craniofacial surgical simulation where the surgical procedures are carried out on cadavers, both in physical reality and in silico. The CT reconstruction after physical surgery is compared with that resulting from virtual surgery using volume registration methods and quantitative error metrics. The surgical procedures are performed on the cranial region and not the mandibular region which is the focus of the proposed research. Verstreken *et al.* [17] discussed a preoperative planning system for oral implant surgery which takes as input CT images of the upper and lower jaws. Hilger *et al.* [18] have investigated the modeling of craniofacial bone growth using generative models for the temporal shape and size of the human mandible that are mapped into Procrustes tangent space. Cevidanes *et al.* [19] described image processing methods for the computation of morphometric changes associated with jaw surgery, precisely locating jaw displacements and quantitatively describing the vectors of displacement. Enciso *et al.* [20] and Mollemans *et al.* [21] have examined issues pertaining to soft tissue modeling and simulation of jaw motion in the context of craniofacial surgery. The multi-disciplinary research team of Jamison, Goldwasser and Grosser at the Beckman Institute for Advanced Science and Technology, University of Illinois - Urbana-Champaign has investigated an alternative approach to bone replacement in the context of reconstructive craniofacial surgery (see [22]). An integrated workflow from the surgeon to the 3D craniofacial modeler to the implant fabricator has been developed that yields a perfectly fitting custom implant. The feasibility of this approach in a real clinical setting has also been demonstrated. However, the focus of this project is on the material science aspect of implant fabrication rather than on automation of the craniofacial reconstruction using machine vision and machine learning techniques. The research group of Stephanides *et al.* [23] at the Stanford University Medical Center has investigated the development of a virtual reality environment for surgical planning in the context of craniofacial and mandibular reconstruction. A realistic 3D virtual environment that models the soft tissue and skeletal structure from CT scans of the patient has been developed. The virtual reality surgical environment is designed to allow the surgeon to better understand the problem and perform the proposed procedure. This system was tested on a group of select patients with

difficult congenital malformations. The system is designed to be purely interactive with no automation of the craniofacial reconstruction procedures using machine vision and machine learning techniques. The research group of Farag *et al.* [24] at the University of Louisville, Kentucky has developed software for construction of a 3D volumetric model of the human mandible using CT scans. The emphasis of the project is on design of dental crowns and dental implants and not on craniofacial reconstruction. The relative paucity of existing work reinforces our thesis that the proposed research is at the cutting edge of Computer-assisted Surgical Planning.

A recent report by the American Medical Association predicts that the major breakthroughs in the field of surgery in the first half of the 21^{st} century will result from surgical robotization and automation [25]. Our overall goal is to develop an enabling technology that leverages the advances in computer vision, graph theory, and statistics for the purpose of virtual (in silico) craniofacial reconstructive surgery. The final outcome of the proposed research is an interactive graphical software to be used as a decision support system for pre-surgical planning as well as a training tool for surgery residents. The input to the software is a series of CT images showing a fractured craniofacial skeleton. The output of the software is a virtual reconstruction of the craniofacial skeleton along with proper detection of the fracture. This research would also constitute the necessary preliminary step towards defect-directed bone substitution by tissue-engineered constructs. The principal advantages of the proposed research include:

1. help surgeons to visualize the end product i.e. the reconstructed jaw before the actual surgery

2. several-fold reduction in the time required in the operating room, especially in case of multiple fractures

3. increased accuracy of fracture reduction

4. semi-automated detection of fractures in presence of intensity inhomogeneity and noise

1.3 Organization of this thesis

The thesis consists of a total of seven chapters and one appendix. Our focus throughout this research is on mandibular fractures within the broad spectrum of craniofacial fractures. The two main directions of this thesis are *virtual reconstruction* and *computer aided detection*. Five chapters are dedicated towards the above themes. Each of these five chapters, in addition to the present one, has a separate bibliography. It is relevant to mention that the references in the present chapter are mostly from the medical science discipline. On the contrary, the literature review for the next five chapters are mostly from the areas of computer vision, graph theory and statistics with applications in the area of medical imaging.

The second and third chapters are respectively devoted to *single-fracture reconstruction* and *multi-fracture reconstruction*. In the second chapter, we discuss various surface matching algorithms like the *Iterative Closest Point (ICP)*, the *Data Aligned Rigidity Constrained Exhaustive Search (DARCES)* and explore *anatomical symmetry* and *biomechanical stability* of the human mandible. The work in the chapter spans diverse disciplines like *Maximum Cardinality Minimum Weight Bipartite Graph Matching* algorithm, concepts from *Graph Automorpism*, *Fuzzy set-theoretic* modeling and extraction of *Mean and Gaussian curvature*. The third chapter is about *in silico* reconstruction from multiple fractures. This reconstruction problem is essentially a 3D jigsaw puzzle and is efficiently solved using *Hausdorff distance* and *Contour Curvature* based score matrix, the *Maximum Weight Graph Matching* algorithm and *Tanimoto Coefficient* based volumetric matching.

The next three chapters describe various techniques for semi-automatic detection of mandibular fractures. The fourth chapter discusses a *Markov Random Field - Maximum A Posteriori (MRF-MAP)* based unified approach for detection of *hairline* or *minor* fractures and generation of target pattern (reconstructed jaw) in such cases. The term hairline fracture or minor fracture refers to those situations where the broken bone fragments are not visibly out of alignment. In the presence of noise, the detection and subsequent visualization of hairline fractures becomes a clinically challenging task. Furthermore, the decision regarding surgical intervention for this type of fracture is less clear as a surgeon can rely

on natural bone healing. In addition to the detection and visualization, the target pattern depicts how a jaw with a hairline fracture would appear if allowed to heal naturally without explicit surgical intervention. In the fifth chapter, we propose a scheme for identification of stable fracture points, for *well-displaced* or *major* fractures in a given CT image sequence. Basic ideas from discrete curvature scale-space theory are used in the first phase to identify a set of candidate fracture points in the individual 2D CT slices. The conventional *Kalman filter* is modeled as a *Bayesian inference* problem and used for testing the consistency of the candidate fracture points across all the CT slices constituting the image sequence of interest. The sixth chapter, which is still an ongoing project, deals with *Graph Cut* based approach for simultaneous detection and classification of fractures. A fracture is essentially a cut in the bone structure. This very fact motivated us to employ the *Maximum Flow-Minimum Cut* algorithm for detection of a fracture. A cut corresponds to a fracture while the extent of the cut can very well determine the nature of the fracture e.g. major or minor.

The thesis is ended in the seventh chapter with a conclusion and a scope of future research. In the appendix, we illustrate the design and functionalities of a Graphical User Interface (GUI), named as *InsilicoSurgeon*. The GUI has several buttons where each button performs a dedicated task. This interactive graphical software will be used by the surgeons for training as well as planning purposes.

1.4 References

[1] R.E. King, J.M. Scianna and G.J. Petruzzelli, "Mandible Fracture Patterns: a Suburban Trauma Center Experience", *Am. J. Otolaryngol.*, 25(5), pp. 301-307, Sep.-Oct. 2004.

[2] B.O. Ogundare, A. Bonnick and N. Bayley, "Pattern of Mandibular Fractures in an Urban Major Trauma Center", *J. Oral and Maxillofac. Surg.*, 61(6), pp. 713-718, June 2003.

[3] C. Zahl, D. Muller, S. Felder and K.L. Gerlach, "Cost of miniplate osteosynthesis for treatment of mandibular fractures: a prospective evaluation", *Gesundheitswesen*, 65(10), pp. 561-565, 2003.

[4] D.H. Pashley, J.L. Borke and J.C. Yu, "Biomechanics and craniofacial morphogenesis", *Craniofacial surgery - Science and surgical technique*, (Lin, K.Y., Ogle R.C., and Jane, J.A. eds.), W. B. Saunders Co., Philadelphia, PA, pp. 84-100, 2002.

[5] T. Kurihara, "The fourth dimension in simulation surgery for craniofacial surgical procedures", *Keio J. Medicine*, 50(2), pp. 155-165, Mar. 2001.

[6] H. Nakajima , T. Kaneko, T. Kurihara and T. Fujino, "Craniofacial surgical simulation in the 3-dimensional CT SurgiPlan system", *Keio J. Medicine*, 50(2), pp. 95-102, Mar. 2001.

[7] M. Siessegger, B.T. Schneider, R.A. Mischkowski, F. Lazar, B. Krug, B. Klesper and J.E. Zoller, "Use of an image-guided navigation system in dental implant surgery in anatomically complex operation sites", *J. Craniomaxillofac. Surg.*, 29(5), pp. 276-281, Oct. 2001.

[8] H. Eldeeb , N. Boubekri, S. Asfour, T. Khalil and A. Finnieston, "Design of Thoracolumbosacral orthosis (TLSO) braces using CT/MR", *J. Comput. Assist. Tomogr.*, 25(6), pp. 963-970, Nov./Dec. 2001.

[9] J.E. Bechtold and S.H. Powless, "The application of computer graphics in foot and ankle surgical planning and reconstruction", *Clin. Podiatr. Med. Surg.*, 10, pp. 551-562, 1993.

[10] C.J. Sutherland, S.J. Bresina and D.E. Gayou, "Use of general purpose mechanical computer assisted engineering software in orthopaedic surgical planning: advantages and limitations", *Comput. Med. Imaging Graph.*, 18, pp. 435-442, 1994.

[11] E.Y.S. Chao and F.H. Sim, "Computer-aided preoperative planning in knee osteotomy", *Iowa Orthop. J.*, 15, pp. 4-18, 1995.

[12] H.S. Byrd and P.C. Hobar, "Rhinoplasty: a practical quide for surgical planning", *Plastic Reconstr. Surg.*, 91, pp. 642 - 654, 1993.

[13] A.F. Ayoub, D. Wray, K.F. Moos, P. Siebert, J. Jin, Nibbet T.B. C. Urquhart and P. Mowforth, "Three-dimensional modeling for modern diagnosis and planning in maxillo-facial surgery", *Intl. Jour. Adult Orthod. Orthognath. Surg.*, 11, pp. 225-233, 1996.

[14] L.R. Gerbo, D.R. Poulton, D.A. Covell and C.A. Russell, "A comparison of a computer-based orthognathic surgery prediction system to postsurgical results", *Intl. Jour. Adult Orthod. Orthognath. Surg.*, 12, pp. 55-63, 1997.

[15] S. Hassfeld, J. Zoller, F.K. Albert, C.R. Wirtz, M. Knauth and J. Muhling, "Preoperative planning and intraoperative navigation in skull base surgery", *J. Craniomaxillofac. Surg.*, 26, pp. 220-225, 1998.

[16] V.V. Patel, M.W. Vannier, J.L. Marsh and L.J. Lo, "Assessing Craniofacial Surgical Simulation", *IEEE Comput. Graph. Appl.*, 16(1), pp. 46-54, Jan. 1996.

[17] K. Verstreken, J. Van Cleynenbreugel, G. Marchal, I. Naert, P. Suetens and D. van Steenberghe, "Computer-assisted planning of oral implant surgery: A three-dimensional approach", *Intl. J. Oral Maxillofac. Implants*, 11, pp. 806-810, 1996.

[18] K.B. Hilger, R. Larsen and M. Wrobel, "Growth Modeling of Human Mandibles using Non-Euclidean Metrics", *Med. Image Anal.*, 7(4), pp. 425-433, Dec. 2003.

[19] L.H.S. Cevidanes, M. Styner, C. Phillips, A.E.F. Oliveira and J.F.C. Tulloch, "3D Morphometric Changes 1 Year After Jaw Surgery", *Proc. Fourth IEEE Symp. Biomedical Imaging (ISBI)*, pp. 1-4, Metro Washington, DC, 2007.

[20] R. Enciso, A. Memon, U. Neumann and J.Mah, "The Virtual Cranio-Facial Patient Project: 3D Modelling and Animation", *Proc. Eleventh 'Medicine Meets Virtual Reality' Conf.*, (J.D. Westwood, H.M. Hoffman, G.T. Mogel, R. Phillips, R.A. Robb and D. Stredney eds.) pp. 65-72, Newport Beach, USA, 2003.

[21] W. Mollemans, F. Schutyser, N. Nadjmi and P. Suetens, "Very fast soft tissue predictions with mass tensor model for maxillofacial surgery planning systems", *Proc. Ninth Annual Conf. Intl. Soc. for Comput. Aided Surg.*, pp. 491-496, 2005.

[22] R. Jamison, M. Goldwasser, B. Grosser, J. Sinn-Halnon and J. Cesarano, Beckman Institute for Advanced Science and Technology, University of Illinois, Urbana-Champaign, IL. http://www.itg.uiuc.edu/technology/reconstruction/index.htm.

[23] M. Stephanides, K. Montgomery, J.C. Latombe, J. Brown, S. Schendel and M. Ross, National Biocomputation Center, Stanford University Medical Center, Palo Alto, CA. http://biocomp.stanford.edu/projects/project_pages/CraniofacialPAGE.html, http://biocomp.stanford.edu/projects/project_pages/MandibularReconPAGE.html.

[24] A. Farag, H. Hassan, A. El-Baz, A. Ahmed and M. Miller, Computer Vision and Image Processing Laboratory, University of Louisville, KY. http://www.cvip.louisville.edu/wwwcvip/frames/mainFrames/Research.htm.

[25] M.J. Mack, "Minimally invasive and robotic surgery", *JAMA*, 285(5), pp. 568-572, Feb. 2001.

Chapter 2

Virtual Single-fracture Mandibular Reconstruction

2.1 Motivation

In this chapter, we focus on the various aspects of the single fracture reconstruction. In addition to exclusive single fracture cases, even in multiple fracture scenario, the fractures are fixated one at a time in the operating room. Thus, reconstruction from a single mandibular fracture assumes paramount importance in most cases. The plastic surgeon in the operating room restores the form and function of the fractured bone elements in the craniofacial skeleton typically by first exposing all the fragments, then returning them to their normal configuration, and finally maintaining these reduced bone pieces with rigid screws and plates. However, there are several critical and inherent limitations to this current, standard approach. To visualize the fragments in order to reduce them necessitates their exposure which consequently reduces the attached blood supply. To improve the blood supply, one can decrease the extent of dissection. However this means not being able to visualize the entire fracture, which could lead to potential misalignments of the bone fragments. Our proposed scheme can potentially bring down the operating time without sacrificing surgical precision. Thus, we can achieve significant reduction of operative and postoperative patient trauma and substantially decrease the cost of surgery.

2.2 Chapter Organization

The chapter is organized in the following way: in section 2.3, we discuss existing literature on craniofacial reconstruction along with some computer vision algorithms that can be applied for this purpose and highlight our contribution; in section 2.4, a series of image processing tasks are described; the next three sections 2.5, 2.6 and 2.7 are respectively devoted to three

algorithms namely ICP, DARCES and hybrid DARCES-ICP for matching of two fracture surfaces; in sections 2.8 and 2.9, we describe Mean and Gaussian curvature and fuzzy set based modeling of the existing irregularities in a fracture surface; section 2.10 shows some reward-penalty schemes to incorporate the surface irregularity information in the reconstruction paradigm to improve the surface matching error; the next three sections emphasize on improving the reconstruction from ICP algorithm by generation of multiple initial solutions (2.11), filtering out the best initial solution (2.12) and use that as a starting point for the ICP, which we call a hybrid Geometric-ICP algorithm (2.13); in section 2.14, we explore the bilateral symmetry of a human mandible; section 2.15 is on detailed analysis and modeling of the biomechanical stability of a human mandible; in the next section (2.16), the angular perturbation based second phase of the two-phase virtual reconstruction scheme is proposed; in the penultimate section (2.17), we describe experimental results and their analyses; finally the chapter ends in section 2.18 with conclusion and future scope of research.

2.3 Literature review and our contribution

There had been a lot of interesting research over the past decade in various aspects of craniofacial/maxillofacial surgery. The mass tensor model is used for fast soft tissue prediction in [1] whereas the mass- spring model is used for fast surgical simulation from CT data in [2]. The problem of building a virtual craniofacial patient from CT data has been addressed in [3] whereas a reconstruction approach involving complete 3D modeling of the solid high-detailed structure of the craniofacial skeleton, starting from the information present in the 3D diagnostic CT images can be found in [4]. A survey with detailed information about reconstruction of anatomic models from craniofacial image data can be found in [5]. The Iterative Closest Point (ICP) [6] algorithm is seen to be a popular computer vision algorithm for surface registration in the field of medical imaging [7]. Some variants of the ICP algorithm that incorporate certain statistical concepts such as Expectation Maximization (EM) in the context of medical imaging can be found in [8]. The basic benefit of the ICP algorithm is that it gives an accurate result given a good initial starting point. Another surface registra-

tion algorithm called the Data Aligned Rigidity Constrained Exhaustive Search (DARCES) which incorporates a Random Sample Consensus (RANSAC) model fitting approach [9], is popular because of its robustness to outliers and has also been used in medical imaging [10]. A two-stage general framework, based on block matching strategies is proposed in [11] for the purpose of robust rigid medical image registration.

The first contribution of this chapter lies in solving the 3D correspondence problem with the Maximum Cardinality Minimum Weight Bipartite Graph Matching algorithm. The second contribution is the proposition of the hybrid DARCES-ICP algorithm. The synergism between these two algorithms are exploited in three different ways. The synergetic combination of the two algorithms, where the output of the DARCES algorithm is fed as an input to the ICP algorithm, is observed to result in an improved surface matching algorithm with a considerable reduction in both, the mean squared error (MSE) and the execution time. The third novelty of the work lies in modeling the surface irregularities in the fracture surfaces using Mean and Gaussian curvatures as well as the fuzzy sets. Our fourth contribution lies in generation of multiple starting solution for ICP using concepts from Graph Automorphism and proposition of the hybrid Geometric-ICP algorithm in that connection. Last but not the least is introducing an altogether different two-phase virtual reconstruction scheme. In the first phase, we employed the ICP and DARCES algorithms first individually and then in a cascaded manner. The anatomy of the human mandible clearly exhibits bilateral symmetry. Furthermore, basic biophysical principles indicate that the most stable state for a solid body is the state with minimum energy and this fact should be applicable to the human mandible as well. Since both the ICP and DARCES algorithms are essentially data driven and are purely local in nature, the first phase cannot explicitly guarantee the preservation of either the global shape symmetry or the biomechanical stability of the reconstructed human mandible. The incorporation of anatomical shape knowledge in medical image registration has been discussed in [12], [13]. However, we go one step further in the second phase of our reconstruction paradigm. In the second phase, a composite reconstruction metric is introduced and expressed as a linear combination of three different terms, namely (a) the MSE, (b) a global shape symmetry term and (c) a surface area term (which is shown to be a

measure of biomechanical stability). An angular perturbation scheme is used to optimize the composite reconstruction metric. Thus the second reconstruction phase enables us to explore and address, in an innovative manner, the anatomical shape preservation as well as biophysical stability issues in the reconstruction paradigm (which may not be always possible in the operating room). As shown in this chapter, the second phase of reconstruction integrates computer vision algorithms with ideas from biophysics and mathematics to generate a more accurate reconstruction.

2.4 Image Processing

Figure 2.1: A real patient CT image sequence of a fractured mandible. The images in (a), (b) and (c) are three consecutive slices in the CT sequence.

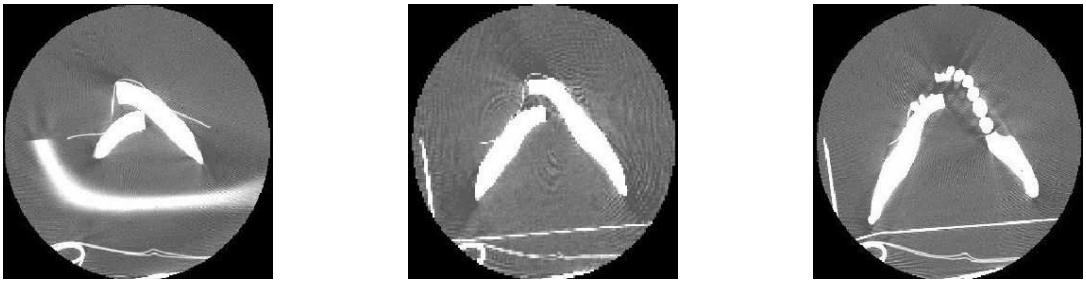

Figure 2.2: A phantom CT image sequence of a fractured mandible. The image in (a) is a slice appearing at the beginning of the sequence, the image in (b) is a slice appearing at the middle of the sequence and the image in (c) is a slice appearing at the end of the sequence. These slices are not consecutive.

The input to the computer vision guided virtual craniofacial reconstruction system is a sequence of 2D grayscale images of a fractured human mandible, generated using CT. Figure (2.1) shows a CT image sequence obtained from a real (human) patient where the images shown in (a), (b) and (c) represent three consecutive CT slices. Figure (2.2) shows three

non-consecutive CT image slices of a phantom mandible where the slice shown in (a) occurs at the beginning of the CT image sequence, the slice shown in (b) occurs in the middle of the CT image sequence and the slice shown in (c) occurs at the end of the CT image sequence. A series of image processing tasks are undertaken before using the surface matching algorithms to register the two fractured bone fragments. The result of the image processing operations on the phantom CT slice in figure (2.2b) is shown in figure (2.4) and on the real (human) patient CT slice in figure (2.1a) is shown in figure (2.3). The software resulting from the implementation of the surface matching algorithms and image processing tasks is currently integrated into a JAVA-based package for computer-assisted reconstructive plastic surgery called *InSilicoSurgeon* (©The University of Georgia Research Foundation Inc., 2004). A brief description of the image processing tasks is as follows:

2.4.1 Thresholding

Two types of thresholding algorithms were used in the present work. For the phantom CT images, the bright components (having higher Hounsfield unit values [16]) represent the fractured mandible (bone) fragments whereas the dark areas (with relatively lower Hounsfield unit values) represent soft tissue. Hence, the threshold value for the binarization of the CT image was not difficult to select and simple thresholding was observed to be sufficient. Based on a priori knowledge, we classify a pixel with grayscale value above a certain threshold value T to belong to the object of interest and represent it using the grayscale value 0 (i.e., color black) as shown in Fig. 3b. Thus, for a grayscale CT image slice $G(i, j)$, we obtain a binary image $B(i, j)$ given by:

$$B(i,j) = \begin{cases} 0 & \text{if } G(i,j) > T \\ 1 & \text{otherwise} \end{cases} \tag{2.1}$$

However, for real (human) patient CT data, the selection of the appropriate threshold is not obvious since the CT images typically contain objects or artifacts of different intensities (varying Hounsfield unit values). For example, a fractured mandibular fragment could contain cavities, dental fillings, crowns and other dental prostheses. In such cases, entropy

based thresholding [17] was found to perform better than simple thresholding. In the case of entropy based thresholding, the threshold value (represented by the variable T in equation (1)) is determined via maximization of the inter-class entropy computed from the grayscale histogram of the CT image. The entropy, in general, is a probabilistic measure of the uncertainty of an event. For an image, the entropy S_c for each graylevel class c (consisting of several graylevel values) can be computed using the grayscale histogram as follows:

$$S_c = \sum_{k \in G_c} p(k) \log_2(p(k)) \tag{2.2}$$

where $p(k)$ is the probability of a pixel having a grayscale value k and G_c is the set of graylevels for class c. In the context of binarization, the graylevel threshold T is chosen such that the total entropy $S = S_1 + S_2$ is maximized.

2.4.2 Connected Component Labeling

Binarization of the CT image by itself cannot distinctly represent the two fracture fragments, as is evident from Figs. 3b and 4b. This is so because one still needs to filter out the undesired artifacts so that only the fractured mandibular fragments are used for the purpose of surface matching. A 2D Connected Component Labeling (CCL) procedure in conjunction with a component area filter was used to remove the undesired artifacts (which are typically small in size). The threshold value for the component area filter was chosen to be 1000 pixels. Connected components with area less than the threshold value were deleted. The result of these operations is illustrated in Figs. 3c and 4c. The image processing tasks described thus far were performed on the individual 2D image slices comprising the CT image stack. The results of the 2D CCL were propagated across the CT image slices, resulting in a 3D CCL algorithm. A 3D component (a fractured jaw bone in this case) was identified by computing the area of overlap of the corresponding 2D components in successive CT image slices.

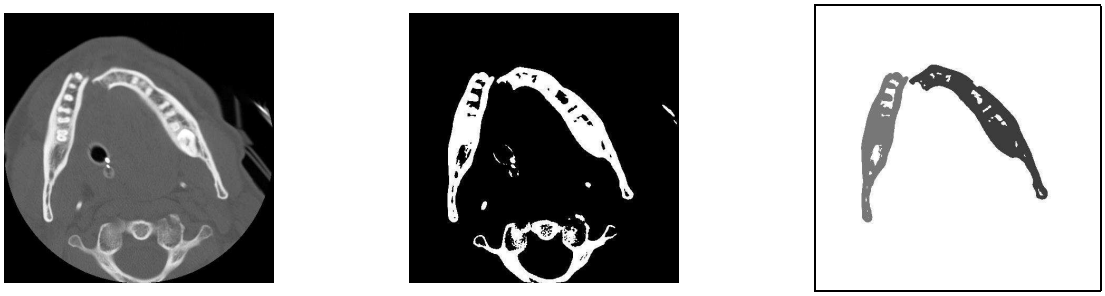

Figure 2.3: (a) A typical 2D CT slice (from a real patient CT sequence). (b) The CT slice after Entropy Thresholding. (c) The CT slice after Connected Component Labeling and Size Filtering. In (c), the two broken mandibular fragments are represented by two different intensity values.

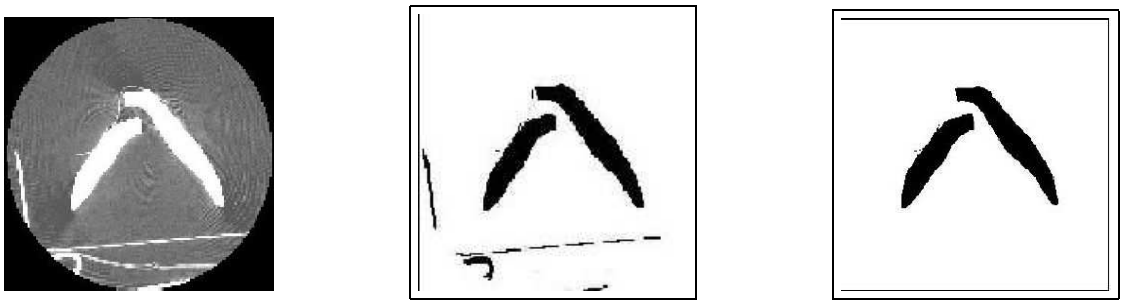

Figure 2.4: (a) A typical 2D CT slice (from a phantom CT sequence). (b) The CT slice after simple thresholding. (c) The CT slice after Connected Component Labeling and Size Filtering. In (b) and (c), the gray scale value 0 (i.e. color black) is used to represent mandible fragments and artifacts.

2.4.3 Contour Data Extraction

After performing the thresholding, CCL and size filtering operations on all the CT image slices, the task of interactive contour detection was performed on the resulting binary image slices. We used two approaches for this purpose. In one approach, the user is required to click on the end points of the fracture contours in each of the binary image slices. The intervening contour points are automatically generated using a contour tracing algorithm. In the other approach, the user can click on potentially interesting points on a contour (typically points of high curvature). In both approaches, the contour points obtained from the individual binary image slices are collated to generate the 3D surface point dataset. A 3D surface point dataset is generated for each fracture surface.

2.5 Surface Matching Using the ICP Algorithm

The task of the ICP algorithm [6] is twofold. The first task is to establish a correspondence between the two surface point sets to be matched. The second task is to compute the 3D transformation that brings the two sets into registration. In the present problem, the cardinalities of the two data sets to be matched are different. We denote the fracture surface (dataset) to be matched as the *sample* fracture surface (dataset) and the fracture surface (dataset) to which the sample fracture (dataset) is to be matched as the *model* fracture surface (dataset).

2.5.1 The Basic ICP Algorithm

The basic ICP algorithm consists of the following steps:

1. The matching points in the model dataset corresponding to points in the sample dataset are determined. This new set of matching points in the model dataset, which represents a subset of the original model dataset, is termed the *closest* set.

2. The 3D rigid body transformation (3D translation and 3D rotation) that brings the two surfaces into registration is computed. The transformation is obtained using the Theory of Quaternions [22].

3. The computed transformation is applied to the original sample dataset and the mean squared error (MSE) between the transformed sample data points and the corresponding closest points is calculated. The MSE (ϵ^2) is given by:

$$\epsilon^2 = (1/n)\sum_{i=1}^{n}((c_i - (Rs_i + T))^2) \tag{2.3}$$

   where R denotes the rotation matrix, T denotes the translation vector, s_i denotes a point of the sample data set, c_i represents the corresponding point in the closest set and n is the total number of sample points.

Steps 1-3 are repeated with an updated sample dataset (generated by applying R and T obtained in the current iteration to the current sample dataset) until the difference in MSE

between two successive iterations drops below a pre-specified threshold (0.01 mm^2 in our case).

2.5.2 Closest Set Computation

Graph theoretic matching has been used extensively in several computer vision problems [21]. In the computation of the closest set, which is the most crucial step in the ICP algorithm, the matching point pairs are determined using the Maximum Cardinality Minimum Weight (MCMW) bipartite graph matching algorithm based on the Hungarian method proposed by Kuhn [23]. We construct a bipartite graph $G(V_1 \cup V_2, E)$ where the 3D sample and model datasets correspond to the two disjoint vertex sets V_1 , and V_2 respectively. The weight w_{ij} of an edge $e_{ij} \in E$ between two vertices v_i and v_j (where $v_i \in V_1$ and $v_j \in V_2$) is given by:

$$w_{ij} = ((x_i - x_j)^2 + (y_i - y_j)^2 + (z_i - z_j)^2))^{1/2} \tag{2.4}$$

Theorem 2.1 *The worst-case time-complexity of the Maximum Cardinality Minimum Weight (MCMW) algorithm for a bipartite graph $G = (V_1 \cup V_2, E)$ with $|V_1| = |V_2| = n$ is $O(n^3)$.*

For the proof of the above theorem see [18], [19].

Claim 2.1 *Given that there is neither a reflection nor a very large (greater than 90^o) rotation (two extremely unlikely cases for a typical craniofacial injury), the Maximum Cardinality Minimum Weight (MCMW) algorithm for a bipartite graph correctly establishes the correspondence between two fracture surfaces at every stage of the Iterative Closest Point (ICP) algorithm in polynomial time.*

Justification: Our justification is based on Theorem 2.1. Each fracture surface, consisting of several 3D data points, is modeled as a vertex set of a weighted bipartite graph $G = (V_1 \cup V_2, E)$. The bipartite graph is complete, i.e., there exists an edge $e_{ij} \in E$ between each vertex pair (v_i, v_j) where $v_i \in V_1$ and $v_j \in V_2$. The weight w_{ij} of edge e_{ij} is chosen to be the Euclidean distance between the corresponding vertices $v_i \in V_1$ and $v_j \in V_2$ where

$i = 1, 2, \ldots n_1;\ n_1 = |V_1|$ and $j = 1, 2, \ldots n_2;\ n_2 = |V_2|$. The vertex set with lower cardinality is denoted as the *sample set* and that with the higher cardinality is denoted as the *model set*. The goal is to compute the *closest set*; i.e., a maximal subset of the model set wherein each point corresponds to a unique point in the sample set such that all points in the sample set are exhausted (principle of maximum cardinality) and simultaneously the sum of the edge weights between all pairs of corresponding points (i.e., $\sum w_{ij}$) is minimized (principle of minimum weight). This procedure is carried out in each iteration of the ICP algorithm. In absence of a reflection or a large (e.g. greater than 90^o) rotation, this graph theoretic optimization procedure, with an objective function as the *sum of the Euclidean distances between all the pairs of matched points*, correctly matches a sample point with a model point without distorting the shape of the fracture surfaces. A greedy approach [24], based on the minimum Euclidean distance between individual pairs of points considered one at a time, on the other hand, would map more than one sample point to a single model point and distort the fracture surface shape. Our problem formulation maps to the following well-known Maximum Cardinality Minimum Weight (MCMW) Bipartite Graph Matching Problem in graph theory, i.e., given a weighted complete bipartite graph $G = (V_1 \cup V_2, E)$ with edge-weights $w_{ij} \geq 0$; determine a pairing of the vertices from two vertex sets V_1 and V_2 such that the vertex set with smaller cardinality is completely exhausted and the total cost of the pairings is minimum. By virtue of its construction the proposed bipartite graph is complete with $E = V_1 \times V_2$ where $|V_1| \leq |V_2|$; such that $\exists$ 1:1 mapping $f : V_1 \rightarrow V_2$. From Theorem 2.1, the MCMW algorithm runs in $O(n^3)$ time for a bipartite graph with two vertex sets of equal cardinality n. In our case, $n = max(n_1, n_2)$. Thus, the proposed solution clearly runs in polynomial time. $\diamond$

2.6 Surface Matching Using the DARCES Algorithm

The DARCES algorithm [9] is widely used for solving 3D registration problems efficiently and reliably, especially in the presence of outliers. The DARCES algorithm requires no local feature detection and no initial transformation estimation for the matching of two 3D data

sets, and thus differs from most feature-based approaches or iterative approaches to the 3D registration problem.

2.6.1 The Basic DARCES Algorithm

The main steps in the DARCES algorithm are as follows:

1. Reference points are selected from the sample data set. Note that the sample data set and the model data set have the same meaning as in the case of the ICP algorithm.

2. From the set of reference points, 3 control points are chosen.

3. Based on certain predefined geometric constraints, the 3 corresponding matching points in the model data set are determined. Note that for the 3 control points, there are many such sets of 3 matching points in the model data set.

4. For each set of 3 pairs of corresponding points (i.e., the 3 control points and one set of 3 matched model points), a 3D rigid body transformation is obtained. Note that 3 pairs of corresponding points are sufficient to determine a 3D rigid body transformation.

5. Each transformation is then applied to all the reference points other than the 3 control points. If the distance between a transformed point and its nearest model point is below a certain threshold, then this reference point is considered to have been successfully aligned to the model surface. Thus the number of successfully aligned sample data points is computed for each transformation.

6. The transformation which has successfully aligned the maximum number of sample data points is deemed to be the solution to the registration problem.

2.7 Surface Matching Using the Hybrid DARCES-ICP Algorithm

Claim 2.2 *The hybrid DARCES-ICP algorithm is expected to yield a lower Mean Squared Error (MSE) compared to that obtained by the DARCES and ICP algorithms in isolation.*

Justification: The DARCES algorithm helps in outlier rejection but the resulting transformation is only approximate. The ICP algorithm, on the other hand, yields a more accurate 3D rigid body transformation but is sensitive to outliers in the input data. Moreover, the pairs of matched points generated by the DARCES algorithm also helps in reducing the cardinalities of the two data sets to be matched (using Bipartite Graph Matching [19]) in the ICP algorithm. Thus the relatively dense bipartite graph used to determine the closest set in the ICP algorithm can be reduced to a relatively sparse bipartite graph with fewer nodes and edges. The subsequent MCMW bipartite graph matching algorithm, (whose run time complexity is determined by the cardinalities of its vertex sets per Theorem 1) has a reduced computational complexity when run on a sparse bipartite graph. Simultaneously, a much lower MSE can be achieved for the matching of the two surfaces, since the DARCES algorithm provides a better starting point to the ICP algorithm by virtue of outlier removal. Thus, the synergistic combination of the DARCES and ICP algorithms, termed as hybrid DARCES-ICP algorithm (where the output of the DARCES algorithm is the input to the ICP algorithm), is expected to yield a higher reconstruction accuracy. $\diamond$ We have exploited the synergism between the DARCES and ICP algorithms in the following three different ways:

1. Using the DARCES transformed sample dataset and the model dataset as the two inputs to the ICP algorithm. Thus, the initial transformation estimate of the ICP algorithm is the one resulting from the DARCES algorithm. This is termed as **Synergism 1**.

2. Using a proper subset of the sample dataset (that has been aligned correctly by the DARCES algorithm) and the model dataset as the two inputs to the ICP algorithm. The initial transformation estimate used by the ICP algorithm is the default estimate, i.e., the initial rotation matrix is the identity matrix and the initial translation vector is the null vector. This is termed as **Synergism 2**.

3. Using the DARCES transformed subset of the sample dataset and the model dataset as the two inputs to the ICP algorithm. Here, the proper subset of the sample dataset

that has been aligned correctly by the DARCES algorithm is used. Also, the initial transformation estimate of the ICP algorithm is the one resulting from the DARCES algorithm. This is tantamount to the combination of **Synergism 1** and **Synergism 2** and is termed as **Synergism 3**.

The composite transformation matrix $\theta_{DARCES-ICP}$ of the hybrid DARCES-ICP algorithm (consisting of a rotation matrix and a translation vector), to be applied to the sample dataset in order to register it with the model dataset is given by:

$$[\theta_{DARCES-ICP}] = [\theta_{DARCES}][\theta_{ICP}] \tag{2.5}$$

where θ_{DARCES} and θ_{ICP} respectively denote the composite transformations obtained from the individual DARCES and ICP algorithms.

2.8 Curvature-based Surface Irregularity Estimation

We have so far treated all the points in a fracture surface equally. Our next goal is to classify and label the individual discrete sampled points on the two fracture surfaces and incorporate that information in our reconstruction paradigm to further improve the reconstruction accuracy. In the present section, we categorize the fracture surface points into various primitive surface categories based on the signs of the local mean (H) and the Gaussian (K) curvatures. Surface labeling of voxels/pixels in volumetric images for feature classification is a well-known technique [25]. The digital surface, within a local window, is approximated by an analytic surface using a least-squares surface fitting technique [26], [27], [28]. Discrete bi-orthogonal Chebyshev polynomials [26], [29] are used as the basis functions in a local $N \times N$ window (where $N = 5$ in our case) around each point to compute the local H and K values. We will follow the notation of [26] for the rest of this section. The elements of $\mathbf{G}$ can be expressed in terms of the estimates of the partial derivatives of the surface as:

$$\begin{aligned} g_{11} &= 1 + f_u^2 \\ g_{22} &= 1 + f_v^2 \\ g_{11} &= g_{22} = f_u f_v \end{aligned} \tag{2.6}$$

Similarly, the elements of **B** can be also expressed in terms of the estimates of the partial derivatives of the surface as:

$$\begin{aligned} b_{11} &= f_{uu}/\sqrt{1+f_u^2+f_v^2} \\ b_{22} &= f_{vv}/\sqrt{1+f_u^2+f_v^2} \\ b_{11} &= b_{22} = f_u f_v/\sqrt{1+f_u^2+f_v^2} \end{aligned} \tag{2.7}$$

The digital surface is approximated by using discrete bi-orthogonal Chebychev polynomials [27]. Discrete bi-orthogonal Chebyshev polynomials are used as basis functions in a local $N \times N$ where (N is odd) window centered about the point of interest. So, each data point in a given $N \times N$ window is associated with a position (u, v) from the set $U \times U$ where N is odd:

$$U = (\frac{-(N-1)}{2}, \cdots, -1, 0, 1, \cdots, \frac{(N-1)}{2}) \tag{2.8}$$

Now, a surface function estimate $\hat{f}$ is obtained of the form:

$$\hat{f}(u,v) = \sum_{i,j=0}^{2} a_{ij}\phi_i(u)\phi_i(v) \tag{2.9}$$

that minimizes the total square error term

$$\varepsilon = \sum_{(u,v)\in U^2} (f(u,v) - \hat{f}(u,v))^2 \tag{2.10}$$

The solution for the unknown coefficients is given by

$$a_{ij} = \sum_{(u,v)\in U^2} f(u,v) b_i(u) b_j(v) \tag{2.11}$$

Here $b_i's$ are the normalized orthogonal Chebyshev polynomials of order i, given by:

$$\begin{aligned} b_0(u) &= \tfrac{1}{N} \\ b_1(u) &= \tfrac{3}{M(M+1)(2M+1)}u \\ b_2(u) &= \tfrac{1}{P(M)}(u^2 - \tfrac{M(M+1)}{3}) \end{aligned} \tag{2.12}$$

where $M = \frac{(N-1)}{2}$ and $P(M)$ is a fifth-order polynomial in M:

$$P(M) = \frac{8}{45}M^5 + \frac{4}{9}M^4 + \frac{2}{9}M^3 - \frac{1}{9}M^2 - \frac{1}{15}M \tag{2.13}$$

The coefficients of functional approximation $a'_{ij}s$ are computed from (2.11 - 2.13). The first order partial derivatives are given in terms of the $a'_{ij}s$ as:

$$\begin{aligned} f_u &= a_{10} \\ f_v &= a_{01} \\ f_{uv} &= a_{11} \\ f_{uu} &= 2a_{20} \\ f_{vv} &= 2a_{02} \end{aligned} \tag{2.14}$$

The elements of $\mathbf{G}$, $\mathbf{B}$ are estimated next using (2.6 and 2.7). The principal curvatures (κ_1, κ_2) are found to be the roots of the following quadratic equation [28]:

$$|\mathbf{G}|\kappa_n^2 - (g_{11}b_{22} + b_{11}g_{22} - 2g_{12}b_{12})\kappa_n + |\mathbf{B}| = 0, \quad n = 1, 2 \tag{2.15}$$

The mean and Gaussian curvatures can be respectively expressed in terms of the principal curvatures (κ_1, κ_2) as:

$$\begin{aligned} H &= (\kappa_1 + \kappa_2)/2 = (g_{11}b_{22} + g_{22}b_{11} - 2g_{12}b_{12})/2(g_{11}g_{22} - g_{12}^2) \\ K &= \kappa_1\kappa_2 = (b_{11}b_{22} - b_{12}^2)/(g_{11}g_{22} - g_{12}^2) \end{aligned} \tag{2.16}$$

The signs of H and K are used to classify the surface point into one of eight qualitative surface types (see table (2.1)). The above procedure is repeated for each point on each of the fracture surfaces for which a valid local window exists.

H, K	$H < 0$	$H = 0$	$H > 0$
$K < 0$	Saddle Ridge	Minimal Surface	Saddle Valley
$K = 0$	Ridge Surface	Flat Surface	Valley Surface
$K > 0$	Peak Surface	None	Pit Surface

Table 2.1: Classification of surface pixels on the basis of signs of H and K

2.9 Fuzzy Set-theoretic Approach to Surface Irregularity Extraction

In this section, we describe an altogether different approach, based on fuzzy sets, to categorize the sampled points on the fracture surfaces. Two fuzzy sets termed as *droop* and *bulge* are

used to classify the fracture contour points [30]. Fuzzy set theory not only permits us to classify a contour point as a droop or bulge, but also enables us to specify the extent of droop or bulge. The average variation of the fracture surface in a direction perpendicular to the plane of fracture is estimated and is denoted by x_{avg}. Note that a fracture surface consists of several fracture contours. For each point on each such contour, the deviation from the average i.e., $(px - x_{avg})$ is determined, where px is the x coordinate of a point p. If $px > x_{avg}$, then the point p belongs to bulge fuzzy set else it belongs to the droop fuzzy set. The goal here is to highlight the surface irregularity and subsequently be able to discriminate between the surface points on the basis of their fuzzy membership values. The fuzzy membership function used for surface labeling is given by:

$$\mu_{droop/bulge} = 1 - \exp(-k|px - x_{avg}|) \tag{2.17}$$

where $\mu_{droop/bulge}$ is the membership value of a point p (with x coordinate value px) in the fuzzy set droop or bulge, as the case may be. The constant k for a particular contour is determined by setting $\mu_{droop/bulge}$ to be very close to 1 (e.g. 0.99) and using the maximum value of $(|x-x_{avg}|)$ for all the points on that contour. This approach for determining the value of k takes into consideration very precisely the local variations of surface coordinate value with respect to the global average of the surface coordinate value over the entire fracture surface. The above fuzzy classification procedure is performed for all points on each of the fracture surfaces.

2.10 Reward/Penalty Schemes

A reward/penalty scheme is introduced to emphasize the effect of the extracted surface irregularities on the process of establishing faithful correspondence. Note that every pair of corresponding points on the opposing fracture surfaces are represented by corresponding elements of the two vertex sets of a bipartite graph. With the reward/penalty scheme, the original edge weights W_{ij} between the two corresponding points i and j are modified by incorporation of a reward-penalty term RP_{ij}. The new edge weights $W_{ij}^{/}$ are given by:

$$W_{ij}^{/} = W_{ij} + \lambda RP_{ij} \tag{2.18}$$

where λ is termed as the reward-penalty coefficient. Two different methods are used to determine the penalty term RP_{ij} in the above equation. This approach is consistent with the two different methods for surface feature extraction. A binary reward/penalty scheme is adopted for the curvature-based surface classification method and a fuzzy reward/penalty scheme is chosen for the fuzzy set-based surface classification method.

2.10.1 Binary Reward/Penalty Approach

The signs of the mean and Gaussian curvatures H and K for a pair of corresponding points from the two opposing fracture surfaces are examined and a reward/penalty value is assigned to the pair of corresponding points based on table (2.2). If there exists no proper local window surrounding a point, then it is not classified into any primitive surface category based on the signs of H and K. Such a point is deemed as unclassified. A pair of points in which at least one of the points is unclassified, is not assigned a reward or penalty value.

Two points i, j	RP_{ij}
Saddle Ridge, Saddle Valley	-1.0
Ridge Surface, Valley Surface	-1.0
Flat Surface, Flat Surface	-1.0
Peak Surface, Pit Surface	-1.0
At least one unclassified point	0.0
All other cases	1.0

Table 2.2: Assignment of reward-penalty value based on the signs of H, K for any two surface points

2.10.2 Fuzzy Reward/Penalty Approach

Two separate fuzzy functions are designed to indicate reward and penalty. If the two points in a pair of corresponding points belong to the same fuzzy set, then they receive a penalty, else they receive a reward. The need for two different functions stems from the fact that the reward is inversely proportional to the membership difference whereas the penalty is directly proportional to the membership difference. The fuzzy reward function μ_R for two points i and j is a function of the individual membership values μ_i and μ_j of these two points in the

fuzzy sets droop and bulge and is given by the following equation:

$$\mu_R(\mu_i, \mu_j) = 2/(1 + \exp(r_c|\mu_i - \mu_j|)) \tag{2.19}$$

where r_c is the reward constant. The value of r_c is chosen such that μ_R is close to 0, when $|\mu_i - \mu_j|$ is maximum (i.e., = 1). We used the following equation to estimate r_c:

$$0.01 = 2/(1 + \exp(r_c)) \tag{2.20}$$

The fuzzy penalty function μ_P for two points i and j is a function of the individual membership values μ_i and μ_j of these two points in the fuzzy sets droop and bulge and is given by the following equation:

$$\mu_P(\mu_i, \mu_j) = (1 - \exp(-p_c|\mu_i - \mu_j|)) \tag{2.21}$$

where p_c is the penalty constant. The value of p_c is chosen such that μ_P is close to 1, when $|\mu_i - \mu_j|$ is maximum (i.e., = 1). We used the following equation to estimate p_c:

$$0.99 = (1 - \exp(-p_c)) \tag{2.22}$$

2.11 Multiple Initial Solutions for the ICP

The main motivation behind the hybrid DARCES-ICP algorithm is to improve the performance of the ICP algorithm. The DARCES algorithm helped in rejection of outliers and gave ICP a better sparse dataset to register. It is also relevant to mention that we have not explored any geometric constraints in the registration process thus far. In the next three sections, our goal is to generate multiple initial solutions based on certain geometric constraints. The subsequent tasks are to filter out the best candidate and propose another hybrid algorithm involving ICP. Besl and McKay [6] suggested multiple initialization as means to attain a global minimum in their version of the ICP algorithm. They suggested comparing shapes' principal moments and sampling the quaternion states based on rotation groups of regular polyhedra to produce multiple initial starting states. We chose to generate multiple solutions, one be eventually used as the starting point for the ICP algorithm, based on the automorphism group of a fracture surface bounding box which is modeled as a cycle graph.

The bounding box for individual fracture surfaces is simply constructed using two pairs of extreme points of a fracture contour that appear in the first and last image slice of the CT image sequence and is modeled as a cycle graph of order 4. The weights assigned to the edges of the cycle graph are the Euclidean distances between the corresponding points. Let us denote the cycle graph of the fracture surface of the fragment frg_1 by B_1 and that of frg_2 by B_2. The main idea is that if the two fracture surfaces should be matched, then their bounding boxes should also match well. We use following interesting concepts from graph isomorphism and graph automorphism in this connection [31]:

Definition 2.1 *Two graphs $G_1 = (V_1, E_1)$ and $G_2 = (V_2, E_2)$ are isomorphic, denoted by $G_1 \cong G_2$, if there exists a bijection $M \subseteq V_1 \times V_2$ such that, for every pair of vertices $v_i, v_j \in V_1$ and $w_i, w_j \in V_2$ with $(v_i, w_i) \in M$ and $(v_j, w_j) \in M, (v_i, v_j) \in E_1$ if and only if $(w_i, w_j) \in E_2$. In such a case M is a graph* **isomorphism** *from G_1 to G_2.*

Definition 2.2 *An* **automorphism** *of a graph G is a graph isomorphism between G and itself.*

The set of all automorphisms of a graph forms a group under the operation of composition. This group is termed the *automorphism group* of the graph.

Lemma 2.1 *The automorphism group of a cycle graph C_n on $n \geq 3$ vertices is a group of order $2n$.*

Proof: A cycle graph with C_n on $n \geq 3$ vertices is left fixed by exactly n rotations as well as exactly n reflections. Thus, the resulting automorphism group has order $2n$.

Thus the automorphism group of, say, B_2 consists of 4 rotation members and 4 reflection members. This means that there can be 8 possible competing orientations of B_2 to match with B_1. We denote the l^{th} automorph of B_2 by $AB_{2,l}$. The nature of the present fracture surface registration problem enables us to employ elegant graph theoretic results to limit the number of candidate solutions for the ICP algorithm.

2.12 Selection Of Bset Possible Candidate Solution

Note that the MCMW bipartite graph matching algorithm essentially establishes the correspondence between the points on the two opposable fracture surfaces. As mentioned above, we employ here additional constraints, specifically geometric constraints and global shape knowledge to improve the results of the surface registration.

2.12.1 Filtering based on Geometric Constraints

Kim and Kak [21] have shown how local geometric constraints can be exploited to improve the correspondence in the context of object recognition. We introduce a dissimilarity function based on two geometric constraints which are invariant to rigid body transformation. In order for B_1 and $AB_{2,l}$ to be well matched:

1. The lengths of corresponding pairs of sides of B_1 and $AB_{2,l}$ should be well matched. Let us denote the lengths of the i^{th} sides of B_1 and $AB_{2,l}$ by d_i^1 and $d_i^{2,l}$ respectively.

2. The angles between the corresponding pairs of sides of B_1 and $AB_{2,l}$ should also be well matched. Let us denote the angle bounded by sides i and j of B_1 and $AB_{2,l}$ by $\theta_{i,j}^1$ and $\theta_{i,j}^{2,l}$ respectively.

The dissimilarity function $\Gamma(B_1, AB_{2,l})$ between B_1 and the l^{th} member of AB_2 can now be defined as a linear combination of the above factors:

$$\Gamma(B_1, AB_{2,l}) = \lambda_1\Gamma_1(B_1, AB_{2,l}) + \lambda_2\Gamma_2(B_1, AB_{2,l}), \text{ where}$$

$$\Gamma_1(B_1, AB_{2,l}) = \textstyle\sum_{i=1}^{4}(|d_i^1 - d_i^{2,l}|), \text{ and} \tag{2.23}$$

$$\Gamma_2(B_1, AB_{2,l}) = \textstyle\sum_{i=1}^{4}(|\theta_{i,((i \bmod 4)+1)}^1 - \theta_{i,((i \bmod 4)+1)}^{2,l}|)$$

The values of λ_1 and λ_2 are determined from the variations of the terms $\Gamma_1(B_1, AB_{2,l})$ and $\Gamma_2(B_1, AB_{2,l})$ for 8 possible values of l and from the normalization $\lambda_1 + \lambda_2 = 1$. The dissimilarity function is computed between B_1 and each of the automorphs of AB_2. The lower the value of the dissimilarity function $\Gamma(B_1, AB_{2,l})$, the better is the match between

B_1 and $AB_{2,l}$. The 8 automorphs are ranked in ascending order of their $\Gamma(B_1, AB_{2,l})$ values and the first 4 automorphs are chosen as the more suitable candidates for being opposable to B_1.

2.12.2 Filtering based on Global Shape Knowledge

After the 4 lower $\Gamma(B_1, AB_{2,l})$ value yielding members of AB_2 are determined, 4 transformations $(\phi_1, \cdots, \phi_4)$ are estimated between B_1 and the eligible automorphs. Each of these four transformations is applied to frg_1 to register it to frg_2. Wang, Peterson and Staib [12] used geodesics and local geometry to improve surface correspondence. In this case, we applied knowledge of the global shape of the human mandible to disambiguate between the 4 reconstructed mandibles by comparing them with an intact reference mandible using a suitable shape similarity measure. The contours $Co_1, \cdots, Co_4$ of each of the reconstructed mandibles and contour Co_{ref} of the intact reference mandible are extracted using simple edge detection. Contour-based shape similarity measures have been well explored in the computer vision literature (e.g., see [32]). We chose Hausdorff distance for the present problem because its relatively fast $O(n^2)$ time complexity and because it avoids the need to establish a prior correspondence between the pixels of the two contours under consideration. The bounding box for each of the five contours is determined. Each contour is scaled to make its bounding box exactly fit into the input image. The Contour Hausdorff Distance (CHD) between two scaled contour data sets Co_i (where $i = 1, \cdots, 4$) and Co_{ref} is given [33] by:

$$H(Co_i, Co_{ref}) = \max(h(Co_i, Co_{ref}), h(Co_{ref}, Co_i)) \tag{2.24}$$

where $h(Co_i, Co_{ref})$ is the directed Hausdorff distance between the two data sets Co_i and Co_{ref} and is defined as:

$$h(Co_i, Co_{ref}) = \max_{a \in Co_i} \min_{b \in Co_{ref}} \|a - b\| \tag{2.25}$$

Here $\|a-b\|$ represents the Euclidean distance between the points a and b. The contour Co^* that yields the minimum value of CHD is deemed to be the best matching contour and the corresponding transformation ϕ^* is treated as the best initial state of the ICP algorithm. We term the above coarse registration approach as the *Geometric* algorithm.

2.13 Hybrid GEOMETRIC-ICP Algorithm

The transformation ϕ^*, the output of the Geometric algorithm is used as the initial transformation for the ICP algorithm. The ICP algorithm initialized with ϕ^*, is denoted as the *Geometric-ICP* algorithm. It is expected that the ICP algorithm, on account of better initialization, should result in lower surface registration error. The transformation ϕ_{GICP} of the Geometric-ICP algorithm can be also interpreted as the following composite transformation:

$$[\phi_{GICP}] = [\phi^*][\phi_{ICP}] \tag{2.26}$$

where ϕ_{ICP} denotes the transformation obtained from the ICP algorithm. We also measure the MSE resulting from the best possible coarse registration transformation ϕ^* computed using the Geometric algorithm. Note that although the Geometric algorithm exploits geometric constraints and knowledge of global shape it uses only 4 pairs of corresponding points and lacks iterative refinement capability. The equation (2.26) is quite similar to equation (2.5) where the input to the ICP algorithm come from the GEOMETRIC algorithm in one case and from the DARCES algorithm in the other.

2.14 Exploration of Bilateral Symmetry

The hybrid DARCES-ICP algorithm produced good surface matching results by yielding a low MSE. But the entire matching process discussed so far, is strictly surface-data driven and hence is local in scope. In order to ensure a more accurate preservation of the global shape of the reconstructed mandible, symmetry issues are considered. There exists extensive research literature [34], [35], [36] in the areas of mathematics, computer vision and image processing, dealing with different types of symmetry such as the reflection symmetry, the rotation symmetry, the skew symmetry *etc.* The anatomical knowledge of the human mandible clearly demonstrates the presence of the bilateral/reflection symmetry. The mathematical notion of reflection symmetry is introduced next following the notations in [37]. Let $\vec{m}$ be a unit vector in $\mathbf{R}^3$, S^2 is the unit sphere of all possible directions in $\mathbf{R}^3$, and $\vec{\Pi}_{\vec{m},n}$ is a plane in $\mathbf{R}^3$ orthogonal to the vector $\vec{m}$ and passing at the distance n from the origin. Let $\vec{g}$ be any

image with its elements denoted as $\vec{g}(x, y, z)$ and $\vec{h} = e_{\vec{m},n}(g)$ be the reflected image with respect to the plane $\vec{\Pi}_{\vec{m},n}$, with elements given by $\vec{h}(x, y, z)$. Then, we can write:

$$e_{\vec{m},n}(\vec{g}(x, y, z)) = \vec{g}(e_{\vec{m},n}(x, y, z))$$

The image $\vec{g}$ is called *reflection symmetrical* if there exists a reflection plane $\vec{\Pi}_{\vec{m},n}$ such that $\vec{h} = \vec{g}$. In such a case, $\vec{\Pi}_{\vec{m},n}$ will be a plane of reflection symmetry for $\vec{g}$. Our goal is to find the plane of maximal bilateral symmetry with respect to some appropriate symmetry measure $\psi(\vec{g}, \vec{h})$. It is well-known that the planes of reflection symmetry of any rigid body pass through its center of mass and are orthogonal to the axes of the ellipsoid of inertia [38]. The moment of inertia matrix M is given by:

$$\begin{pmatrix} \mu_{200} & \mu_{110} & \mu_{101} \\ \mu_{110} & \mu_{020} & \mu_{011} \\ \mu_{101} & \mu_{011} & \mu_{002} \end{pmatrix}$$

The elements of the 3x3 moment of inertia matrix are the second order centralized moments for the rigid body under consideration. So, each matrix element μ_{pqr} can be written as:

$$\mu_{pqr} = \int\int\int (x - x_c)^p \ (y - y_c)^q \ (z - z_c)^r \ dx\, dy\, dz \tag{2.27}$$

In equation(2.27), each of the powers p, q and r can assume any value between 0 and 2 and the centroid of the mandible has the coordinates (x_c, y_c, z_c). For a binary object (a mandible in the present case), we can write $f(x, y, z)$ as:

$$f(x, y, z) = \begin{cases} 1 & \text{if } (x, y, z) \in \textit{mandible} \\ 0 & \text{otherwise} \end{cases} \tag{2.28}$$

The eigenvalues of M can be found as the roots of the secular equation. Since, this secular equation is cubic in nature, which means there are three possible eigenvectors, the number of potential candidates for the plane of reflective symmetry is restricted to just three. This obviates the need of any exhaustive search for determining the plane of symmetry. We rewrite the plane of reflection symmetry $\vec{\Pi}_{\vec{m},n}$ as a general equation of a three-dimensional plane similar to [39],[40]:

$$F(x, y, z) = ax + by + cz - d = 0 \tag{2.29}$$

In equation(2.29), (a, b, c) is a vector describing the plane normal and $d/\sqrt{a^2+b^2+c^2}$ is the perpendicular distance of the plane from the origin. Once the coefficients of the three symmetry planes are determined, the entire mandible is reflected about each of the three planes. We look forward to compute:

$$\max(\psi(\vec{g}, \vec{h_1}), \psi(\vec{g}, \vec{h_2}), \psi(\vec{g}, \vec{h_3}))$$

where $\vec{h_1}, \vec{h_2}, \vec{h_3}$ represent the three reflected mandibles. For each voxel $\vec{g}(x, y, z)$ in the reconstructed mandible $\vec{g}$, there exists a corresponding $\vec{h}(x, y, z)$ in any of the reflected mandibles $\vec{h}$ (where $\vec{h} \in (\vec{h_1}, \vec{h_2}, \vec{h_3})$), which can be estimated from the following equation [40]:

$$\vec{h}(x, y, z) = \begin{cases} \vec{g}(x, y, z) - \frac{F(\vec{g})}{\|\nabla F\|}\frac{\nabla F}{\|\nabla F\|} & \text{if } F(f) > 0 \\ \vec{g}(x, y, z) + \frac{F(\vec{g})}{\|\nabla F\|}\frac{\nabla F}{\|\nabla F\|} & \text{otherwise} \end{cases} \tag{2.30}$$

where F is computed from the equation (2.29). There are various measures of symmetry available in the literature [37], [41], [42] such as sum of absolute distance, sum of squared distance, normalized cross- correlation *etc.* Out of the various measures, we chose the normalized cross-correlation to quantify the extent of symmetry $\psi(\vec{g}.\vec{h})$. The normalized cross-correlation between the reconstructed mandible $\vec{g}$ and the reflected mandible $\vec{h}$ is given by [40]:

$$\psi(\vec{g}, \vec{h}) = \frac{(\vec{g} - \overline{g}\vec{u})(\vec{h} - \overline{h}\vec{u})}{\|(\vec{g} - \overline{g}\vec{u})\|\|\vec{h} - \overline{h}\vec{u})\|} \tag{2.31}$$

where $\overline{g}$ and $\overline{h}$ are the means of the elements of $\vec{g}$ and $\vec{h}$ respectively and $\vec{u}$ is a $N - dim.$ unit vector. One of the three candidate planes, about which the corresponding reflected mandible yields the maximum value of the symmetry measure, will be deemed as the plane of bilateral/reflection symmetry. The corresponding symmetry measure will be deemed as the coefficient of symmetry. It may be noted that our principal aim was to compute the coefficient of symmetry rather than very accurate determination of the plane of symmetry. Thus, we did not employ any sophisticated techniques like the Downhill Simplex method [43] for further refining the plane of symmetry.

2.15 Estimation of Biomechanical Stability

Since human mandible is a solid body with biomechanical properties, we estimated the biomechanical stability of the reconstructed mandible. In the first subsection 2.15.1, we argumentatively validate our claim that a measure of stability for an object under certain conditions is provided by its minimum surface area. In the following subsection 2.15.2, we use techniques from differential geometry to compute the surface area.

2.15.1 Biomechanical Stability in terms of Surface Area

Claim 2.3 *Maximum biomechanical stability of a rigid linear body under conditions of near zero volumetric response and constant surface force is ensured by a state with minimum surface area.*

Justification: A biomechanical stability for a rigid linear body can be conceived as a state with minimum potential energy U. The general form of U is given by [44]:

$$U = \int\int\int f(\varphi, \chi, Y, \sigma)\ dv$$

where φ, χ, Y and σ denotes the normal strain, shear strain, Young's Modulus and Poisson ratio respectively. Let us consider a deformed body with volume V and surface area S and a volume load (basically body force) B and surface load (basically shear force) T. Then U can be mathematically expressed in a way similar to that in [45]:

$$U = \int\int\int L_b(u)\ dv + \int\int L_s(u)\ ds \tag{2.32}$$

where $L_b(u)$ and $L_s(u)$ respectively denote the volume load potential and surface load potential and u the displacement field. The potentials are given by:

$$\begin{aligned} B &= -\tfrac{\delta L_b}{\delta u} \\ T &= -\tfrac{\delta L_s}{\delta u} \end{aligned} \tag{2.33}$$

Applying calculus of variations to (2.32) and (2.33), we can write:

$$\delta U = \int\int\int [-B \cdot \delta u] dV + \int\int\ [-T \cdot \delta u] dS \tag{2.34}$$

The normal and shear strains occurring in response to a force field are represented by the displacement field u and resisted by forces arising from the Young's and shear moduli. The body force B and the surface shear forces T will result in a deformation pattern that minimizes U. From (2.34), we can state that the following criterion must be satisfied under equilibrium conditions:

$$\int\int [-T \cdot \delta u] dS + \int\int\int [-B \cdot \delta u] dV - \delta U = 0 \tag{2.35}$$

For the purpose of this discussion, we may assume near zero resistance to movement resulting from a force of unity, thus the energy related to volumetric response i.e. the second term in (2.35) is near zero. Hence it can be concluded that a minimum potential energy state results in minimum surface energy. Further, minimum surface energy in the context of moving fragments with constant surface force T (which makes the quantity within the square bracket in the first term in (2.35) a constant) is consistent with minimum surface area (leaving $\|\delta U\| \propto \int\int \ dS$). So, a biomechanically stable state (i.e. a state with minimum potential energy) is guaranteed by a state with minimum surface area.

2.15.2 Computation of Surface Area

Since, the human mandible possesses curved surfaces, we used techniques from differential geometry to calculate the area. A digital surface S can be parameterized as $\vec{S}(u, v) = [u \ v \ f(u, v)]$. The area A for such a surface can be written as [26]:

$$A = \int\int \ \sqrt{g} \ dudv \tag{2.36}$$

where g is called the *metric determinant* (defined as the determinant of the *First fundamental form* $\mathbf{G}$) of the surface [28]. So, we divide the surface S into appropriate number (say n) of disjoint surface patches (where SP_i denotes the i^{th} surface patch). Thus, we can write:

$$\begin{aligned} &S = \cup_{i=1}^{n} SP_i \\ &SP_i \cap SP_j = \xi \qquad if(i \neq j) \end{aligned} \tag{2.37}$$

where ξ is a null set. With this idea, we can modify equation (2.36) as:

$$\begin{aligned} &A_i = \int\int \ \sqrt{g_i} \ dudv \\ &A = \textstyle\sum_{i=1}^{n} A_i \end{aligned} \tag{2.38}$$

2.16 Reconstruction Phase-II

The phase-I of this two-phase mandibular reconstruction scheme exclusively deals with the accuracy of registration of the two fracture surfaces. Thus the symmetry and the biomechanical stability constraints cannot be explicitly enforced in the first phase of the reconstruction. The principal rationale behind the second phase, which consists of an angular perturbation scheme, is to arrive at a configuration that not only minimizes the MSE between the matched fracture surfaces but also yields the best possible shape symmetry as well as biomechanical stability of the reconstructed mandible. A composite reconstruction metric *(CRM)*, expressed as a linear combination of three terms involving MSE, global shape symmetry and biomechanical stability is proposed as the overall performance measure of the two-phase virtual reconstruction paradigm. This *CRM* is treated as the objective function of a convex optimization problem. The inverse of the symmetry measure $\psi(\vec{g}, \vec{h})$, mentioned in equation (2.31), is used in *(CRM)* as the present optimization problem is casted as a minimization problem. So, the goal is to attain a reconstructed state which generates minimum MSE, minimum value of the inverse of the symmetry measure and minimum surface area (shown to be a measure of biomechanical stability, see claim 2.3). Mathematically, *CRM* is given by:

$$\Omega = \lambda_1 \epsilon^2 + \lambda_2 \psi^{-1} + \lambda_3 \bar{A} \tag{2.39}$$

where the MSE (ϵ^2) is computed using equation (2.3), inverse of the shape symmetry ψ^{-1} is estimated from equation (2.31) and the average surface area $\bar{A}$ is determined from equation (2.38). There exists several standard techniques for convex optimization problems [43]. However, we used a small-scale angular perturbation scheme to optimize the proposed performance measure. Our strategy is to recompute each of the three terms in equation (2.39) over every perturbed state for a range of angular perturbation with a specific quantization about all the three (x, y, z) axes. A somewhat similar strategy can be found in [46]. We basically need to find a finer transformation (ϕ_{AP}) following the transformation (($\phi_{DARCES-ICP}$)) obtained from the hybrid DARCES-ICP algorithm. It is assumed that ϕ_{AP} contains only some small rotation and no translation. The composite transformation (ϕ_{Comp}) of the two-

phase reconstruction is given by:

$$[\phi_{Comp}] = [\phi_{AP}][\phi_{DARCES-ICP}] \tag{2.40}$$

Typically, ϕ_{AP} is a clockwise/counter-clockwise rotation about one of the x, y, z axes. The range and quantization of angular perturbation are based on some arguments as well as some trade-offs. Since we have already achieved a reasonably good (minimum MSE yielding) local state in the first phase of the reconstruction, we can expect that this locally good solution is not very far off from the best overall solution (resulting in the minimum Ω value). This explains why we don't need any sophisticated optimization technique and subsequently allows us to keep the range of the angular perturbation small. The choice of the angular quantization is a judicious trade-off between the execution time and the accuracy. The smaller the angular quantization, the higher is the execution time of the algorithm. On the contrary, making the angular quantization too large may prevent the algorithm from arriving at the best possible solution. As an integral part of this approach, we were also keen to find out whether MSE by itself could be reduced any further. Besl and McKay [6] proposed multiple initialization as means to attain a global minimum in their version of the ICP algorithm. They suggested comparing shapes' principal moments and sampling the quaternion states [22] based on rotation groups of regular polyhedra to produce multiple initial starting states. We used transformation obtained from the DARCES as a good starting state for the ICP algorithm on the grounds of outlier rejection. The angular perturbation approach, by its exploration of the reconstruction states which are rotationally close to the one obtained from the hybrid DARCES-ICP algorithm, could potentially lead to a lower MSE (compared to that of the hybrid DARCES-ICP algorithm) in its search for the lowest *CRM*. The coefficients of the functional approximation $(\lambda_1, \lambda_2, \lambda_3)$ are computed from:

$$\begin{aligned} &\tfrac{\lambda_1}{|\Delta(\epsilon^2)|} = \tfrac{\lambda_2}{|\Delta(\psi^{-1})|} = \tfrac{\lambda_3}{|\Delta(A)|} \quad \text{and} \\ &\textstyle\sum_{i=1}^{3}(\lambda_i) = 1. \end{aligned} \tag{2.41}$$

where $\Delta(t)$ denotes the normalized absolute difference (i.e. difference of the maximum and minimum values, divided by the maximum value) of the term t over the range of perturbation.

2.17 Experimental Results

In this section, we will first discuss the experimental results of various surface matching algorithms on both phantom as well as real patient CT data. Next, we will demonstrate the effectiveness of composite reconstruction scheme by showing results on shape symmetry, biomechanical stability and angular perturbation.

Datasets	MSE-DAR. (mm^2)	MSE-ICP (mm^2)	MSE-Hyb. DAR.-ICP (mm^2)
$Phantom-1$	0.33	0.91	0.25
$Real-1$	4.62	2.07	1.24

Table 2.3: MSE Values for Different Datasets using the DARCES, ICP and Hybrid DARCES-ICP Algorithms

Table (2.3) compares the reconstruction accuracy of the ICP, the DARCES and the Hybrid DARCES-ICP algorithms for a typical phantom and a typical real (human) patient dataset. In both the cases, the hybrid DARCES-ICP algorithm outperforms the individual ICP and DARCES algorithms. The convergence in the case of the hybrid DARCES-ICP algorithm is achieved within 3-4 iterations as compared to 6-8 iterations for the original ICP algorithm. However, in the case where each fracture surface dataset consists of only the interest points (essentially points of high curvature), both the DARCES and the ICP algorithms take only a few seconds more than the hybrid DARCES-ICP algorithm for completion. For example, in the case of real (human) patient CT data, all the three algorithms finished their execution within well less than a minute on a 1.73 GHz $Intel^{©}$ $Pentium^{©}M$ Processor. Although the hybrid DARCES-ICP algorithm is observed to result in lower surface matching error, its computational benefit (in terms of execution time) compared to that of the ICP algorithm used in isolation is perceivable only in cases where the input datasets to the ICP algorithm are very dense. In such cases, the DARCES component of the hybrid DARCES-ICP algorithm can be used to greatly prune the sample dataset by virtue of outlier removal. Subsequently, the ICP component of the hybrid DARCES-ICP algorithm would run with a considerably sparse sample dataset, resulting in a perceivably lower computation time.

Type of Synergism	MSE for Hybrid DARCES-ICP (mm^2)
$Synergism-1$	2.07
$Synergism-2$	1.65
$Synergism-3$	1.24

Table 2.4: MSE Values for the Hybrid DARCES-ICP algorithm using three Different Synergism Strategies

Table (2.4) shows the impact of the various levels of synergism between the ICP and DARCES algorithms (discussed in Section 2.7) on the MSE. It is interesting to note that not all the ways of exploiting synergism between the DARCES and ICP algorithms are equally effective. The subset of the sample dataset that is properly aligned by the DARCES algorithm consists of the original sample dataset with possible outliers removed. When the ICP algorithm is run on this filtered dataset, with the initial transformation estimate as the output of the DARCES algorithm (i.e., **Synergism 3**), the lowest MSE is achieved.

Scheme	Penalty Coeff.	MSE (mm^2)
$Hybrid\ \ DARCES-ICP$	–	0.251
$Hybrid\ \ DARCES-ICP+FuzzySetbased$	1.0	0.254
$Hybrid\ \ DARCES-ICP+FuzzySetbased$	0.5	0.235
$Hybrid\ \ DARCES-ICP+FuzzySetbased$	0.1	0.248
$Hybrid\ \ DARCES-ICP+Curvaturebased$	1.0	0.252
$Hybrid\ \ DARCES-ICP+Curvaturebased$	0.5	0.247
$Hybrid\ \ DARCES-ICP+Curvaturebased$	0.1	0.234

Table 2.5: MSE Values for a Phantom Dataset using Hybrid DARCES-ICP algorithm with various reward-penalty schemes

Table (2.5) demonstrates the impact of modeling the irregularities present in the pixels of a typical fracture surface. Note that the modeling of these irregularities is necessary but not sufficient to guarantee a better rconstruction. The tuning of the penalty coefficient plays an important role for that purpose. This fact is evident from table (2.5) where only certain values of the penalty coefficient yield a lower MSE compared to that from the hybrid DARCES-ICP

algorithm. Since the hybrid DARCES-ICP algorithm generates a MSE which is very close to the minimum possible value (for a given pair of fracture surfaces), a correct choice of the penalty coefficient would help attain the global minimum (causing further decrease of MSE) whereas a wrong choice would take the solution away from the global minimum (leading to an increase in MSE).

Rank of the Automorph	Dissimilarity Function Value
1	52.20
2	57.30
3	61.37
4	66.51

Table 2.6: Dissimilarity Function Values for Competing Automorphs

Next, we show some results on the improvement of the registration error from the ICP algorithm using hybrid Geometric-ICP algorithm. As mentioned earlier, the fracture surface bounding box is modeled as a cycle graph of order 4. Thus, there are a total of 8 possible automorphs. The best 4 out of these 8 competing automorphs from AB_2 are selected based on the dissimilarity function value (see table (2.6)) using equation (2.23). The best 4 candidate transformations $\phi_1, \cdots, \phi_4$ are then estimated from B_1 and the best four automorphs and applied to frg_1 resulting in the 4 reconstructed mandibles $M_1, \cdots, M_4$.

Contour from Figure (2.5)	Rank	CHD Value
Co_1	1	111.22
Co_2	2	2.24
Co_3	3	52.43
Co_4	4	149.97

Table 2.7: CHD Values for Competing Contours

Figure (2.5) shows the reference contour Co_{ref} in the first row and the contours of the four registered mandibles $Co_1, \cdots, Co_4$ in the second and third rows. Table (2.7) shows the CHD values obtained using equation (2.24), from which Co^* (equal to Co_2 in the present case) and ϕ^* (equal to ϕ_2) are estimated. Figure (2.5) clearly demonstrate how multiple competing fracture surfaces and hence multiple candidate solutions are generated and the

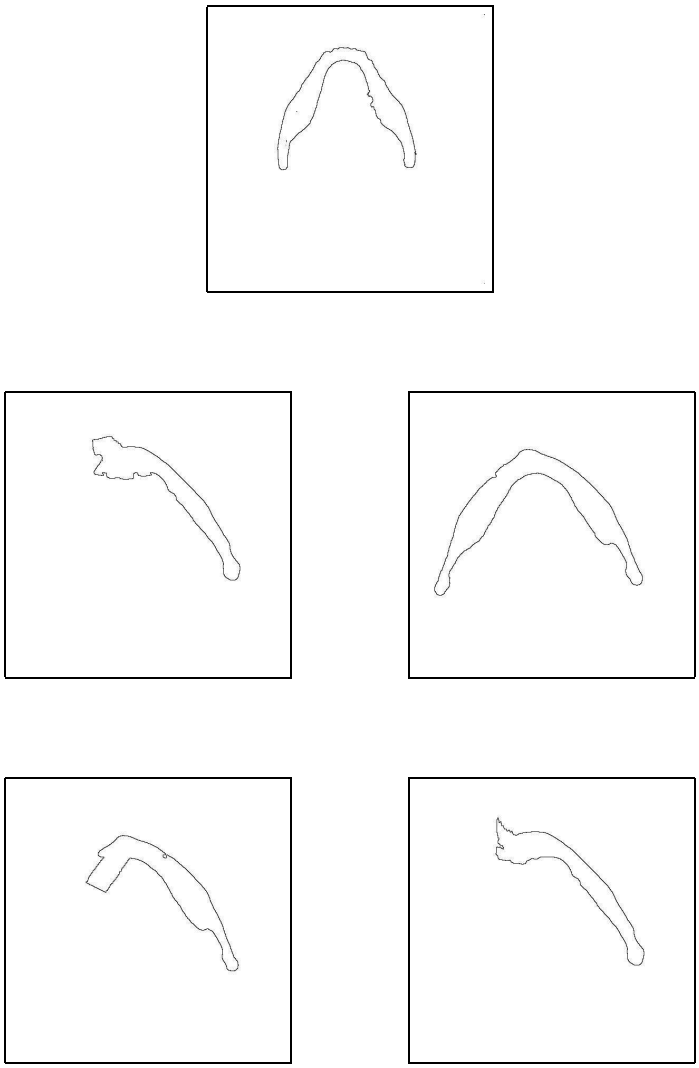

Figure 2.5: Reference and Candidate Contours

best (coarse) solution (denoted as ϕ^*)is obtained. The algorithm leading to the coarse solution is termed as the Geometric algorithm as the solution is based on fulfillment of certain geometric constraints.

Table (2.8) and figure (2.6) quantitatively and qualitatively describes the performance of various reconstruction algorithms for a real fracture. It is an interesting observation that accuracy of DARCES and Geometric algorithms are similar. The ICP algorithm, by itself, performed better than both DARCES and Geometric algorithms. The synergism between

Reconstruction Algorithm	MSE (mm^2)
$DARCES$	4.62
ICP	2.07
$Hybrid\ DARCES - ICP$	1.24
$Geometric$	4.57
$Hybrid\ Geometric - ICP$	1.96

Table 2.8: MSE values for 5 different reconstruction algorithms for a real fracture

DARCES and ICP algorithms as well as between Geometric and ICP algorithms further improve the reconstruction accuracy. Since the best reconstruction accuracy is obtained from the hybrid DARCES-ICP algorithm, rendred volumes of a broken mandible (of a real patient) and its reconstructed version using the hybrid DARCES-ICP algorithm is illustrated next in figure (2.7). In figure (2.8), the slice-wise reconstruction of a phantom mandible using DARCES, ICP and hybrid DARCES-ICP algorithm is presented. A visual comparison of the projections of a 3D intact phantom mandible and a 3D reconstructed phantom mandible along x, y, z axes is shown in figure (2.9).

Coeff. of Sym.	Eqn. of the Candidate Planes for Sym.	Comments
0.79	$0.98x - 0.16y + 0.12z = 65.42$	Plane of Bilateral Sym.
0.27	$-0.20x + 0.87y - 0.45z = 58.78$	-
0.35	$-0.03x + 0.47y + 0.88z = 50.95$	-

Table 2.9: Plane of Symmetry and Coefficient of Symmetry for a phantom dataset in unperturbed states

λ_1 (Coeff. of ϵ^2)	λ_2 (Coeff. of ψ^{-1})	λ_3 (Coeff. of A)
0.82	0.06	0.11

Table 2.10: Coefficiets of the CRM for a phantom dataset

Table (2.9) shows typical values for the coefficient of symmetry for the three different candidate planes in the unperturbed state. The variations of the (a) mean squared error,

State	ϵ^2	ψ^{-1}	A	Ω
$Optimal(x, -0.4^0)$	0.138	0.952	0.892	0.275
$Unperturbed(-, -)$	0.148	0.964	0.982	0.293

Table 2.11: Comparison of performance measures for a phantom dataset in the optimal and unperturbed states

(b) inverse coeffciient of symmetry for the plane of the bilateral symmetry, (c) average surface area and (d) normalized composite reconstruction metric as a function of angular perturbations along all the three major axes are graphically portrayed in figure (2.10). The values for coefficients of (a), (b) and (c) are shown in table (2.10). With the incorporation of very small angular perturbations, it is possible to attain a reconstruction state, which not only yields better results in terms of the average surface area and shape symmetry, but also reduces the local MSE. This is clearly revealed in table (2.11), where the first and the second row respectively show the values of MSE, inverse shape symmetry and average surface area (see equation (2.41)) for the unperturbed configuration (i.e. the reconstruction generated by the hybrid DARCES-ICP algorithm) and the optimal configuration (for a perturbation of-0.40^o about the x-axis, yielding the minimum normalized CRM value). These results show the effectiveness of the second phase of the proposed virtual reconstruction.

2.18 Conclusion and Future Work

The chapter addressed various interesting aspects of 3D virtual craniofacial reconstruction from single fractures. A single 3D image stack is treated as a sequence of 2D images at the time of extracting the data and displaying the registered images. We tackled the problem as a single 3D registration for an image stack instead of slicewise 2D registration. Two different classes of algorithms namely the ICP and the DARCES were first applied individually and then in a cascaded manner for accurate surface matching. The combination of these two algorithms, described as the hybrid DARCES-ICP algorithm, resulted in an improved MSE

and a considerable reduction in the execution time compared to the ICP algorithm used in isolation. The irregularities present in the fracture surfaces are modeled using Mean and Gaussian curvatures as well as fuzzy sets. The MSE from the DARCES-ICP algorithm is further reduced by incorporating the fracture surface information into the reconstruction paradigm by means of two reward-penalty schemes. Note that all these algorithms exploited the point set representation of the fracture surfaces. However, a fracture surface can be also described as a solid object with a well-defined bounding box. This very fact motivated us to design Geometric and hybrid Geometric-ICP algorithms. The hybrid DARCES-ICP algorithm mainly benefits from outlier rejection in the fracture surface datasets. The hybrid Geometric-ICP on the contrary takes advantage of fulfillment of certain geometric constraints. Our next focus was preservation of global shape and biomechanical stability of the reconstructed human mandible in addition to accurate local surface matching. Human mandible is found to exhibit bilateral symmetry. The plane of bilateral symmetry was computed using the normalized cross-correlation. Minimization of surface area was shown to be mathematically equivalent to minimization of surface energy and was used as a measure of biomechanical stability. The plane of bilateral symmetry and average surface area were estimated for the reconstructed mandible based on the hybrid DARCES-ICP algorithm. A composite reconstruction metric, expressed as a linear combination of the mean squared error, global shape symmetry and surface area, was subsequently introduced as the performance measure of the reconstruction process. A local search in this phase, based on an angular perturbation scheme, was shown to result in a solution that minimizes the composite reconstruction metric instead of just the MSE alone.

As a part of the future research, we plan to build the anatomical models of the reconstructed mandible. This model can be used to generate useful feedback on the virtual reconstruction process. For an example, we can fine tune the coefficients of the three different factors in the composite reconstruction metric to ensure a more anatomically meaningful reconstruction. We also look forward to possible use of a robot arm to peform the surgery in presence of an experienced surgeon. Thus, the robot can apply the transformation, as predicted from the various reconstruction algorithms, to put the fractured fragments into

registration. Another direction for the future work would be to replace the bounding box of a fracture surface by its convex hull in the Geometric and Geometric-ICP algorithms. It will be also interesting to try some more combinations of the surface matching algorithms e.g. incorporating the fracture surface irregularity information in the hybrid Geometric-ICP algorithm, exploration of a hybrid DARCES-Geometric-ICP algorithm *etc.*

2.19 References

[1] W. Mollemans, F. Schutyser, N. Nadjmi and P. Suetens, "Very fast soft tissue predictions with mass tensor model for maxillofacial surgery planning systems", in *Proc. of* 9^{th} *Annual Conf. of the Int. Soc. for Computer Aided Surgery*, 2005, pp. 491-496.

[2] E. Keeve, S. Girod and B. Girod, "Craniofacial Surgery Simulation", *Proc. of* 4^{th} *Int. Conf. on Visualization in Biomedical Computing*, Hamburg, Germany, 1996, pp. 541-546.

[3] R. Enciso, A. Memon, D. A. Fidaleo, U. Neumann, and J. Mah, "The Virtual Cranio-Facial Patient Project: 3D Jaw Modeling and Animation", presented at 11^{th} Annual Medicine Meets Virtual Reality Conference, Newport Beach, California, January 22-25, 2003.

[4] A. Sarti, R. Gori, C. Marchetti, A. Bianchi and C. Lamberti, "Maxillofacial Virtual Surgery from 3D CT Images", in *VR in medicine*, M. Akay and A. Marsh Ed., Springer, 2000.

[5] S. Zachow, H.C. Hedge and P. Deuflhard, "Computer assisted planning in cranio-maxillofacial surgery", in *Journal of Computing and Information Technology - Special Issue on Computer-Based Craniofacial Modeling and Reconstruction*, 14(1), pp. 53-64, 2006.

[6] P.J. Besl and N.D. McKay, "A Method for Registration of 3-D Shapes", *IEEE Trans. Pattern Anal. Mach. Intell.*, 14(2), pp. 239-256, 1992.

[7] J.B.A. Maintz and M.A. Viergever, " A survey of medical image registration", *Med. Image Anal.*, 2(1), pp. 1-36, 1998.

[8] S. Granger, X. Pennec, and A. Roche, "Rigid Point-Surface Registration Using an EM variant of ICP for Computer Guided Oral Implantology", in *Proc. of the Int. Conf. on Medical Image Computing and Computer Assisted Intervention*, Utrecht, The Netherlands, 2001, pp. 752-761.

[9] C.S. Chen, RANSAC-Based DARCES, "A New Approach to Fast Automatic Registration of Partially Overlapping Range Images", *IEEE Trans. Pattern Anal. Mach. Intell.*, 21(11), pp. 1229-1234, 1999.

[10] M. Rogers and J. Graham, "Robust Active Shape Model Search for Medical Image Analysis", in *Proc. of Int. Conf. on Medical Image Understanding and Analysis*, Portsmouth, UK, 2002, pp. 1-4.

[11] S. Ourselin, A. Roche, S. Prima, and N. Ayache, "Block Matching: A General Framework to Improve Robustness of Rigid Registration of Medical Images", in *Proc. of the* 3^{rd} *Int. Conf. on Medical Robotics, Imaging And Computer Assisted Surgery, A.M. DiGioia and S. Delp Ed.)*, LNCS 1935, Pittsburgh, PA, 2000, pp. 557-566.

[12] Y. Wang, B. Peterson and L. Staib, "Shape-based 3D Surface Correspondence Using Geodesics and Local Geometry", in *Proc. of the* 1^{st} *IEEE Int. Conf. on Computer Vision and Pattern Recognition*, Hilton Head Island, USA, 2000, pp. 644- 651.

[13] K.M. Pohl, S.K. Warfield, R. Kikinis, W.E.L. Grimson and W.M. Wells, "Coupling Statistical Segmentation and PCA Shape Modeling", in *Proc. of the* 7^{th} *Int. Conf. on Medical Image Computing and Computer Assisted Intervention*, Saint-Marlo, France, 2004, pp. 151- 159.

[14] A.S. Chowdhury, S.M. Bhandarkar, E.W. Tollner, G. Zhang, J.C. Yu and E. Ritter, "A Novel Multifaceted Virtual Craniofacial Surgery Scheme using Computer Vision", in *Proc. of Computer Vision for Biomedical Image Applications: Current Techniques and*

Future Trends, an ICCV Workshop, Y Liu, T. Jiang and C. Zhang (Eds.), LNCS 3765, Beijing, China, 2005, pp. 146 - 159.

[15] W.S. Rasband, "ImageJ", *U. S. National Institutes of Health*, Bethesda, Maryland, USA, http://rsb.info.nih.gov/ij/, 1997-2006.

[16] Hounsfield G.N., Nobel Award Address, Computed Medical Imaging. Med. Phys., 7(4), pp. 283-290, 1980.

[17] P.K. Sahoo, S. Soltani, K.C. Wong and Y.C. Chen, "A Survey of Thresholding Techniques", *Computer Vision, Graphics, and Image Processing*, 41, pp. 233-260, 1988.

[18] C.H. Papadimitriou and K. Steiglitz, *Combinatorial Optimization: Algorithms and Complexity*, Prentice Hall of India; 1982.

[19] Christofides N., Graph Theory An Algorithmic Approach: Academic Press; 1975.

[20] A. Rangarajan, H. Chui, E. Mjolsness, S. Pappu, L. Davachi, P.S. Goldman-Rakic and J. S. Duncan, "A Robust Point Matching Algorithm for Autoradiograph Alignment", *Med. Image Anal.*, 1(4), pp. 379-398, 1997.

[21] W. Kim and A.C. Kak, "3-D Object Recognition Using Bipartite Matching Embedded in Discrete Relaxation", *IEEE Trans. Pattern Anal. Mach. Intell.*, 13(3), pp. 224-251, March 1991.

[22] W.R. Hamilton, On Quaternions, in *Proc. of the Royal Irish Academy*, 3, pp. 1-16, 1847.

[23] H.W. Kuhn, The Hungarian method for the assignment problem, *Nav. Res. Log. Quart.*, 2, 1955.

[24] T.H. Cormen, C.E. Leiserson, R.L. Rivest and C. Stein, *Introduction to Algorithms*, MIT Press, 2001.

[25] R. Yarger and F. Quek, Surface Parameterization in Volumetric Images for Feature Classification, *Proc. First IEEE Intl. Symp. Bioinformatics and Biomed. Engr.*, Arlington, VA, 2000, pp. 297-304.

[26] P.J. Besl, Surfaces In Early Range Image Understanding, Ph.D. dissertation, Dept. of Computer Science, Michigan Univ., Ann Arbor, MI, 1986.

[27] R.M. Haralick, "Digital step edges from zero crossing of second directional derivatives", *IEEE Trans. Pattern Anal. Mach. Intell.*, 6(1), pp. 58 - 68, 1984.

[28] I.D. Faux and M.J. Pratt, *Computational geometry for design and manufacture*, John Wiley & Sons, 1979.

[29] M. Suk and S.M. Bhandarkar, *Three-Dimensional Object Recognition from Range Images*, Springer-Verlag, 1992.

[30] K. Miyajima and A. Ralescu, Spatial organization in 2D segmented images: Representation and recognition of primitive spatial relations, *Fuzzy Sets and Systems*, 65, pp. 225 - 236, 1994.

[31] Valiente G., *Algorithms on Trees and Graphs*, Springer-Verlag, Berlin-Heidelberg, 2002.

[32] R. C. Veltkamp and L. J. Latecki, "Properties and Performance of Shape Similarity Measures", *Proc. of the Tenth IFCS Int. Conf. on Data Science and Classification*, pp. 1-9, Ljubljana, Slovenia. 2006.

[33] D.P. Huttenlocher, G.A. Klanderman and W.J. Rucklidge, "Comparing Images Using the Hausdorff Distance", *IEEE Trans. Pattern Anal. Mach. Intell.*, 15(9), pp. 850-863, 1993.

[34] H. Zabrodsky, S. Peleg and D. Avnir, "Symmetry as a Continuous Feature", *IEEE Trans. Pattern Anal. Mach. Intell.*, 17(12), pp. 1154 - 1166, 1995.

[35] C. Sun and J. Sherrah, "3D Symmetry Detection Using The Extended Gaussian Image", *IEEE Trans. Pattern Anal. Mach. Intell.*, 19(2), pp. 164 - 169, 1997.

[36] A.V. Tuzikov and S.A. Sheynin, "Symmetry Measure Computation for Convex Polyhedra", *J. Math. Imag. Vis.*, 16, pp. 41 - 56, 2002.

[37] A. Tuzikov, O. Colliot and I. Bloch, "Brain Symmetry plane computation in MR images using inertia axes and optimization", in *Proc.* 16^{th} *Int. Conf. on Pattern Recognition*, Quebec, Canada, 2002, pp. 10516-10519.

[38] H. Goldstein, *Classical Mechanics*, Addison-Wesley, 1982, ch. 5.

[39] S. Prima, S. Ourselin, and N. Ayache. "Computation of the Mid-Sagittal Plane in 3D Brain Images". *IEEE Trans. Med. Imag.*, 21(2), pp. 122-138, 2002.

[40] B. Ardekani, J. Kershaw, M. Braun and I. Kanno, "Automatic Detection of the Mid-Sagittal Plane in 3-D Brain Images", *IEEE Trans. Med. Imag.*, 16(6), pp. 947-952, 1997.

[41] S. Gefan, Y. Fan, L. Bertrand and J. Nissanov, "Symmetry-based 3D Brain Reconstruction", in *Proc.* 2^{nd} *IEEE Int. Symp. on Biomedical Imaging*, Arlington, VA, 2004, pp. 744-747.

[42] L. Junck, J.G. Moen, G.D. Hutchins, M.B. Brown, and D.E. Kuhl, "Correlation methods for the centering, rotation and alignment of functional brain images", *J. Nucl. Med.*, 31(7), pp. 1220- 1226, 1990.

[43] W. H. Press, B. P. Flannery, S. A. Teukolsky and W. T. Vetterling, *Numerical Recipes in C: The Art of Scientific Computing*, Cambridge University Press, 1992.

[44] I.H. Shames, *Mechanics of deformable solids*, Prentice-Hall Inc., Englewood Cliffs, NJ, 1964.

[45] F.Y.M. Wan, *Introduction to the Calculus of Variations and its Applications*, Chapman & Hall, 1995.

[46] V.V. Patel, M.W. Vannier, J.L. Marsh and L.J. Lo, "Assessing Craniofacial Surgical Simulation", *IEEE Computer Graph. Appl.*, 16(1), pp. 46-54, 1996.

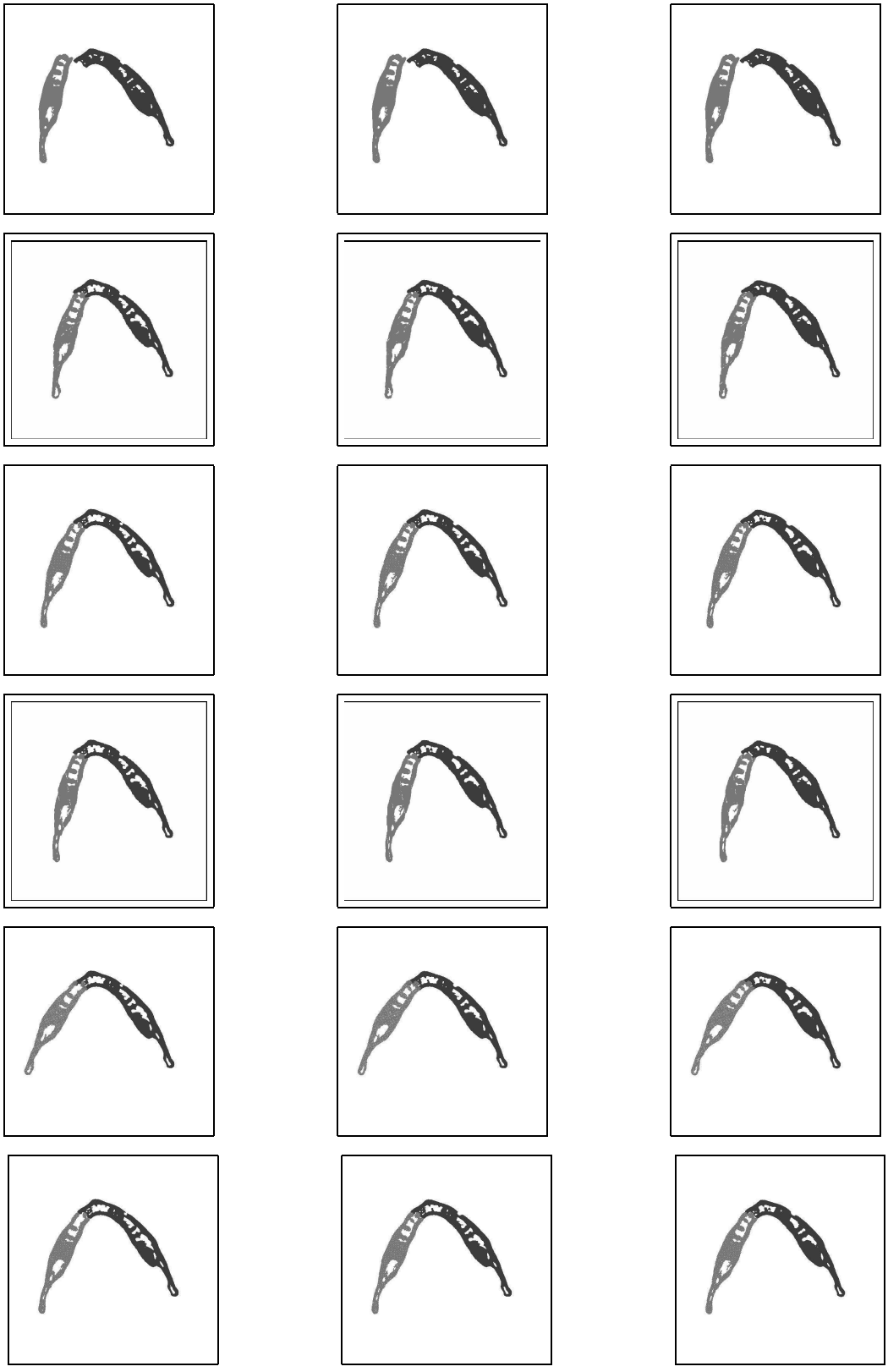

Figure 2.6: Slicewise Reconstruction of a Real Patient Mandible using DARCES (second row), ICP (third row), Hybrid DARCES-ICP (fourth row), Geometric (fifth row), Hybrid Geometric-iCP (sixth row) algorithms. The first row shows the two broken components.

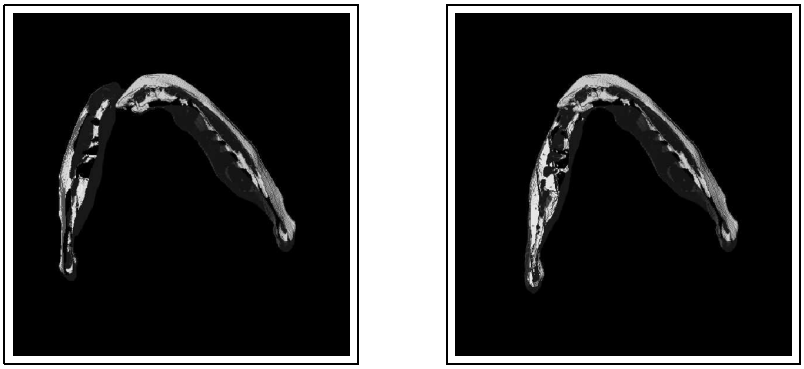

Figure 2.7: A Visual comparison of the rendered volume of the broken jaw and the reconstructed jaw (using hybrid DARCES-ICP algorithm)

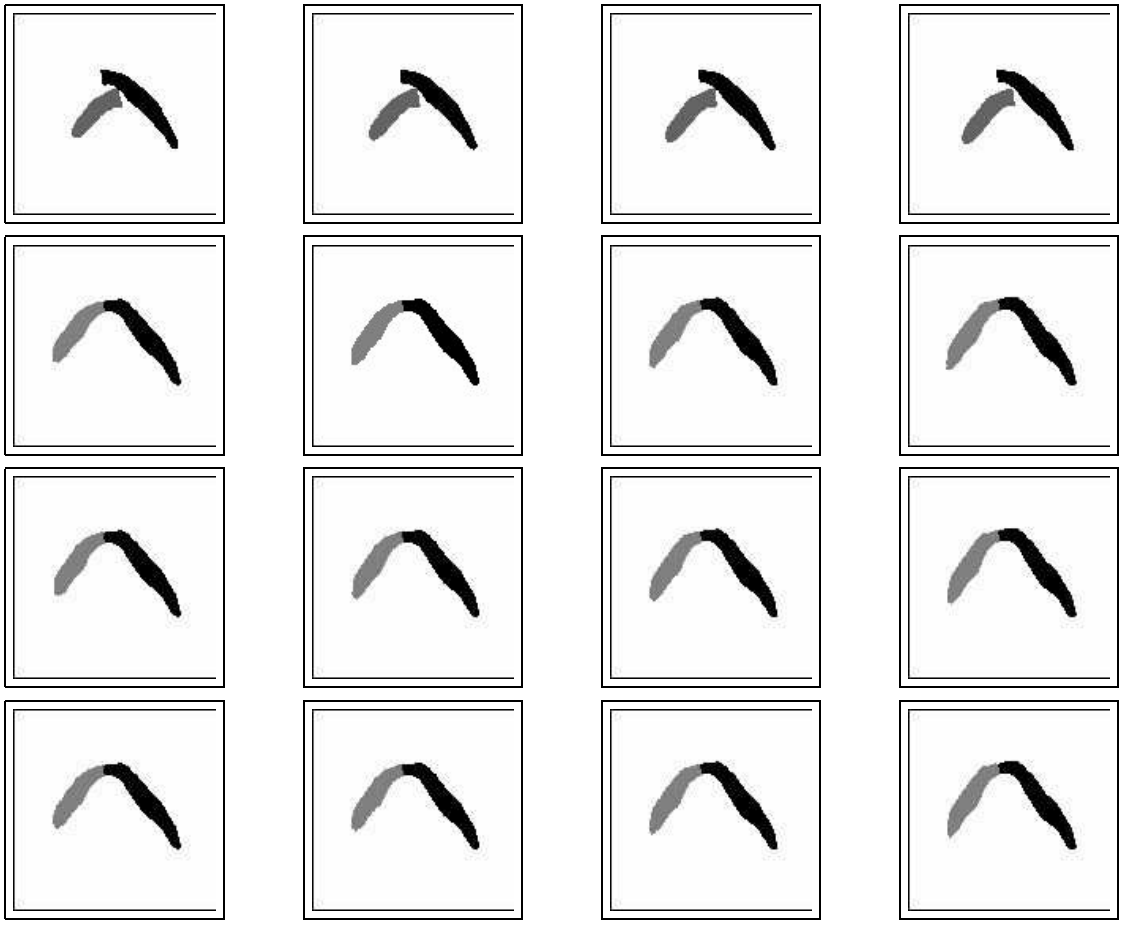

Figure 2.8: The first row represents broken mandible fragments in phantom CT slices. The second, third and fourth rows respectively represent reconstruction resulting from DARCES, ICP and hybrid DARCES-ICP algorithms.

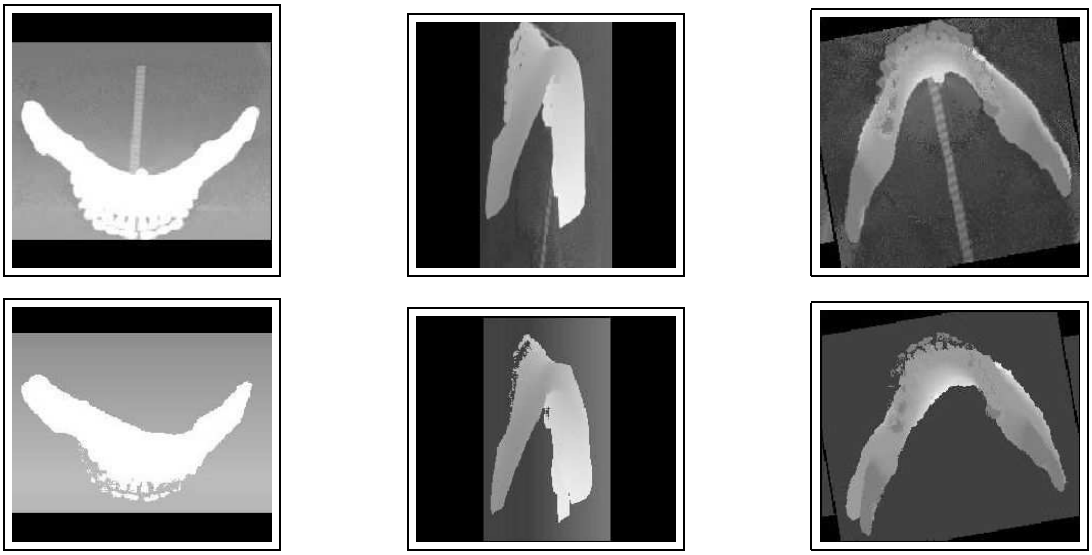

Figure 2.9: Comparison of the original and reconstructed mandibles. The top row is the original mandible and the bottom row is the reconstructed mandible obtained using hybrid DARCES-ICP algorithm. The first, second and the third columns represent the 3D projections along the x, y and z axes respectively.

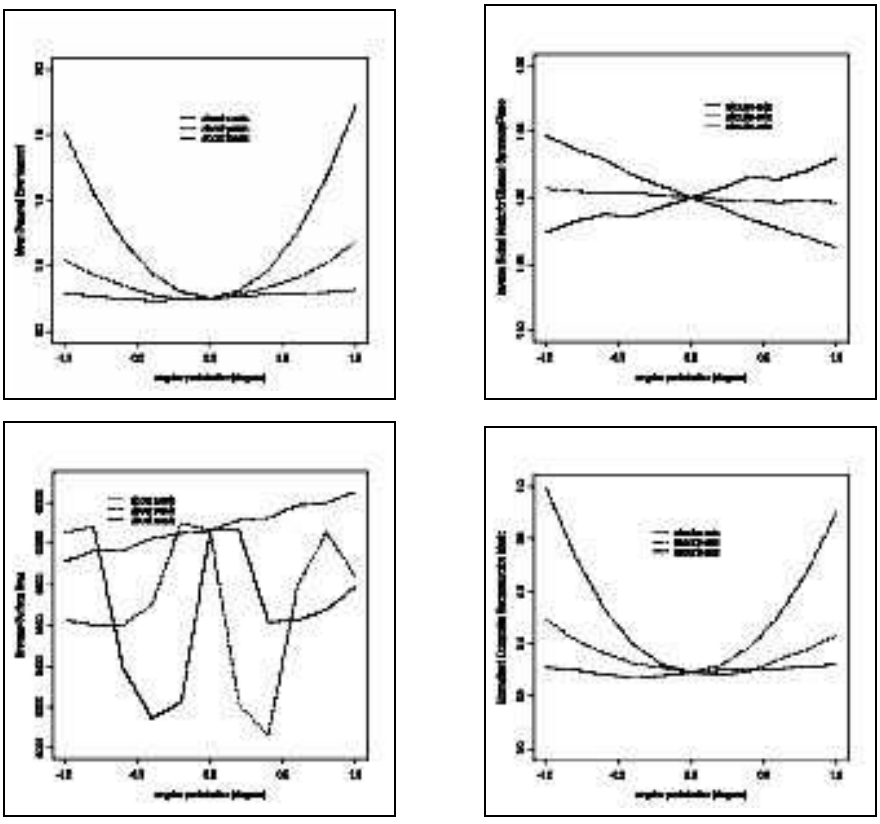

Figure 2.10: Variations in the MSE (ϵ^2) (top left), Inverse Coeff. of Sym. ψ^{-1} (top right), Average Surface Area $\bar{A}$ (bottom left) and Normalized CRM (bottom right) with angular perturbation along all the three major axes.

Chapter 3

Virtual Multi-fracture Mandibular Reconstruction based on Graph Matching

3.1 Motivation

The problem of reconstruction gets far more complex in case of multiple fractures. Subsequently, the cost of surgery becomes prohibitive with the increased operative time necessary to identify accurately the opposable fracture surfaces and thereby ensure an overall accurate reconstruction [1]. The problem becomes one of jigsaw puzzle solving and is of general interest with applications in various domains like forensic, archeology, earthenware assembly *etc.* The present work provides a novel two step solution to the virtual multi-fracture reconstruction problem, which can be easily extended to similar problems in other domains. In the first step, the opposable fracture surfaces are identified using the maximum weight graph matching algorithm for a weighted graph, and a pre-computed score matrix. In the second step, the opposable fracture surface pairs identified in the first step are registered using an improvised ICP algorithm, where the closest set is determined using the maximum cardinality minimum weight bipartite graph matching algorithm. The reconstruction process in the second step is constantly monitored using two simple but useful constraints based on the Tanimoto coefficient and concepts of volumetric matching.

3.2 Literature Review and Our Contribution

The multi-fracture reconstruction problem in a broader sense is a combinatorial pattern matching problem (we would show this explicitly in section 3.6). Hence, as a part of the literature review, we would first discuss the various existing approaches for solving a two-dimensional (2D) and a three-dimensional (3D) jigsaw puzzle problem. A very brief survey on

the importance of the multiple mandibular and related fractures, as appeared in the surgical literature is mentioned next.

As the number of references in this research field is quite high, we would restrict ourselves to a few representative works. The research on jigsaw puzzle solving by a computer using images, has started around twenty years ago with the work by Wolfson *et al.* [2]. In their seminal paper, they modeled the problem as a Traveling Sales Person (TSP) problem. Webster *et al.* [3] identifies isthmus critical points as robust global features for matching jigsaw puzzles. The isthmus critical points were extracted using medial axis transformation. Leitato and Stolfi used multi-scale filtering, an initial matching followed by refinement and pruning with incremental dynamic programming to solve the matching problem [4]. Yao and Shao [5] designed an algorithm which combines shape and image matching with a cyclic "growth" process that tries to place pieces in their correct positions. Goldberg *et al.*, [6] addressed the same problem of 2D jigsaw puzzle reconstruction with an emphasis on a global relaxation approach after detection of fiducial points (robust canonical locations). Makridis and Papamarkos proposed a new technique which employs both geometrical and color features for the jigsaw puzzle matching [7]. Barequet and Sharir in [8] used improved geometric hashing techniques for partial surface and volume matching in 3D. Ucoluk and Toroslu [9] addressed the 3D reconstruction problem from the point of view of matching two 3D space curves. Papaioannou *et al.* [10] formulated a novel matching error for solving the problem of 3D reconstruction through matching of their parts. They used a shape signature for that purpose. Huang *et al.* [11] used integral invariants in the process of geometrically matching fragmented 3D objects. Some other important 3D jigsaw puzzle solving approaches include the archaeological fragment assembly problem by Kampel and Sablantig [12], the 3D axially symmetric shapes in case of an earthenware assembly using Bayesian techniques by Willis and Cooper [13] *etc.*

In an article by Ogundare *et al.* [14], it is shown that 52% of the patients studied in an urban level trauma center, contained multiple mandibular fractures. In a study conducted by Boole *et al.* [15], about 30% of the duty army soldiers were shown to contain two or more fractures. Clauser *et al.* [16] discussed severe midface fractures as a result of vehicle accidents,

which could lead to clinical complexity. It is interesting to note that in their work on mutilple craniofacial injuries, Schettler *et al.* [17] illustrated that the technique of reconstruction is often tantamount to solving a puzzle.

The rest of this chapter is organized in the following way: section 3.3 is on image processing, section 3.4 deals with the formulation of a fracture surface score matrix, section 3.6 describes the identification of opposable fracture surfaces, section 3.7 discusses the pairwise registration of the fracture surfaces, section 3.8 is about monitoring the shape of the reconstructed mandible, section 3.9 describes the experimental results and finally in section 3.10 we draw the conclusion and mention the future research directions.

3.3 Image Processing

For multi-fracture reconstruction, the experimentation has been so far limited to phantom data. We are in the process of doing further experiments on real patient multi-fracture data. For the phantom data, simple thresholding followed by Connected Component Labeling is used to segment the broken mandibular fragments. Contour data is next extracted for the individual fracture surfaces, the aggregation of which produced the surface data. The details of these steps are omitted to avoid repetition and the reader can refer to section 2.4 for more information.

3.4 Design of a Score Matrix

A score matrix is constructed based on the appearance of various mandible fragments in the input CT image sequence. The mandible fragments are classified as *terminal* or *non-terminal*, based on the presence or absence of condyles (a craniofacial body part that exhibits pronounced sphericity) respectively. This type of prior rudimentary classification of the fragments to be assembled is along the same line of Wolfson *et al.* [2] and Goldberg *et al.* [6]. Both Wolfson *et al.* and Goldberg *et al.* separately assemble the *border* and *interior* frame pieces. In fact, Goldberg *et al.* further classified the border pieces into indents, outdents and flat sides. A terminal fragment in our case is similar to a border piece whereas a non-terminal

fragment corresponds to an interior piece. A terminal fragment is often found to contain a single fracture surface. On the contrary, a non-terminal fragment more frequently exhibits two fracture surfaces. In the present work, the experimentation and mathematical analysis is based on the above set-up i.e. a terminal fragment has one fracture surface and a non-terminal fragment has two fracture surfaces. However, our scheme is flexible enough to handle any number of fracture surfaces for a given fragment. Each fracture surface is represented by a collection of 3D data points obtained by extracting and collating the corresponding fracture contour points in the 2D CT image slices. In the case of 2D problems, the score matrix formulation is typically based on curve matching, where the matrix elements denote matches between potentially opposable edge points [18], [19]. In our case, we need to estimate the matching score between the 3D fracture surfaces extracted from the CT image slices. A high matching score is assigned to a pair of fracture surfaces if (a) they are determined to be spatially proximal, and (b) they are determined to exhibit complementary (opposable) fracture surface characteristics. We have used both of these factors in determining the matching score.

3.4.1 Mathematical formulation of spatial proximity

The various fracture surfaces possess a varying number of data points. The notion of a distance (as a measure of spatial separation) between any surface pair requires the establishment of correspondence between the data points. Given the dimension of the score matrix i.e. the number of possible fracture surface pairs for which the above correspondence has to be pre-established, the task of finding a distance measure becomes computationally very expensive. We therefore use the Hausdorff distance, which does not need a prior correspondence between the two data point sets to give a measure of spatial separation between them. The Hausdorff distance H(A, B) between two datasets A and B is given by [20]:

$$H(A, B) = max(h(A, B), h(B, A)) \tag{3.1}$$

where $h(A, B)$ denotes the *directed* Hausdorff distance between the two datasets A and B and is defined as:

$$h(A, B) = \max_{a \in A} \min_{b \in B} \|a - b\| \tag{3.2}$$

Here $\|a - b\|$ represents the Euclidean distance between the points a and b. Each such a, b in our case is a 3D data point in the fracture surface data set A and B respectively. The computation of the Hausdorff distance can be done trivially in $O(mn)$ i.e. quadratic polynomial time where m and n denote the cardinalities of the two fracture surface data sets.

3.4.2 Mathematical formulation of Surface Characteristics

There are some well-known measures of surface characteristics available in the standard computer vision literature. *Gaussian* and *Mean* curvatures are the most prominent among them [21]. Each fracture surface in the present scenario is a collection of several fracture contours. We also noticed that the calculation of the Gaussian and Mean curvatures are relatively computationally intensive and are more sensitive to noise as compared to contour curvature. This choice of contour curvature as a measure of surface irregularity is further boosted by the fact that it also enjoys rotational and translational invariance. The *contour curvature* for a point (x, y) in a given CT image slice (for a specific value of z) is given by [24]:

$$c(x, y) = (d^2y/dx^2)/(1 + (dy/dx)^2)^{3/2} \tag{3.3}$$

We now propose a function which captures the matching between two fracture surfaces using contour curvature. Note that such a function $FS(A, B)$ for a pair of surfaces A, B is the sum of the score $fs(a, b)$ for each possible point pair, one from each surface. If the two points under consideration have the same signs for their curvatures, then they cause the overall score for the surface to increase; otherwise they cause it to decrease. Thus, we can write:

$$FS(A, B) = \sum_{a \in A} \sum_{b \in B} fs(a, b) \tag{3.4}$$

Intuitively, the score $fs(a, b)$ between any pair of points a, b becomes high if (a) the slice-wise locations of two points are spatially proximal, and (b) the relative positions of the two points

in respective slices (estimated using the end-points of the slices as the reference points) are close and (c) the curvature values of the two points are close. The score will be low if any of the above criteria is not satisfied. So, we can quantitatively express $fs(a,b)$ as the product of the above three factors with a sign function:

$$fs(a,b) = S(a,b)E(a,b)C(a,b)sg(c_a c_b) \tag{3.5}$$

where

$$\begin{aligned} S(a,b) &= 2/(1+\exp(|s_a - s_b|)) \\ E(a,b) &= 2/(1+\exp(|e_a - e_b|)) \\ C(a,b) &= 2/(1+\exp(|c_a - c_b|)) \\ sg(c_a c_b) &= \begin{cases} +1 & \text{if } c_a c_b > 0 \\ -1 & \text{if } c_a c_b < 0 \end{cases} \end{aligned} \tag{3.6}$$

Here $S(a,b), E(a,b)$ and $C(a,b)$ respectively denote the *slice - wise*, *relative position within the slice - wise* and *curvature value - wise* scores of the two points a and b and $s_a(s_b), e_a(e_b), c_a(c_b)$ respectively denote the slice value, relative position value of the point in the slice and contour curvature value (given by equation (3.3)) of the point $a(b)$.

3.4.3 Elements of the Score Matrix

The elements of the score matrix $SC(A,B)$ are estimated as a linear combination of the inverse Hausdorff distance and the surface matching:

$$SC(A,B) = \lambda_1 H^{-1}(A,B) + \lambda_2 FS(A,B) \tag{3.7}$$

where the coefficients of the linear combination are determined from the following:

$$\begin{aligned} &\lambda_1 + \lambda_2 = 1 \\ &\lambda_1/\sigma(H^{-1}(A,B)) = \lambda_2/\sigma(FS(A,B)) \end{aligned} \tag{3.8}$$

In equation (3.8) $\sigma(H^{-1}(A,B))$ and $\sigma(FS(A,B))$ respectively denote the standard deviation of the terms $H^{-1}(A,B)$ and $FS(A,B)$ for all possible fracture surface pairs A and B. Let us denote the number of fracture surfaces by nfs and enumerate the fracture surfaces as $1, 2, ..., nfs$. Some properties of the score matrix under the present setup (i.e. two fracture

surfaces per non-terminal fragment and one fracture surface each per terminal fragment) are given below:

1. The score matrix is *real symmetric*
2. For two fracture surfaces $k, k+1$ of the same non-terminal fragment, $SC[k][k+1] = 0$ (two fractures of the same fragment cannot match)
3. The score matrix has its diagonal elements as zero i.e. $SC[k][k] = 0$ (no score is assigned for matching a fracture surface k to itself)
4. In presence of one or more non-terminal fragments (which means two or more non-terminal fracture surfaces), the two fracture surfaces belonging to the two terminal fragments cannot match i.e. $SC[1][nfs] = 0$.

3.5 Basics of Graph Matching

The purpose of the section is to make the reader familiar with basics of graph matching. Some definitions/concepts and three theorems (without proof) will be presented here. The reader is referred to well-known texts in graph theory like [22] and [23] *etc.* for proof and other details.

Definition 3.1 *A* **matching** *M of a graph $G = (V, E)$ is a subset of the edges with the property that no two edges of M share the same node.*

Definition 3.2 *If the edge weights of a graph are all unity, the matching problem essentially becomes a Cardinality Matching problem. A* **Maximum Cardinality Matching** *is a matching with maximum number of edges.*

Definition 3.3 *When the cardinality of a matching is $\lfloor |V|/2 \rfloor$, the largest possible in a graph with $|V|$ nodes, we say the matching is* **complete** *or* **perfect**.

Definition 3.4 *If the edge weights are given by a function $w : E \rightarrow \Re_+$ the weight of a matching is defined as $w(M) := \sum_{e \in M} w(e)$. The* **Maximum Weight Matching** *problem is to find a matching M in G that has maximum weight.*

Definition 3.5 *Edges of a graph in a matching are called* **matched** *edges; the other edges are called* **free**. *Similarly, the vertices that are not incident upon any matched edge are called* **exposed**; *the remaining vertices are called* **free**.

Definition 3.6 *A path* $p = [u_1, u_2, ..., u_k]$ *is called* **alternating**
if edges $[u_1, u_2], [u_3, u_4], ..., [u_{2j-1}, u_{2j}], ...$ *are free,*
where as $[u_2, u_3], [u_4, u_5], ..., [u_{2j}, u_{2j+1}]$ *are matched.*

Definition 3.7 *An alternating path* $p = [u_1, u_2, ..., u_k]$ *is called* **augmenting** *if both* u_1 *and* u_k *are exposed vertices.*

Theorem 3.1 *A matching* M *in a graph* G *is maximum if and only if there is no augmenting path in* G *with respect to* M.

Theorem 3.2 *The worst-case time-complexity of the Maximum Weight (MCMW) algorithm for a graph* $G = (V, E)$ *with* $|V| = n$ *is* $O(n^4)$.

Theorem 3.3 *The worst-case time-complexity of the Maximum Cardinality Minimum Weight (MCMW) algorithm for a bipartite graph* $G = (V_1 \cup V_2, E)$ *with* $|V_1| = |V_2| = n$ *is* $O(n^3)$.

The above theorem is same as theorem 1.1. It is repeated here for making this section on graph matching more complete.

3.6 Identification of Opposable Fracture Surfaces

In the first subsection of the present section, we will prove that the current reconstruction problem gets combinatorial in terms of number of reconstruction options. In the second subsection, using maximum weight graph matching, we will show how we can identify the juxtaposable fracture surface pairs in polynomial time.

3.6.1 Combinatorial Nature of the Reconstruction

Theorem 3.4 *Given that a non-terminal fragment has two fracture surfaces and a terminal fragment has one fracture surface, the number of possible reconstruction options rc_n where n is the total number of fragments is:*
$rc_n = (n-2)!2^{(n-2)}$

Proof: With n total fragments, the $(n-2)$ non-terminal fragments can be encountered in any of $(n-2)!$ possible orderings. Further, each non-terminal fragment can be oriented such that either of the fracture surfaces is the first in the sequence. This accounts for the factor $2^{(n-2)}$ in counting the possibilities. $\diamond$

The presence of a factorial and an exponential term in the already proved expression for rc_n clearly demonstrate the combinatorial explosion in terms of the number of reconstruction options. Thus, an exhaustive search for the identification of the opposable fracture surfaces is prohibited. Note that even for a reasonably smaller number of fragments e.g. $n = 6$, the number of reconstruction options becomes 384. We would like to mention that the analysis with the assumption of two fracture surfaces per non-terminal fragment and one fracture surface per terminal fragment is without loss of any generality.

3.6.2 Maximum Weight Graph Matching for restricting the Reconstruction Options

As mentioned in the literature review section, different types of algorithmic and computational geometry based approaches were undertaken in the past to restrict the number of options for the reconstruction. We used the *Maximum Weight Graph Matching (MWGM)* algorithm to solve the above problem. Now, we would state and justify the following claim about correct modeling of our reconstruction problem as a MWGM problem and generating polynomial time solution:

Claim 3.1 *Maximum Weight Graph Matching (MWGM) algorithm for a weighted graph correctly identifies a number of solution sets, where each individual solution set is guaranteed to include all the fracture surfaces given by a collection of unordered opposable fracture surface pairs, in polynomial time.*

Justification: The fracture surfaces are modeled as the vertices of a weighted graph $G = (V, E)$. The anatomical constraints precludes placement of edges between certain pairs of vertices and we can treat them as edges with zero edge-weight. A pre-computed real symmetric score matrix elements SC_{AB} (from equation (3.7)) are assigned the positive edge weights w_{AB} for each remaining edge $[v_A v_B] \in E$. The goal is to identify the sets of opposable fracture surfaces such that the sum of the matching scores is a maximum. The modeling of our original problem maps to the following well-known Maximum Weight Graph Matching (MWGM) problem in graph-theory i.e. given a weighted undirected graph $G = (V, E)$ with edge weights $w_{AB} \geq 0$, obtain a pairing of the vertices such that $\sum w_{AB}$ is maximum. The number of vertices for our graph is even and hence a complete/perfect matching is guaranteed i.e. a solution set will always include a possible pairing of all the (opposable) fracture surfaces. Furthermore, since the score matrix is symmetrical and the graph is undirected, the ordering of an individual pair of surfaces does not matter. Each successive solution set will lead to a decrease in the value of the $\sum w_{AB}$ compared to its previous solution. From Theorem 3.2, we know that the MWGM algorithm for a weighted non-bipartite graph G with n vertices (i.e. $n = |V|$), has $O(n^4)$ run-time complexity. If we generate k solution sets, where k is usually much less than n, then the time-complexity of our proposed solution is $O(kn^4)$, which is guaranteed to be in polynomial-time. $\diamond$

3.7 Pairwise Registration of the Fracture Surfaces

The fracture surface pairs are first registered using the ICP algorithm described in [25] with the incorporation of a novel graph-theoretic augmentation. The main steps in this augmented ICP algorithm [26] are as follows:

1. The matching points in one fracture surface data set, called the *model data set*, that correspond to points in the other fracture surface data set, called the *sample data set*, are determined and termed the *closest set*. The matching point pairs are determined using the MCMW bipartite graph matching algorithm [23]. The use of the MCMW graph matching algorithm obviates the need for any prior alignment of the two fracture surface data sets at the time of computing the *closest set* in the ICP algorithm.

2. The 3-D rigid body transformation computed using the closest set is applied to the original sample data set and the Mean Squared Error (MSE) between the transformed sample data points and the corresponding closest points is computed. The MSE (ϵ^2) is given by:

$$\epsilon^2 = (1/p)\sum_{i=1}^{p}((c_i - (Rs_i + T))^2) \tag{3.9}$$

where R denotes the rotation matrix, T denotes the translation vector, s_i denotes a point in the sample data set, c_i represents the corresponding point in the closest set and $p = \min\{|V_{1B}|, |V_{2B}|\}$.

The above two steps are repeated with an updated sample set (generated by applying R and T obtained at the current iteration to the current sample set) until a pre-specified error convergence criterion (0.01 in our case) is reached. Next, we will state a claim about the modeling of our problem as one of MCMW graph matching:

Claim 3.2 *Given that there is neither a reflection nor a very large (greater than* 90^o*) rotation (two extremely unlikely cases for a typical craniofacial injury), the Maximum Cardinality Minimum Weight (MCMW) algorithm for a bipartite graph correctly establishes the correspondence between two fracture surfaces at every stage of the Iterative Closest Point (ICP) algorithm in polynomial time.*

The above claim is same as 2.1. It is repeated here for the sake of completeness. However, for the justification of the claim, which is omitted here, the reader can revisit the section 2.5.2.

3.8 Shape Monitoring of the Reconstructed Mandible

Note that we have so far used a) a score matrix favorable to an optimal solution and b) a non-greedy MWGM algorithm to solve the problem of multi-fracture reconstruction. In this section, we use the global shape knowledge of a human mandible to monitor the step-by-step reconstruction process. The existing research on jigsaw puzzle assembly mentions about this type of verification. For example, Burdea and Wolfson in their work [27] discussed robotic verification following the machine vision and the combinatorial optimization techniques. Our overall strategy in solving this multi-fracture reconstruction problem is somewhat similar. From the MWGM algorithm, we can generate multiple solution sets. Each solution set is a collection of fracture surface pairs. The approach is to start with the best solution set and do some shape checking after every additional fracture surface pair is registered. At any point in the reconstruction stage if the shape matching constraint(s) is(are) violated, we abandon the current solution and restart the registration with the next best solution of the MWGM algorithm. Since the outcome of the reconstruction is known from the beginning, we can actually use something similar to the outcome as a reference. We used an unbroken human jaw as a reference for our purpose. Subsequently, we compared the partially reconstructed jaw at every stage of the reconstruction with the unbroken reference. There exists various computer vision literature for shape matching e.g. see [28], [29] *etc.* We employed two constraints based on Tanimoto coefficient in the context of volumetric matching. The Tanimoto coefficient $TC_{f,g}$ between two volumetric shapes f and g is defined as [30]:

$$TC_{f,g} = O_{f,g}/(I_f + I_g - O_{f,g}) \tag{3.10}$$

where

$$I_f = \int\int\int f^2(\hat{x},\hat{y},\hat{z})dxdydz \tag{3.11}$$

$$I_g = \int\int\int g^2(\tilde{x},\tilde{y},\tilde{z})dxdydz \tag{3.12}$$

$$O_{f,g} = 2\int\int\int f(\hat{x},\hat{y},\hat{z})g(\tilde{x},\tilde{y},\tilde{z})dxdydz \tag{3.13}$$

Here $(\hat{x},\hat{y},\hat{z}) = (x - x_{RC}, y - y_{RC}, z - z_{RC})$ and $(\tilde{x},\tilde{y},\tilde{z}) = (x - x_{SC}, y - y_{SC}, z - z_{SC})$ respectively represent the points of the reference mandible R and the reconstructed mandible

S with respect to their individual centroids (x_{RC}, y_{RC}, z_{RC}) and (x_{SC}, y_{SC}, z_{SC}). Thus, we can write the following:

$$f(\hat{x}, \hat{y}, \hat{z}) = \begin{cases} 1 & \text{if } (\hat{x}, \hat{y}, \hat{z}) \in R \\ 0 & \text{otherwise} \end{cases} \tag{3.14}$$

$$g(\tilde{x}, \tilde{y}, \tilde{z}) = \begin{cases} 1 & \text{if } (\tilde{x}, \tilde{y}, \tilde{z}) \in S \\ 0 & \text{otherwise} \end{cases} \tag{3.15}$$

Now, we state and justify the following claim about the volumetric matching based constraints derived from the above equations (3.10 - 3.15).

Claim 3.3 *The following two volumetric matching-based shape constraints at any stage should decide the correctness of the reconstruction:*

1. *$TC_{f,g}$ is monotonically non-decreasing*

2. *$2I_g - O_{f,g} \leq 2qI_g$ where q is a small positive number*

Justification: At each stage of reconstruction, one more bone fragment is getting added to the already reconstructed mandible thus far. This ensures that the value of $TC_(f, g)$ cannot decrease. Sometimes a fragment can at most keep the value of $TC_{f,g}$ the same as that in the previous stage. If the value of $TC_(f, g)$ is found to decrease at any stage, then we are definitely in a wrong direction. Thus the claim in (a) i.e. $TC_{f,g}$ should be monotonically non-decreasing to indicate correct reconstruction, is justified.

Note that the reference mandible remains the same throughout and the reconstructed mandible increases in volume at successive stages of reconstruction. Furthermore, both the reference and the reconstructed mandibles under consideration are binary objects. It becomes quite evident from the equations (3.10 - 3.15) that at any stage, the extent of the volumetric overlap O_{fg} should be exactly twice that of the reconstructed volume I_g. Then, we can write $1 - O_{fg}/2I_g < q$. Multiplying both sides by $2I_g$, we get the result. $\diamond$

3.9 Analysis of Experimental Results

A typical input CT image sequence has six broken human mandible fragments with a total of ten fracture surfaces. The two fracture surfaces belonging to the terminal fragments are numbered 1 and 10 and the remaining eight fracture surfaces of the non-terminal fragments are numbered from 2 to 9.

Score Parameter Extremes	Value	Fracture Surface Pair
Min. Hausdorff Distance	29.83	$(5, 6)$
Max. Hausdorff Distance	185.12	$(1, 9)$
Max. Surface Match	955.55	$(1, 4)$
Min. Overall Score	1	$(4, 9)$
Max. Overall Score	1362	$(1, 4)$

Table 3.1: Extreme Score Parameter Values

Table (3.1) shows the extreme values of the Hausdorff distance, the surface match function and the overall score amongst all possible fracture surface pairs. The surface match values are normalized so that the minimum value is 1.0 before using them in equation (3.7) to ensure all positive weights for the graph. The overall score elements are also rounded to their nearest integer values for the graph matching algorithm. For the present CT image sequence, the surface match clearly dominates the overall score. However, for a different CT image sequence with fairly similar fracture surface characteristics, the spatial proximity of the fracture surfaces could easily be more decisive. This justifies the inclusion of the Hausdorff distance term in the overall score.

Solution Set (j)	Score of the j^{th} solution set (W_j)
$((1, 4), (2, 5), (3, 6), (7, 8), (9, 10))$	4987
$((1, 3), (2, 9), (4, 6), (5, 7), (8, 10))$	3123

Table 3.2: Results from the Graph Matching Algorithm

Table (3.2) shows the solution set obtained from the MWGM algorithm along with the sum of the edge weights for each solution set. We chose $p = 0.1$, which in this case led to termination after obtaining two best solution sets based on equation (3.11).

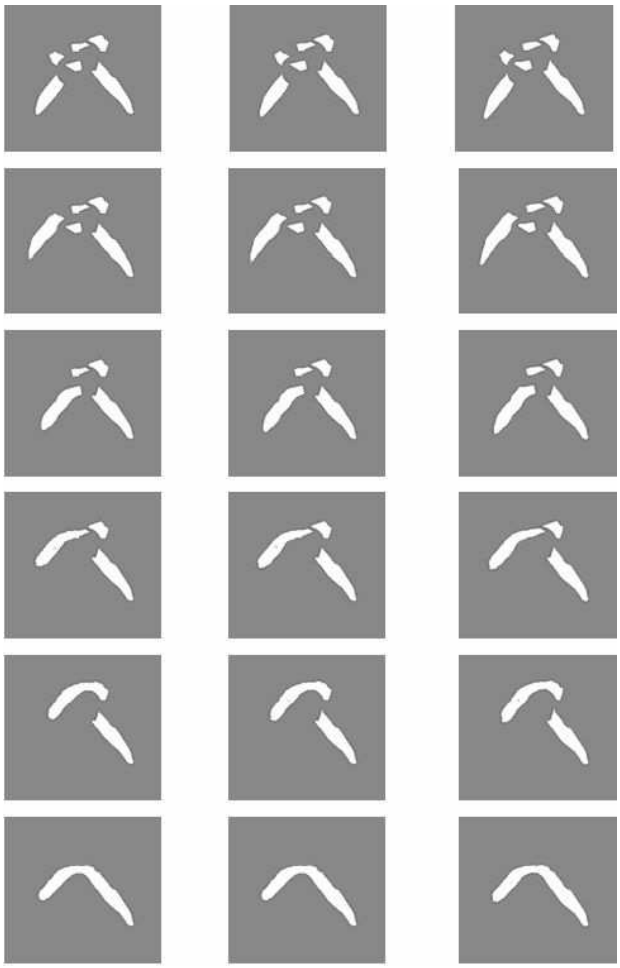

Figure 3.1: Different Stages of a Multi-fracture Reconstruction

Figure (3.1) describes the various stages of the reconstruction with the best solution set (obtained from row 1 of table (3.2)) using the improvised ICP algorithm described in Section 3.7. The first row shows three successive images in the original CT sequence with six broken fragments or components (denoted by bright intensity values), obtained after preprocessing the original CT image sequence. Each of the later five rows shows the same three images with a new pair of fracture surfaces registered at each stage.

Table (3.3) describes the results of the step-by-step shape monitoring of the partially reconstructed mandible at various stages of reconstruction. At each stage, both the shape

Various Stages of Reconstruction	TC_{fg}	$A = \frac{(2I_g - O_{f,g})}{2I_g}$
$(1,4)$ registered	1.08	0
$(1,4),(2,5)$ registered	1.47	0
$(1,4),(2,5),(3,6)$ registered	1.57	0
$(1,4),(2,5),(3,6),(7,8)$ registered	1.69	0
$(1,4),(2,5),(3,6),(7,8),(9,10)$ registered	1.69	0.0003

Table 3.3: Results of shape Monitoring at Various Stages of the Reconstruction Process

constraints (defined in Section 3.8) are satisfied with a choice of $q = 0.01$. Thus, we proceed with the best solution of the MWGM algorithm to complete the registration of all five fracture surface pairs.

3.10 Conclusion and Future Research

We have addressed an important problem of virtual craniofacial reconstruction in the area of biomedical pattern analysis. The present problem is appealing from both application and theoretical standpoints. As far as the application is concerned, the fast and accurate reconstruction of human mandible from several broken pieces poses a severe challenge for a practicing surgeon. On the contrary, from the theoretical perspective, the problem resembles that of a 3D jigsaw puzzle assembly which necessitates efficient handling of combinatorial pattern matching. We employed computer vision and graph matching to solve this extremely challenging problem. A score matrix is first constructed using a linear combination of inverse Hausdorff distance and a function based on contour curvature. MWGM algorithm was used next to identify the opposable fracture surface pairs. The individual fracture surface pairs were registered using MCMW bipartite graph matching algorithm. Finally, the overall reconstruction process was continuously monitored by some shape constraints based on Tanimoto coefficient. The proposed solution has the potential to considerably reduce the operative time, operative cost and patient trauma during actual craniofacial surgery.

One direction of future research is to extend the proposed solution for virtual craniofacial reconstruction to other areas of reconstructive surgery involving multiple fractures. The score matrix design in such cases can be made more appropriate using the relevant domain knowledge. We have so far used pure volumetric matching for monitoring the reconstruction. However, the use of active shape models by Cootes *et al.* [31] or parametric shape models by Gong *et al.* [32] can provide more flexibility. We also plan to carry out future research along these lines.

3.11 References

[1] C. Zahl, D. Muller, S. Felder and K.L. Gerlach, "Cost of miniplate osteosynthesis for treatment of mandibular fractures: a prospective evaluation", *Gesundheitswesen*, vol. 65, no. 10, pp. 561-565, 2003.

[2] H. Wolfson, E. Schonberg, A. Kalvin and Y. Lamdan, "Solving Jigsaw Puzzles by Computer", *Ann. Oper. Res.*, vol. 12, pp. 51-64. December 1988.

[3] R.W. Webster, P.S. LaFollette and R.L. Stafford, "Isthmus Critical Points for Solving Jigsaw Puzzles in Computer Vision", *IEEE Trans. Syst., Man and Cybern.*, vol. 21, no. 5, pp. 1271 - 1278, Sept./Oct. 1991.

[4] H. Christina da Gama Leitao and J. Stolfi, "A Multiscale Method for the Reassembly of two-Dimensional Fragmented Objects", *IEEE Trans. Pattern Anal. Machine Intell.*, vol.24, no. 9, pp. 1239 - 1251, September 2002.

[5] F.H. Yao and G.F. Shao, "A shape and image merging technique to solve jigsaw puzzles", *Pattern Recognit. Lett.*, vol. 24, no. 12, pp. 1819 - 1835, August 2003.

[6] D. Goldberg, C. Malon and M. Bern, "A Global Approach to Automatic Solution of Jigsaw Puzzles", *Comput. Geom. - Th. and Appl.*, vol. 28, no. 3, pp. 165-174. 2004.

[7] M. Makridis and N. Papamarkos, "A new technique for solving a jigsaw puzzle", *Proc. Thirteenth IEEE Int. Conf. On Image Processing (ICIP)*, pp. 2001 - 2004, Atlanta, USA, 2006.

[8] G. Barequet and M. Sharir, "Partial Surface and Volume Matching in Three Dimensions", *IEEE Trans. Pattern Anal. Machine Intell.*, vol. 19, no. 9. pp. 929 - 948, Sept. 1997.

[9] G. Ucoluk and I. Toroslu, Automatic reconstruction of broken 3D surface objects, *Comput. Graph.*, vol. 23, pp. 573 - 582. 1999.

[10] G. Papaionnou, E. Karabassi and T. Theoharis, "Reconstruction of Three-Dimensional Objects through Matching of Their Parts", *IEEE Trans. Pattern Anal. Machine Intell.*, vol. 24, no. 1, pp. 114 - 124, Jan. 2002.

[11] Q.X. Huang, S. Flory, N. Gelfand, M. Hofer and H. Pottmann, "Reassembling Fractured Objects by Geometric Matching", *ACM Trans. Graph.*, vol. 25, no. 3, pp. 569 - 578, 2006.

[12] M. Kampel and R. Sablantig, "On 3D Mosaicing of Rotationally Symmetric Ceramic Fragments", *Proc. Seventeenth IAPR Int. Conf. On Pattern Recognition (ICPR)*, Cambridge, U.K., pp. 265 - 268, 2004.

[13] A. Willis and D. Cooper, "Bayesian Assembly of 3D Axially Symmetric Shapes from Fragments", *Proc. Sixth IEEE Int. Conf. On Computer Vision Pattern Recognition (CVPR)*, Washington D.C., USA, pp. 82 89, 2004.

[14] B.O. Ogundare, A. Bonnick and N. Bayley, "Pattern of Mandibular Fractures in an Urban Major Trauma Center", *J. Oral Maxillofac. Surg.*, vol. 61, no. 6, pp. 713-718, June 2003.

[15] JR. Boole, M. Holtel, P. Amoroso and M. Yore, "5196 mandible fractures among 4381 active duty army soldiers, 1980 to 1998", *Laryngoscope*, vol. 111, no. 10, pp. 1691-1696, October 2001.

[16] L. Clauser, M. Galie, S. Mandrioli, E. Sarti, "Severe Panfacial Fracture With Facial Explosion: Integrated and Multistaged Reconstructive Procedures", *J. Craniofac. Surg.*, vol. 14, no. 6, pp. 893-898, November 2003.

[17] D. Schettler, K. Roosen, J. Heesen1 and R. Kalff, "Timing and techniques of reconstruction and stabilization of combined craniofacial injuries", *Neurosurg. Rev.*, vol. 12, no. 1, March, 1989.

[18] J.T. Schwartz and M. Sharir, "Identification of partially obscured objects in two dimensions by matching of noisy characteristic curves", *Int. J. Rob. Res.*, vol. 6, no.2. pp. 29 - 44, 1987.

[19] H. Wolfson, "On Curve Matching", *IEEE Trans. Pattern Anal. Machine Intell.*, vol. 12, no. 5, pp. 483 - 489, May 1990.

[20] D.P. Huttenlocher, G.A. Klanderman and W.J. Rucklidge, "Comparing Images Using the Hausdorff Distance", *IEEE Trans. Pattern Anal. Machine Intell.*, vol. 15, no. 9, 850 863, Sept. 1993.

[21] R.W.I. Yarger and F.K.H. Quek, "Surface parameterization in volumetric images for feature classification", *Proc. of IEEE Int. Symp. on Bio-Informatics and Biomedical Engineering*, 297 - 303, Washington, D.C., USA, 2000.

[22] C.H. Papadimitriou and K. Steiglitz, *Combinatorial Optimization: Algorithms and Complexity*, Prentice Hall of India; 1982.

[23] N. Christofides, *Graph Theory An Algorithmic Approach*, Academic Press; 1975.

[24] L.F. Costa and R.M. Cesar Jr., *Shape Analysis and Classification, Theory and Practice*, CRC Press; 2000.

[25] P.J. Besl and N.D. McKay, "A Method for Registration of 3-D Shapes", *IEEE Trans. Pattern Anal. Machine Intell.*, vol. 14, no. 2, pp. 239-256, Feb. 1992.

[26] A.S. Chowdhury, S.M. Bhandarkar, R.W. Robinson and J.C. Yu, "Virtual Craniofacial Reconstruction from Computed Tomography Image Sequences Exhibiting Multiple Fractures", *Proc. of Thirteenth IEEE Int. Conf. on Image Processing (ICIP)*; pp. 1173 - 1176; Atlanta, GA, Oct. 2006.

[27] G.C. Burdea and H.J. Wolfson, "Solving Jigsaw Puzzles by a Robot", *IEEE Trans. Rob. Autom.*, vol. 5, no. 6, Dec. 1989.

[28] R. C. Veltkamp, "Shape Matching: Similarity Measures and Algorithms", *Proc. of IEEE Int. Conf. on Shape Modeling & Applications*, pp. 188 - 189, Genova, Italy, 2001.

[29] S. Belongie, J. Malik and J. Puzicha, "Shape Matching and Object Recognition Using Shape Contexts", *IEEE Trans. Pattern Anal. Machine Intell.*, vol. 24, no. 4, Apr. 2002.

[30] E.J. Mills and P.M. Dean, "Three-dimensional hydrogen-bond geometry and probability information from a crystal survey", *J. Comput-Aided Mol. Des.*, vol. 10, no. 6, pp. 607 -622, 1996.

[31] T.F. Cootes, D. Cooper, C.J. Taylor and J. Graham, "Active Shape Models - Their Training and Application", *Comput. Vis. Im. Understand.*, vol. 61, no. 1, pp. 38 - 59, 1995.

[32] L. Gong, S. D. Pathak, D. H. Haynor and Y. Kim, "Parametric shape modeling using deformable superellipses for prostate segmentation", *IEEE Trans. Med. Imag.*, vol. 23, no. 3, pp. 340-349, 2004.

Chapter 4

Hairline Fracture Detection and Target Pattern Generation using MRF and Bayesian Image Restoration

4.1 Introduction

In this chapter, we would focus on detection of hairline or minor fractures. Mandibular fractures are observed to possess certain distinct patterns in X-ray or CT images [1]. In some cases, the fractures are observed to be hairline or minor in nature. By the terms *hairline fracture* or *minor fracture* we respectively refer to those situations where the broken bone fragments are not visibly out of alignment or have incurred very little relative displacement. The presence of noise makes the detection and subsequent visualization of such types of fractures in X-ray or CT images a very challenging task. In case of a *major fracture*, i.e., fractures where the broken fragments are clearly displaced relative to each other, surgical intervention is almost mandatory. However, in the case of a *hairline/minor fracture*, the decision regarding surgical intervention is less clear as a surgeon can rely on natural bone healing. We propose a Markov Random Field (MRF)- Maximum A Posteriori probability (MAP) based scheme for (a) mandibular hairline fracture detection in the presence of noise and (b) target pattern generation for hairline/minor fractures. The target pattern depicts how a jaw with a hairline fracture would appear if allowed to heal naturally without explicit surgical intervention. This *in silico* reconstructed pattern may have potential prognostic significance because surgeons can decide if open surgical reduction and fixation is necessary or the fractures can be managed by allowing them to heal spontaneously based on what the naturally healed mandible will look like. For a major single fracture or multiple fractures that are visibly out of alignment, the proposed technique can be used as a smoothing technique at the sites where the opposable bone fragments have been brought into coarse

registration. This would result in the generation of a smooth or continuous 3D model of the reconstructed jaw where the individual bone fragments are fused together during free-form solid fabrication. Note that a 3D model is essential for pre-adaptation of the prostheses needed to stabilize the fractures and for performing the necessary biomechanical analysis to validate the virtual reconstruction of the fractured mandible or craniofacial skeleton along with the affixed prostheses.

From the standpoint of computer vision and pattern recognition research, the problems of hairline fracture detection and target pattern generation are of significant interest. Conventional corner detection techniques for determining points of surface discontinuity, such as the Harris detector [2], do not perform well because of the pronounced intensity inhomogeneity and noise present in X-ray or CT images. In the proposed scheme, hairline fracture detection and target pattern generation are simultaneously achieved by a process of implicit image restoration. The visual comparison of an X-ray or CT image of a mandible containing a hairline/minor fracture with that of an unbroken (intact) mandible reveals changes in pixel intensity only in the vicinity of the fracture site. This results in the formulation of an image restoration problem with a *partially unknown local* degradation. This is in sharp contrast to the more conventional image restoration problem with a *known global* degradation as outlined by Geman and Geman in their classical paper [3].

The proposed scheme takes as input a stack of 2D CT image slices of a human mandible with a hairline fracture. A two-step approach is taken where, in the first step, a hairline fracture is approximately localized within a block of pixels by exploiting the (approximate) bilateral symmetry of the human mandible and by using statistical correlation of the pixel intensities as a measure of intensity mismatch. An MRF modeling approach coupled with MAP estimation, is employed within the localized pixel blocks in the second step to detect the fracture and generate the target pattern with high accuracy.

4.2 Related Work and Our Contribution

In this section, we first mention some of the existing applications of MRF modeling and Bayesian restoration in the area of medical image analysis. Existing approaches for fracture detection in X-ray/CT images are described next. The theoretical and practical importance of the proposed scheme are discussed subsequently. The two classical applications of MRF-MAP paradigm for Bayesian image restoration can be found in Geman and Geman [3] and Besag [4]. MRF-based techniques have gained popularity in the past decade for solving various biomedical imaging problems. Some interesting applications include MRF-based image reconstruction for SPECT images by Lee *et al.* where they used an MRF for a spatial smoothness regularizer [5]; 3D MRF-based volumetric object reconstruction in Magnetic Resonance (MR) images by Choi *et al.* [6]; multiresolution MRF for tumor detection in mammograms by Zheng and Chan [7]; contextual clustering for analysis of functional MR (fMR) images using an MRF prior by Salli *et al.* [8]; segmentation of MR brain image data using MRF and a Gibbs prior by Chen and Metaxas [9]; matching of digital mammograms using Markovian (and variational) approaches by Richard [10]; penalized least square technique for Borehole Tomography using an MRF and a Gibbs prior by Popa and Zdunek [11]; contour detection of human kidneys using MRF and active contours [12] and reconstruction of MR images from raw Fourier data where an MRF is used to enforce spatial smoothness by Raj *et al.* [13].

Existing published literature on fracture detection in X-ray/CT images describes use of various approaches such as exploitation of anatomical knowledge combined with a *divide-and-conquer* approach by Ozanian and Philips [14]; texture analysis by Yap *et al.* [15]; an adaptive interface agent with neural networks by Syiam *et al.* [16]; an affine morphological scale space along with iterative peak detection and modified Hough transform by Donnelley and Knowles [17]; probabilistic combination of various classifiers by Lum *et al.* [18] and an active contour modeling coupled with shape constraints by Jia and Jiang [19]. An example of semi-automated fracture detection scheme for the class of well-displaced fractures can be found in Chowdhury *et al.* [20].

To the best of our knowledge, the classical MRF-MAP paradigm has not been previously applied to the problem of fracture detection in medical images (X-ray or CT) in general. From a biomedical imaging perspective, the proposed two-phase MRF-MAP based scheme addresses some important clinical problems such as hairline fracture detection and target pattern generation with accompanied prognosis of fracture healing. The proposed MRF-MAP paradigm is shown to handle input noise in an explicit and efficient manner. The approximate localization of fractures within pixel blocks in the first phase is shown to result in significant computational savings in the second phase since the MRF modeling and MAP estimation using Gibbs sampling, is restricted only to those pixel blocks in the CT image stack which are known to contain potential fractures. From a theoretical standpoint, the proposed scheme extends the conventional MRF-MAP paradigm to deal with a *partially unknown local* degradation of image pixel intensities at the fracture site. This is in contrast to the conventional MRF-MAP paradigm which incorporates a *global* and *known* deformation model. The proposed scheme for hairline fracture detection is also designed to perform an implicit restoration of the broken mandible at the fracture sites, thus offering the surgeon a prognostic view of the bone healing process.

The rest of the chapter is organized as follows: in Section 4.3 we discuss the method used for fracture localization; in section 4.4 we discuss some basic statistical concepts; in Section 4.5 we describe the Bayesian restoration framework; Section 4.6 contains the description and analysis of the experimental results; Section 4.7 concludes the chapter and outlines the directions for future research.

4.3 Fracture Localization

The input to the proposed fracture detection scheme is a stack of 2D CT image slices of the human mandible with a hairline fracture. Each 2D CT image slice is assumed to be parallel to the xy plane whereas the z axis is assumed to be the axial direction along which the CT image slices are acquired. The CT image stack is divided into a number of pixel blocks.

The fracture localization phase which constitutes the first phase of the proposed two-phase scheme, is decomposed into three sub-phases as follows:

4.3.1 Localization of the Mandible

Different anatomical structures within the human body are known to possess different types of symmetry [21]. In the context of our problem, we exploit the (approximate) bilateral symmetry exhibited by the human mandible. In the case of a hairline/minor fracture, the bilateral symmetry of the mandible is still preserved to a great extent despite the presence of the fracture. The general equation of a 3D plane (of bilateral symmetry) is given by:

$$Ax + By + Cz = D \tag{4.1}$$

For an axial CT scan of the human mandible we assumed B and C to be approximately equal to zero. and the mandibular cross-section to be approximately centered within each CT image slice of width W. Thus, the equation of the approximate plane of bilateral symmetry reduces to:

$$x = W/2 \tag{4.2}$$

Now, for every incident pixel g_i with coordinates (x, y, z) in the left half of the mandible with a hairline fracture, a bilaterally symmetric pixel g_i^R with coordinates (x^R, y^R, z^R) can be determined as:

$$x^R = W - x,\ y^R = y,\ z^R = z \tag{4.3}$$

Two heuristics are exploited to reduce the search space for coarse fracture localization. These heuristics along with their justifications (based on domain knowledge) are given below:

1. Since mandibles are essentially bone structures that typically exhibit higher intensity (i.e. Hounsfield unit) values in CT images, we seek pairs of pixel blocks with high average intensity. This helps to remove pixel blocks containing artifacts and/or large amounts of soft tissue from further consideration.

2. The mandible is typically larger in size compared to other bones in the CT images of the craniofacial skeleton. Since we are primarily interested in detecting mandibular

fractures, we perform a second round of filtering by applying the connected component labeling algorithm, at the pixel block level rather than at the level of individual pixels, and eliminating components which span only a small number of pixel blocks.

By using the above heuristics, we basically retain only a few (say q) pixel blocks which are deemed to constitute solely the fractured mandible.

4.3.2 Identification of the Appropriate Symmetric Block(s)

Having localized the mandible in the CT image, the next goal is to localize the fracture within it. This is done by taking a block from the left half of the image, all of whose pixels have x coordinate values: $0 \leq x \leq W/2$, and a corresponding bilaterally symmetric block in the right half of the image, all of whose pixels have x coordinate values $W/2 \geq x \geq W$, and computing the statistical correlation between the two. The correlation coefficient between a typical incident block g, with individual pixels g_i, and its bilaterally symmetric counterpart g^R, with corresponding pixels g_i^R is given by:

$$r(g, g^R) = \frac{1}{(n-1)} \sum_{i=1}^{n} (\frac{g_i - \bar{g}}{s_g})(\frac{g_i^R - \bar{g}^R}{s_g^R}) \tag{4.4}$$

where $\bar{g}$ and $\bar{g}^R$ denote the mean, and s_g and s_g^R denote the standard deviation of the pixels within the blocks g and g^R respectively.

Having obtained a value of $r(g, g^R)$ for each pair of pixel blocks (g, g^R), the pixel block pairs are sorted in increasing order of their $r(g, g^R)$ values. Note that the pixel block within the intact (unbroken) half of the mandible will have more pixels with higher intensity values (due to the presence of more bone material) compared to its bilaterally symmetric counterpart which contains the hairline fracture (resulting in some loss of bone material). Thus, the underlying rationale is that pairs of pixel blocks which potentially contain fractures should exhibit a higher intensity mismatch and hence lower correlation values. The user can then choose the best k out of q pixel blocks as sites containing potential hairline fractures. The above technique for coarse fracture localization provides the following two advantages:

1. It achieves computational efficiency by effectively reducing the image size over which the proposed MRF-MAP scheme coupled with Gibbs sampling is to be applied. Thus,

instead of applying the proposed MRF-MAP scheme over the entire CT image slice, we do so only over the selected k pixel blocks in each CT image slice.

2. It renders the prior shape information in each CT image slice more relevant and more accurate. Instead of determining two quadratic polynomials to describe the inner contour and outer contour of the entire mandible, we now only need to determine the quadratic polynomials that describe the inner and outer contours of the portion of the mandible that appears within the selected set of k pixel blocks.

4.3.3 Identification of the Fracture Site

After corresponding pairs of blocks are determined on both the halves of the approximate plane of symmetry in the CT scans, we identify the fracture site using the following three clinical observations:

1. In some CT scans, the fracture sites are marked by the presence of pixel regions with distinctly low intensity values (as compared to those of the bone fragments and soft tissue). When the soft tissue integrity is violated (due to the impact of the injury), air can enter the deeper tissue planes and form these low intensity regions, known as *emphysema*. The reason *emphysema* appears as dark (low-intensity) spots in the CT scans is due to its low electron density [22], [23].

2. The fracture sites in most of the CT scans are accompanied by *swelling of the soft tissue* in its vicinity. When tissue injury occurs, the resulting inflammation increases the capillary permeability in the region. This results in transudate and exudate formation, which is manifested in the form of soft tissue swelling [22], [23].

3. The hairline/minor fractures are essentially marked by loss of bone (i.e. high intensity) pixels. Thus, given the fact that the localized fracture blocks are (approximately) bilaterally symmetrical, the fractured half should typically contain a lower number of bone pixels within the localized area (from phase-I).

We first check for *emphysema* within the localized blocks in the CT slices. Obviously, the image half which contains the *emphysema* is designated as the one containing the hair-line/minor fracture. In cases, where *emphysema* is absent, we look for *soft tissue swelling*. The image half in which the *soft tissue swelling* is present, is deemed to contain the fracture. In cases, where *emphysema* is absent and *soft tissue swelling* is not particularly prominent (an extremely unlikely case from a clinical viewpoint; we have found only a single such case in our datasets), we count the bone pixels within the localized blocks in the two image halves and conclude that the image half containing the fewer number of bone pixels is the one containing the fracture.

4.4 Statistical Foundation

This section is devoted to different statistical concepts, used later in the chapter. We follow the notations of [24]:

Definition 4.1 *Let $F = \{F_1, ..., F_m\}$ be a family of random variables defined on the set S, in which each random variable F_i takes a value f_i in the set of labels L. The family F is called a* **random field**.

Definition 4.2 *F is said to be a* **Markov random field (MRF)** *on S with respect to a neighborhood system N if and only if the following two conditions are satisfied:*

$P(f) > 0 \quad \forall f \in L$ *(positivity)*

$P(f_i|f_{S-(i)}) = P(f_i|f_{N_i})$ *(Markovianity)*

where $S - (i)$ is the set difference, $f_{S-(i)}$ denotes the set of labels at the sites $S - (i)$ and $f_{N_i} = (f_{i'}|i^{'} \in N_i)$ stands for the set of labels at the sites neighboring i.

Definition 4.3 *A set of random variables F is said to be a* **Gibbs random field (GRF)** *on S with respect to N if and only if its configurations obey a Gibbs distribution. A Gibbs distribution takes the following form:*

$P(f) = Z^{-1} \exp^{-U(f)/T}$ *where*

$Z = \sum_{f \in F} \exp^{-U(f)/T}$ *is called the partition function, T, a constant, is the temperature $U(f)$ is the energy function.*

Theorem 4.1 *F is an MRF on S with respect to N if and only if F is a GRF on S with respect to N. This is known as* **Hammersley - Clifford Theorem**.

For the proof of Hammersley - Clifford Theorem, the reader can see [25] *etc.* An image can be represented as a MRF.

For explaining prior and posterior distributions and MAP estimates in the context of image processing, we follow an approach similar to [26]:

Definition 4.4 *Let Π be a probability distribution on a set of images $\mathbf{X}$. As Π depends on individual images x and not on the data y, it is called a* **prior** *distribution.*

Definition 4.5 *Let $P(y|x)$ is the probability to observe y if x is the correct image. This can be considered as a* **likelihood**.

Definition 4.6 *Following* **Bayes' Theorem**, *we can write the conditional probability of $x \in \mathbf{X}$ given y. This is written as: $P(x|y) = \frac{\Pi(x)P(y|x)}{\sum_z \Pi(z)P(z|y)}$ Since $P(.|y)$ is an adjustment of Π to data (after the observation), it is called the* **posterior** *distribution of x given y.*

Definition 4.7 *A mode $x^*(y)$of the posterior distribution $P(.|y)$ is called a* **Maximum Posterior Estimate (MAP)** *of x given y.*

For Gibbsian posterior distributions, MAP estimates are the minimizers of the posterior energy.

Definition 4.8 *A* **stochastic relaxation algorithm** *in this context refers to a nondeterministic, stochastic, iterative algorithm to find the MAP estimates.*

Definition 4.9 Gibbs Sampler *is a stochastic relaxation algorithm, which generates new configurations from a given Gibbs distribution. It is basically a Markov Chain constructed from conditional distributions of the target Gibbs field. In our case, the target Gibbs distribution/field refers to the posterior distribution/field.*

4.5 Hierarchical Bayesian Restoration Framework

In this section, we first describe the statistical model adopted for explaining the pixel intensity distribution of the image within a Bayesian framework and then illustrate the manner in which we model the degradation matrix stochastically. We also prove that in the proposed Bayesian restoration approach the posterior energy remains Gibbsian (in the manner defined by Geman and Geman [3]). Although we describe the model in terms of the entire CT image, however we apply our restoration procedure effectively to the selected localized block.

4.5.1 Statistical Model

Suppose we have an image consisting $m \times n$ pixels. Let $p = m \times n$. Based on the formulation detailed in [3], the pixel intensities in the image can be expressed as

$$g = \Phi(f) + \epsilon \tag{4.5}$$

where g, f and ϵ are $p \times 1$ vectors such that g represents the vector of all observed image intensities, f represents the vector of intensities corresponding to the true image and ϵ is zero-mean random Gaussian noise

$$\epsilon \sim \mathcal{N}(0, \sigma^2 I_p). \tag{4.6}$$

where I_p is the p-th order identity matrix. The function $\Phi(\cdot)$ in equation (4.5) denotes a known degradation (or perturbation) function. Furthermore, we assume the that true pixel intensity f has a known prior distribution. The conditional autoregressive model (CAR) is one of several typical prior distributions used extensively in the domain of image processing. The CAR model also ensures the Markovian property of dependence of the intensity value of any pixel on those of the pixels in its neighborhood [27]. Let τ^2 be the variance of the prior distribution and σ^2 be variance of the data model. Therefore,

$$\begin{aligned} p_{\sigma^2}(g|f) &\propto (\sigma^2)^{-p/2} \exp\left\{-\tfrac{1}{2\sigma^2}||g - \Phi(f)||^2\right\} \\ p(f|\tau^2) &\propto (\tau^2)^{-p/2} \exp\left\{-\tfrac{1}{2\tau^2} f^T (I_p - \gamma N) f\right\} \end{aligned} \tag{4.7}$$

where N is the neighborhood matrix given by $N = [n_{ij}]$ as $n_{ii} = 0 \; \forall \; i$ and

$$n_{ij} = \begin{cases} 1 & \text{if} \quad i \text{ and } j \text{ are neighbors} \\ 0 & \quad \text{otherwise} \end{cases} \tag{4.8}$$

The value of γ is appropriately chosen to avoid singularity of the matrix $(I_p - \gamma N)$. Also the prior distributions on σ^2 and τ^2 are chosen as

$$\begin{aligned} p(\sigma^2) &\propto (\sigma^2)^{-(\nu+1)} \, e^{-\beta/\sigma^2} \\ p(\tau^2) &\propto (\tau^2)^{-(\kappa+1)} \, e^{-\delta/\tau^2}. \end{aligned} \tag{4.9}$$

In other words, $\sigma^2 \sim$ inverse-gamma (ν, β) and $\tau^2 \sim$ inverse-gamma (κ, δ). Under this formulation, the posterior distribution of f given the observed data g can be shown to be Gibbsian on account of conjugacy under linear degradation. Before describing the proposed MRF-MAP scheme in detail, it is important to formulate a precise definition of the term *known degradation* in the present context. In image processing, generally, the term *known degradation* commonly refers to a mathematically known degradation (or blurring) function which is applied to the *entire* true image and which in conjunction along with the (typically additive) noise yields the observed data.

For fracture detection, we assume that the image of the fractured mandible is a degraded version of some true (possibly hypothetical) intact mandible. Consequently, the degradation function needs to be formulated in a manner such that if it is applied to the entire true image, i.e., the CT image of the intact mandible, the resulting image should display a hairline fracture at the desired site while retaining the pixel intensity values of the true image elsewhere. A minor/hairline fracture denotes a loss of bone mass and hence can be modeled as a decrease in the Hounsfield unit (image intensity) at the fracture site. Thus, from equation (4.5), a simple formulation of the degradation function could be

$$g = Af + \epsilon \tag{4.10}$$

where A is the degradation matrix of order $p \times p$ consisting of non-zero elements only along the diagonal. For the i-th pixel,

$$g_i = a_i f_i + \epsilon_i \tag{4.11}$$

where

$$a_i = \begin{cases} \alpha_i & \text{if } \; i \text{ is a fracture site} \\ \\ 1 & \text{otherwise} \end{cases} \tag{4.12}$$

for some $\alpha_i \in (0,1)$. The prior distribution of α_i is assumed to be Gaussian:

$$\alpha_i \sim \mathcal{N}(\alpha_{i0}, \eta^2). \tag{4.13}$$

The choice of parameters α_{i0} and η is made in such a way that the support of the distribution becomes effectively $(0,1)$. Later in this section, we provide details on the choice of α_{i0}.

Lemma 4.1 *Under the model characterized by equations (4.5)-(4.13), for each fixed value of g, the posterior probability $p(f|g)$ is a Gibbs distribution with an associated energy function given by:*

$$U(f|g) = \frac{1}{2\sigma^2}||g - Af||^2 + \frac{1}{2\tau^2} f^T (I_p - \gamma N) f$$

For a detailed proof of the above lemma, the interested reader is referred to [3]. As a special case of the Lemma 1, we formulate the following lemma. Before we formulate the lemma, we introduce the parameter f_{i-} to denote the neighborhood of f_i.

Lemma 4.2 *Based on the MRF formulation in equation (4.6) and equations (4.10) – (4.12), if we assume $E(f_i|f_{i-}) = \mu(f_{i-})$ then the posterior distribution of f_i given g_i can be shown to be (see [28] for details)*

$$f_i|g_i, f_{i-} \sim \mathcal{N}\left(\frac{\frac{a_i g_i}{\sigma^2} + \frac{\mu(f_{i-})}{\tau^2}}{\frac{a_i^2}{\sigma^2} + \frac{1}{\tau^2}}, \frac{1}{\frac{a_i^2}{\sigma^2} + \frac{1}{\tau^2}} \right).$$

Proof The posterior distribution of $f_i|g_i, f_{i-}$ can be expressed as

$$\begin{aligned} p(f_i|g_i, f_{i-}) &\propto \exp\left\{ -\frac{1}{2\sigma^2}(g_i - a_i f_i)^2 - \frac{1}{2\tau^2}(f_i - \mu(f_{i-}))^2 \right\} \\ &\propto \exp\left[-\tfrac{1}{2}\left\{ \left(\frac{a_i^2}{\sigma^2} + \frac{1}{\tau^2} \right) f_i^2 - 2 f_i \left(\frac{a_i g_i}{\sigma^2} + \frac{\mu(f_{i-})}{\tau^2} \right) \right\} \right] \\ &\propto \exp\left\{ -\frac{\frac{a_i^2}{\sigma^2} + \frac{1}{\tau^2}}{2} \left(f_i - \frac{\frac{a_i g_i}{\sigma^2} + \frac{\mu(f_{i-})}{\tau^2}}{\frac{a_i^2}{\sigma^2} + \frac{1}{\tau^2}} \right)^2 \right\} \end{aligned}$$

In lemma 4.2 above it should be noted that $E(f_i|g_i)$ can be seen to be a weighted average of the data and mean of the prior distribution with the weights being functions of reciprocals of σ^2 and τ^2. In other words, the posterior mean is a weighted average of data mean and prior mean where the weights are proportional to their respective precisions.

4.5.2 Modeling of the Stochastic Degradation Matrix

A critical issue in the proposed MRF-MAP formulation described above is an appropriate choice for the values of α_i. A necessary prerequisite for choosing an appropriate value of α_i is to acquire some *a priori* knowledge on the shape of the mandible within the selected pixel blocks in each CT slice. The inner contour and outer contour of the portion of the mandible within the selected set of pixel blocks can each be essentially approximated by a quadratic polynomial with a distinct set of coefficients. A quadratic polynomial has the general form:

$$y = c_0 + c_1 x + c_2 x^2. \tag{4.14}$$

To estimate the coefficients c_0, c_1 and c_2 in equation (4.14), we need a set of three points, say, $(x_1, y_1), (x_2, y_2), (x_3, y_3)$ on the inner contour and likewise on the outer contour of the portion of the mandible in the selected set of pixel blocks in each image slice in the CT image stack. The need to obtain so many data points i.e., these six data points per contour (inner or outer) per CT image slice, can be justified as follows:

1. The inner and outer contours of the mandible, appearing in a particular CT image slice, cannot be represented mathematically by a single quadratic polynomial with the appropriate translational parameters along the x and y axes. This is because the curvatures of the inner contour and the outer contour of the mandible are observed to be quite different.

2. Since the spatial resolution of the image stack is coarser along the z axis (axial direction) compared to the x and y axes, an inner or outer contour of the mandible in two

different slices cannot be mathematically approximated by a single quadratic polynomial. This is once again due to difference in curvatures of an inner (or outer) contour in two consecutive CT image slices.

Here we once again re-emphasize a major advantage of the proposed localization phase. Fitting a second degree polynomial to a small portion of the bone surface is more appropriate than to the entire mandible. Although the whole mandible can be roughly viewed as a parabolic shape but it is not exactly a parabola. A small portion of the mandible, on the other hand, can be more accurately represented by a parabola (which is a second degree polynomial). Thus, it is more appropriate to use the second-order polynomial shape approximation within a small pixel lock over an attempt to derive a complex shape model for the entire mandible.

In the current implementation, user interaction is required (via computer mouse clicks) to generate all the required data points. Note that a typical set of three data points can be located anywhere along the inner or outer contour of the portion of the mandible within the chosen set of pixel blocks. Thus, the coefficients of the fitted quadratic polynomial are not particularly sensitive to the choice of the clicked points to the extent that these points lie on the (inner or outer) contour whose equation is being estimated. Once the quadratic polynomial for a contour is determined, a set of points satisfying the polynomial (i.e., set of points along the fitted contour) is generated. Typically, most of the points within the set have high intensity values, since they correspond to bone pixels, whereas only a few have low intensity values since they correspond to pixels at a potential fracture site. For potential fracture pixels at a site i, on a given contour, the value of α can be ideally assumed to be given by:

$$\alpha_i = g_i / \max_i(g_i) \tag{4.15}$$

where $\max_i(g_i)$ represents the maximum of all the observed pixel intensity values along the contour under consideration. Therefore, it is reasonable to assume the mean of $\alpha_i (= \alpha_{i0})$ to be $g_i / \max_i(g_i)$.

Lemma 4.3 *Under the model characterized by equations (4.7), (4.9) and (4.13), it can be shown that the full conditional distribution of α_i is given by*

$$\alpha_i|g_i, f_i \sim \mathcal{N}\left(\frac{\frac{g_i f_i}{\sigma^2} + \frac{\alpha_{i0}}{\eta^2}}{\frac{f_i^2}{\sigma^2} + \frac{1}{\eta^2}}, \frac{1}{\frac{f_i^2}{\sigma^2} + \frac{1}{\eta^2}}\right).$$

The proof of Lemma 4.3 is very similar to the proof of Lemma 4.2 given earlier.

Lemma 4.4 *Under the model characterized by equations (4.7), (4.9) and (4.13), the full conditional distribution of σ^2 is given by*

$$\sigma^2|g, f, \alpha \sim \textit{ Inverse-gamma } \left(\frac{p}{2} + \nu, \frac{S + 2\beta}{2}\right).$$

where $S = ||g - Af||^2$ and α is a vector with the elements being the collection of all α_is.

Proof: Note that

$$p(\sigma^2, f, g) \propto p_{\sigma^2}(g|f)p(f|\tau^2)p(\sigma^2)$$

From equations (4.7), (4.9) and (4.13), we can write:

$$p(\sigma^2|f_i, g_i) \quad \propto \quad \left(\sigma^2\right)^{-\frac{p}{2} - (\nu+1)} \exp\left\{-\frac{S + 2\beta}{2\sigma^2}\right\}$$

Hence the Lemma.

Lemma 4.5 *Under the model characterized by equations (4.7), (4.9) and (4.13), the full conditional distribution of τ^2 is given by*

$$\tau^2|f, g \sim \textit{ Inverse-gamma } \left(\frac{p}{2} + \kappa, \frac{f^T(I_p - \gamma N)f + 2\delta}{2}\right).$$

The proof of the above lemma is similar to the proof of Lemma 4.4.

It can be noted that all conditional posterior distributions in question have closed-form expressions that are known. Under this situation, we can iteratively draw samples from the posterior distribution using Gibbs sampling. The Gibbs sampling procedure ensures convergence to the MAP estimate of the true image after a sufficient number of iterations [3].

4.6 Experimental Results and Analysis

In this section, we will describe experimental results on fracture detection and target mandibular reconstruction using the proposed two-phase MRF-MAP-based scheme within a hierarchical Bayesian setup. The experiments were performed on 7 different real patient CT scans with different resolutions (pixels/mm) and fracture locations. The fractures were observed to appear typically in 3-6 2D slices in each CT image sequence. Each 2D CT image slice is of size 512×512 pixels with a grayscale resolution of 8 bits per pixel.

4.6.1 Results on Fracture Localization

Dataset	Block Size	Potential Blocks	Selected Blocks	Correlation
1	$64 \times 64 \times 3$	8	2	$0.022, 0.038$
	$32 \times 32 \times 3$	13	4	$0.007, 0.068, 0.109, 0.153$
2	$32 \times 32 \times 3$	15	2	$0.012, 0.036$
3	$32 \times 32 \times 3$	11	2	$0.03, 0.16$
	$32 \times 32 \times 3$	11	3	$0.03, 0.16, 0.23$
4	$32 \times 32 \times 4$	8	4	$0.002, 0.028, 0.087, 0.144$
5	$32 \times 32 \times 3$	9	2	$0.029, 0.101$

Table 4.1: Fracture localization

Dataset	Emphysema	Tissue Swell. (pix. dist.)	Bone pix.	Frac. Half
1	$Left$	–	–	$Left$
2	–	$left : 65, right : 54$	–	$Left$
3	$Left$	–	–	$Left$
4	–	$left : 36, right : 79$	–	$Right$
5	–	$left : 44, right : 76$	–	$Right$
6	–	–	$left : 5996; right : 5097$	$Right$
7	–	$left : 60, right : 64$	–	$Right$

Table 4.2: Detection of the fractured half

In the first stage of the proposed two-phase scheme, we localized the fracture by determining the approximate region and the image half, in which it appears. The pixel block width and height (which is a power of 2 in the current implementation) is sought as an input

from the user via a graphical user interface (GUI). The block thickness is deemed to be the number of 2D slices, in which a broken jaw appears in a given CT sequence. For the CT image sequences used in the current experiments, the pixel block width and height vary between 64×64 and 32×32. Similarly the thickness for the present set of data varies between 3 and 6. However, our scheme is fairly robust to the chosen block dimensions. For example, from figure (4.1) and table (4.1), it is evident that the localization works correctly for *dataset* 1 with two different pixel block dimensions given by $64 \times 64 \times 3$ and $32 \times 32 \times 3$. With pixel block dimensions of $64 \times 64 \times 3$, there were altogether 32 pairs of pixel blocks to be examined. For this particular dataset i.e. *dataset* 1, after the two heuristics based on mandible size and bone pixel intensity were applied, only 8 out of 32 blocks were retained. These were then arranged in order of increasing value of the correlation coefficient. Finally, 2 out of these 8 pixel blocks were chosen as potential hairline fracture sites. For the same dataset, with pixel block dimensions of $32 \times 32 \times 3$, the first 13 out of a possible 128 blocks were retained using the aforementioned two heuristics and eventually 3 out of 13 blocks were chosen as potential hairline/minor fracture sites based on the correlation coefficient values. Table (4.1) shows details of our experiments with five different datasets and two different block sizes. It shows the number of selected blocks based on correlation values in each case and typical values of correlation coefficient for potential fracture-containing blocks. Table (4.1) along with figure (4.1) clearly illustrates that our scheme is not strictly sensitive to (a) the chosen pixel block size and (b) the number of pixel blocks selected as sites of minor/hairline fractures. However, we would like to add the following observations (which hold in most of the cases)

1. For a mandible of larger size, the size of the pixel block may be chosen to be larger e.g. a 64×64 block size would work better compared to a 32×32 block size for a larger mandible.

2. If number of mandible-containing blocks (k) is smaller, then it is better to be conservative in choosing number of selected blocks (q) as sites of potential fractures e.g. if k turns out to be 2, then it is preferable to choose q as 2, rather than 1 (a case not shown in table (4.1)).

Next, we discuss the determination of the CT image half containing the potential fracture. Out of the seven datasets we experimented with, we detected the presence of emphysema in two cases (see table (4.2)). The detection of *emphysema* is also marked by the presence of white crosses in figure (4.1). Note that we have just marked one particular pixel site to denote the occurrence of *emphysema* in each of the 2D slices, where as potentially there is quite a few such emphysema pixels. Obviously, the image half in which emphysema is detected is designated as the one containing fracture site. table (4.2) demonstrates the detection of *swelling of the soft tissue* for four other datasets. For a given dataset, the average pixel distance of the outer soft tissue boundary from the center of the localized block is computed for both the left and the right image half. The image half for which the average pixel distance is higher, indicates the presence of *soft tissue swelling* and hence the fracture site. The difference in the distance can be quite high such as 30- 40 pixels in case of major swelling (as indicated for *datasets* 4 and 5 in table (4.2)) or could be quite small like under 10 pixels in case of minor swelling (as indicated for *datasets* 1 and 7 in table (4.2)). The major and minor swellings can be found in figures (4.4) and (4.5) and figures (4.1) and (4.7) respectively. In one single case (*dataset* 6), we used the count of the number of bone pixels (i.e. pixels with a high intensity value) within the localized blocks (in both the halves) for determining the fracture-containing image half. Logically, the fracture half (within the localized area) should contain fewer bone pixels compared to its non-fracture-containing symmetric counterpart. As there was no *emphysema* and the *soft tissue swelling* is negligible, the above heuristic was employed to determine the fracture-containing image half for *dataset* 6 (see figure (4.6) and table (4.2)). The first and second row in each of the figures (4.1, ..., 4.7) respectively represent a CT image sequence that depicts a mandible with a minor/hairline fracture and the localization of the fracture. Additionally, in figure (4.1), the fourth row portrays fracture localization with a different set of pixel block dimensions and with a different number of potential fracture containing blocks (selected, based on correlation values). For all the seven datasets, the localized fractures are highlighted by the surrounding black boxes at the fracture sites.

4.6.2 Precise fracture detection using MRF-MAP scheme

Coeffs. of Quad. Poly.	Slice 1		Slice 2		Slice 3	
$(c_0 + c_1x + c_2x^2)$	Outer	Inner	Outer	Inner	Outer	Inner
c_0	-11344	6808	8798	5228.7	-177200	-107.19
c_1	162	75.7	-113.2	67.8	2380	5.79
c_2	-1	2	4	2	-10	-0.02

Table 4.3: Coeffs. of the Quad. Poly. for outer and inner contours over various slices for the dataset 1

In this subsection, we will first discuss in detail the three coefficients, required to fit a second order polynomial to a mandible contour in a 2D slice. From table (4.3), it is quite clear that for a given slice, the outer and inner contours of a jaw cannot be approximated by two (approximately) parallel quadratic polynomials as all of the three coefficients are widely different. Thus, the user needs to provide six data points per slice (3 data points for the inner contour and 3 data points for the outer contour). Table (4.3) also shows that an outer(inner) contour cannot be approximated over all the slices using the same quadratic polynomial. Thus, the necessity of six points per 2D slice (that contains a fracture) is numerically justified. These points are provided by the user via interactive mouse clicks. It is important to note in this context that the proposed scheme is not sensitive to any specific pattern of mouse clicks. As long as the user clicks on three points on the outer contour and three points on the inner contour in each of the relevant 2D slices, the polynomial fitting procedure and hence subsequent fracture detection works well. This is clearly illustrated in figure (4.8), where the contour extraction for two different datasets are shown. The centers of the black crosses mark the locations of the mouse clicks. In some cases, even the portion of the mandible contour within the localized area cannot be approximated using a quadratic polynomial. In such cases, one needs to further restrict the span of mouse clicks within the localized region. Another practical constraint for reducing the spatial extent of the mouse clicks could be excessive intensity inhomogeneity in the CT images. We have used domain knowledge about possible fracture point intensity values to estimate the degradation matrix. So, using

equation (4.15), we assign a value of 1 to a_i if α_i is in the range [0.85, 1]; we assign α_i to be the mean of a_i otherwise.

For the MRF-MAP formulation, we chose a first order neighborhood. As far as the statistical parameters are concerned, we chose the shape and scale of the inverse gamma distribution for τ^2 to be 3.0 and 1.0 and for σ^2 to be 3.0 and 0.5. We experimented with both 100 and 1000 as the number of iterations for the possible convergence of the Gibbs sampling procedure (i.e., for the posterior distribution to attain its maximum value) for two datasets. Since, we did not find any notable visual difference in the reconstructed output, we simply decided to use 100 iterations for the remaining datasets, thus reducing the execution time. In fact the completion of each phase in the proposed two-phase scheme was observed to take about 2-3 minutes on a 1.73 GHz Intel© Pentium©-M processor. It is relevant to discuss here why we opted for a partial 3D scheme instead of a pure 3D scheme for the purpose of fracture detection. The localization procedure is essentially a 3D scheme as the correlation is computed over a single 3D pixel block instead of multiple 2D blocks in individual 2D slices. The estimation of the degradation matrix calls for prior polynomial fitting to the contours of the mandible. It is visually intuitive to fit a second-order polynomial to portions of these contours over the localized block in individual 2D slices. Thus, as mentioned earlier, we can avoid the use of complicated shape models for an entire 3D mandible. Furthermore, since the number of slices in which a fracture appears in a stack is often few (typically 3 to 6), a complete 3D scheme would not have resulted in a significant performance improvement in terms of overall execution time. The third row in each of the figures (4.2),..., (4.7) and the third as well as the fifth row in the figure (4.1) show the results of precise fracture detection and visualization using the proposed MRF-MAP scheme. Note that whereas the original intensity values at the fracture pixel sites are low (due to bone loss), the reconstructed (restored) intensity values at these sites are high, (corresponding to the bone pixel intensities) on account of MAP estimation via repetitive Gibbs sampling. The pixels exhibiting large intensity differences (between the reconstructed and the fractured mandible) are highlighted (using the color black) for the purpose of visualization. The detection of the hairline fractures was validated by experienced surgeons. In this context, we would like to briefly

discuss about controlling the threshold (indicating the difference in intensity between the input data and the reconstructed data) for fracture visualization. If the user selects a low threshold value, the final fracture appearance will be quite restricted. On the contrary, if the user selects a higher value for this threshold, the fracture at the proper locations will be displayed more prominently but at the cost of some spurious appearances (due to spatial spread). This fact is well illustrated by figure (4.6) where the threshold value increases from the third to the fifth row. This procedure for adjusting the threshold can be viewed as tuning a practical knob for controlling the visualization of the fractures. We end this section with a brief discussion on target pattern generation. Figures (4.9), (4.10) and (4.11) depict the generated target patterns for three different datasets. The first row in each of these figures depicts the broken jaw, where as the second row illustrates the *in silico* reconstructed jaw, generated using the proposed MRF-MAP-based approach. It is quite evident that the reconstructions in figures (4.9) and (4.10) exhibit relatively smooth mandible contours which, in turn, indicate that natural bone healing could be opted for in such cases. However, the reconstructed jaw in figure (4.11) exhibits a relatively rugged mandible contour which indicates that surgical intervention may be a more appropriate choice in this case.

4.7 Conclusion and Future Work

In this chapter, we presented a novel two-phase scheme for simultaneous hairline fracture detection and target pattern generation for fractured human mandibles. The fracture detection scheme is robust to the presence of noise and intensity inhomogeneity, present in the CT images. The reconstructed jaw can be treated as a target pattern which can assist a surgeon in determining whether manual surgical intervention is necessary or whether natural bone healing is adequate. In the first phase of the proposed two-phase approach, the hairline/minor fractures are localized within the pixel blocks of a given size by analyzing all the image slices in the CT image stack. The CT image analysis exploits the (approximate) bilateral symmetry of the human mandible and uses the statistical correlation coefficient as a measure of intensity mismatch. The CT image half, in which a fracture appears is

determined by exploiting domain knowledge that includes the presence of *emphysema*, *soft tissue swelling* and occurrence of a fewer bone pixels in localized fracture sites. In each of the aforementioned pixel blocks, an MRF-MAP-based approach for hairline/minor fracture detection is employed. The MRF-MAP-based approach surpasses existing conventional techniques based on corner detection or discontinuity detection in the image intensity surface. The hairline fracture detection scheme has obvious diagnostic significance. Since the implicit reconstruction procedure embedded within the proposed MRF-MAP based technique is designed to mimic the natural bone healing process in the absence of any surgical intervention, the proposed scheme has an important prognostic significance as well. In addition to the aforementioned clinical significance, the problem of hairline fracture detection also has certain noteworthy aspects of theoretical interest from the perspective of computer vision and pattern recognition research. This is primarily because we are faced with the challenging task of modeling a spatially localized degradation resulting from a mathematically unknown degradation function. Thus, we first computed the degradation matrix from the input data by fitting quadratic polynomial functions to the inner and outer contours of the mandible. This was followed by the application of the Gibbs sampling procedure for the MAP probability estimation. In the current implementation, the degradation matrix A is modeled as a stochastic entity, by imposing a normal distribution on the α values. Additionally, we used the inverse-gamma distribution for both τ^2 (variance of the prior distribution) and σ^2 (variance of the data model) in order to conform to the hierarchical Bayesian estimation paradigm.

Our future plan is to incorporate a higher degree of automation within the existing scheme. The current scheme for quadratic polynomial approximation of the contours of the mandible calls for user interaction via mouse clicks; which could be automated in order to reduce the burden on the user. Another future direction entails automatic identification of the set of 2D CT image slices containing the fractured mandible from a larger set of CT images. Note that a typical CT image sequence is an aggregation of 2D image slices where only some of the image slices contain the fractured mandible. We also intend to explore the utility of the present MRF-MAP approach as a smoothing tool. Thus, we can potentially

use the proposed MRF-MAP scheme as a smoothing tool on instances of well-displaced fractures that have been coarsely registered [29]. Subsequently, we can generate a better 3D model of the reconstructed mandible resulting in a more accurate analysis of biomechanical stability. From the statistical perspective, we plan to investigate the effects of (a) a higher-order neighborhood (e.g. second order) for the MRF or a different model for the MRF-MAP paradigm (e.g. the SAR model) [24] and (b) an objective assumption on the prior distribution of the nuisance parameters which would make the problem computationally more challenging [28].

4.8 References

[1] B.O. Ogundare, A. Bonnick and N. Bayley, "Pattern of Mandibular Fractures in an Urban Major Trauma Center", *J. of Oral and Maxillofac. Surg.*, vol. 61, no. 6, pp. 713-718, June 2003.

[2] C. J. Harris and M. Stephens, "A combined corner and edge detector", in *Proc. 4th Alvey Vision Conference*, Manchester, UK, pp. 147-151, 1988.

[3] S. Geman and D. Geman, "Stochastic Relaxation, Gibbs Distributions, and the Bayesian Restoration of Images", *IEEE Trans. Pattern Anal. Mach. Intell.*, vol. 6, no. 6, pp. 721 - 741, June 1984.

[4] J. Besag, "On the Statistical Analysis of Dirty Pictures", *J. Roy. Statist. Soc. B*, vol. 48, no. 3, pp. 259-302, 1986.

[5] S.J. Lee, A. Rangarajan and G. Gindi, "Bayesian Image Reconstruction in SPECT Using Higher Order Mechanical Models as Priors", *IEEE Trans. Med. Imag.*, vol. 14, no. 4, pp. 669 -680, Dec. 1995.

[6] S. M. Choi, J. E. Lee, J. Kim and M. H. Kim, "Volumetric Object Reconstruction Using the 3-D MRF Model-Based Segmentation", *IEEE Trans. Med. Imag.*, vol. 16, no. 6, pp. 887-892, Dec. 1997.

[7] A.K. Chan and L. Zheng, "An artificial intelligent algorithm for tumor detection in screening mammogram", *IEEE Trans. Med. Imag.*, vol. 20, no. 7, pp. 559 - 567, July 2001.

[8] E. Salli, H. J. Aronen, S. Savolainen, A. Korvenoja and A. Visa, "Contextual Clustering for Analysis of Functional MRI Data", *IEEE Trans. Med. Imag.*, vol. 20, no. 5, pp. 403-414, May 2001.

[9] T. Chen and D.N. Metaxas, "Markov Random Field Models", in *Insight into Images*, T. S. Yoo Ed., A.K. Peters, Wellesey, MA, 2004.

[10] F.J.P. Richard, "A comparative study of Markovian and variational image-matching techniques in application to mammograms", *Pattern Recognit. Lett.*, vol. 26, pp. 1819 - 1829, 2005.

[11] C. Popa and R. Zdunek, "Penalized Least-Squares Image Reconstruction For Borehole Tomography", in *Proc. of Algorithmy*, Podbanske, Slovakia pp. 260-269, March 2005.

[12] M. Martin-Fernandez, C. Alberola-Lopez, "An approach for contour detection of human kidneys from ultrasound images using Markov random fields and active contours", *Med. Image Anal.*, vol. 9, pp. 1 - 23, 2005.

[13] A. Raj, G. Singh and R. Zabih, "MRFs for MRIs: Bayesian Reconstruction of MR Images via Graph Cuts", in *Proc. of CVPR*, New York, NY, pp. 1061 - 1068, June 2006.

[14] T. Ozanian and R. Phillips, "Image Analysis for Computer-Assisted Surgery of Hip Fractures", *Med. Image Anal.*, vol. 4, no. 2, pp. 137 - 159, June 2000.

[15] D. W. H. Yap, Y. Chen, W. K. Leow, T. S. Howe, and M. A. Png, "Detecting Femur Fractures by Texture Analysis of Trabeculae", in *Proc. of ICPR*, Cambridge, UK, pp. 730-733, August 2004.

[16] M. Syiam, M.A. El-Aziem and M. El-Mensshawy, "Adgen: Adaptive Interface Agent for X-Ray Fracture Detection", *Internat. J. of Comput. and Inform. Sci.*, vol. 2, no. 3, pp. 143 - 148, 2004.

[17] "M. Donnelley and G. Knowles, Automated Bone Fracture Detection", in *Proc. of SPIE Medical Imaging*, San Diego, CA, pp. 955 - 966, February 2005.

[18] V. Lum, W. Leow, Y. Chen, T. Howe and M. Png, "Combining classifiers for bone fracture detection in X-ray images", in *Proc. of IEEE ICIP*, Genoa, Italy, pp. 1149 - 1152, September 2005.

[19] Y Jia and Y Jiang, "Active Contour Model with Shape Constraints for Bone Fracture Detection", in *Proc. of IEEE CGIV*, Sydney, Australia, pp. 90-95, July 2006.

[20] A.S. Chowdhury, S.M. Bhandarkar, G. Datta and J.C. Yu, "Automated Detection of Stable Fracture Points In Computed Tomography Image Sequences", in *Proc. of IEEE ISBI*, Arlington, VA, pp. 1320 - 1323, April 2006.

[21] S. Prima, S. Ourselin, and N. Ayache, "Computation of the Mid-Sagittal Plane in 3D Brain Images", *IEEE Trans. Med. Imag.*, vol. 21, no. 2, pp. 122-138, Feb. 2002.

[22] P. V. Giannoudis and H. Dinopoulos, "Current concepts of the inflammatory response after major trauma: an update", *Injury*, vol. 36, no. 1, pp. 229-230, Jan. 2005.

[23] Y. Vodovotz *et al.*, "In silico models of acute inflammation in animals", *Shock*, vol. 26, no. 3, pp. 235-44, Sep. 2006.

[24] S. Z. Li, *Markov random field modeling in computer vision*, Springer-Verlag London, UK, 1995.

[25] J. Besag, "Spatial interaction and the statistical analysis of lattice systems" (with discussions). *J. Roy. Stat. Soc., Ser. B*, vol. 36, pp. 192-236, 1974.

[26] G. Winkler, *Image Analysis, Random Fields and Markov Chain Monte Carlo Methods*, Springer-Verlag, Berlin Heidelberg, Germany, 2003.

[27] R. Molina, "On the Hierarchical Bayesian Approach to Image Restoration: Applications to Astronomical Images", *IEEE Trans. Pattern Anal. Mach. Intell.*, vol. 16, no. 11, pp. 1122-1128, Nov. 1994.

[28] A. Gelman, J.B. Carlin, H.S. Stern and D.B. Rubin, *Bayesian Data Analysis*, Chapman & Hall-CRC, NY, 2004.

[29] S.M. Bhandarkar, A.S. Chowdhury, Yarong Tang, Jack Yu and E.W.Tollner, "Surface Matching Algorithms for Computer Aided Reconstructive Plastic Surgery", in *Proc. of IEEE ISBI*, Arlington, VA, pp. 740 - 743, April 2004.

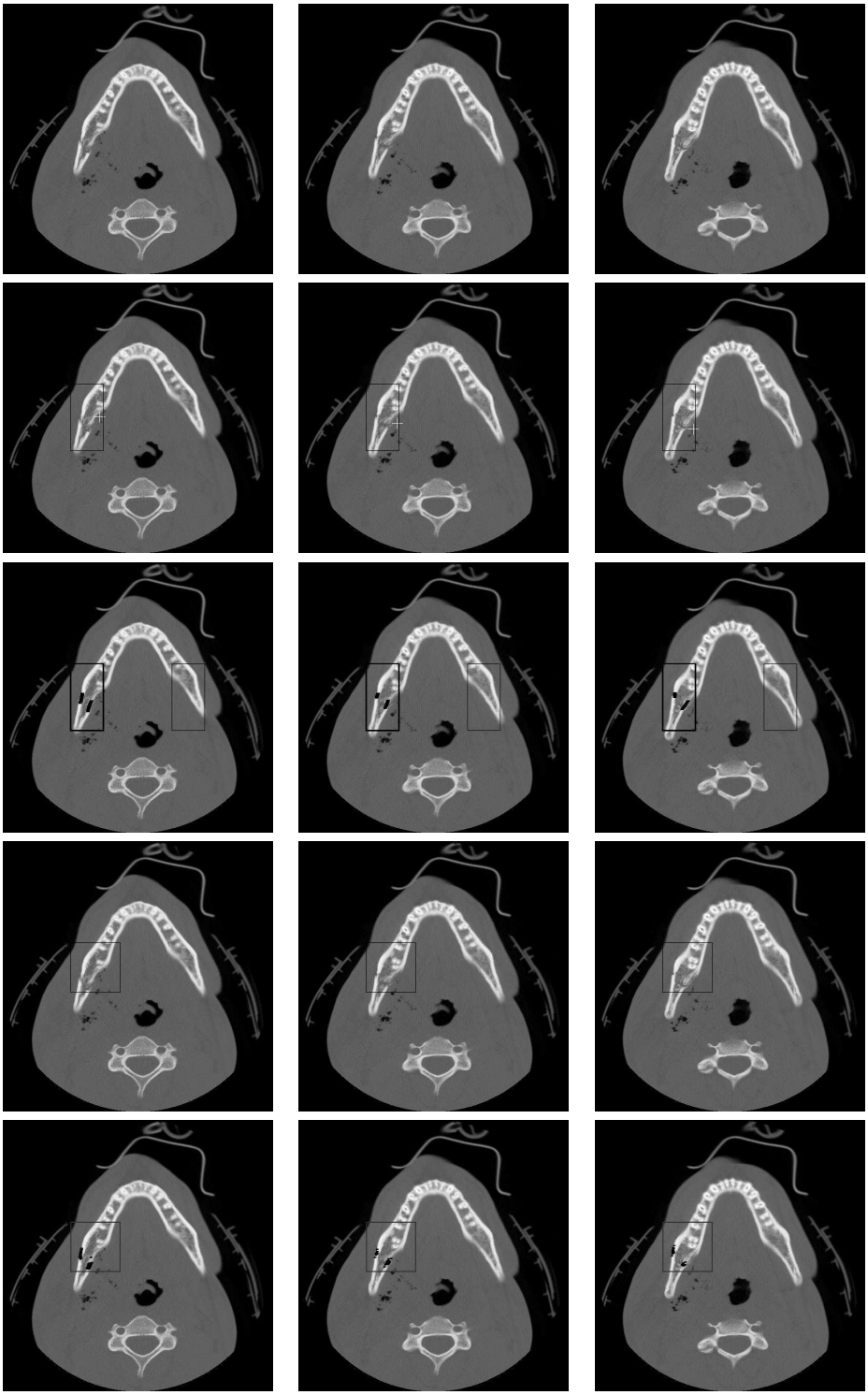

Figure 4.1: Fracture detection for dataset 1 (the topmost row shows the input sequence, the second and third row from the top shows fracture localization and precise detection with a 'block size' of $64 \times 64 \times 3$ and 2 selected blocks (in terms of correlation); the fourth and fifth row respectively show the same with a 'block size' of $32 \times 32 \times 3$ and 4 selected blocks (in terms of correlation); additionally centers of white crosses in the second row mark the detection of *emphysema*)

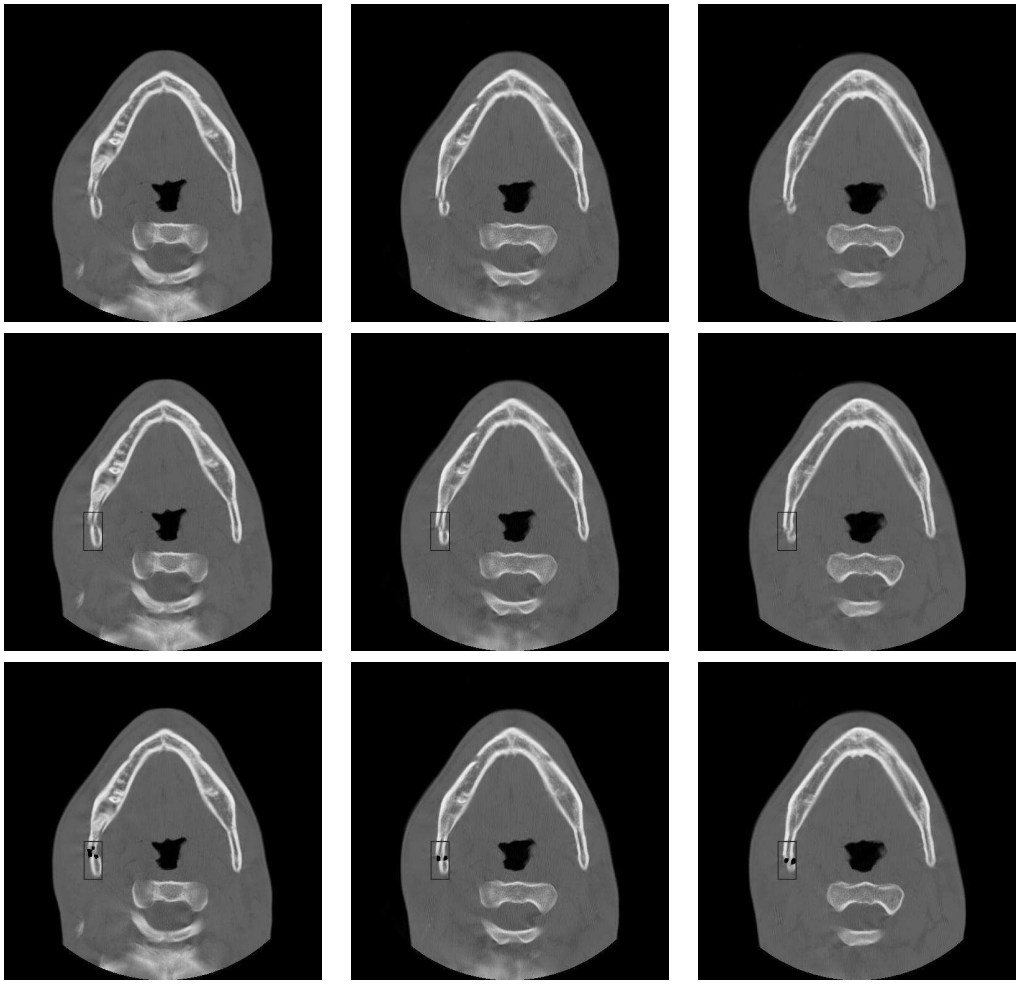

Figure 4.2: Fracture detection for dataset 2 (the top tow shows the input sequence, the middle row shows the localization and the bottom row shows the precise detection of the fracture)

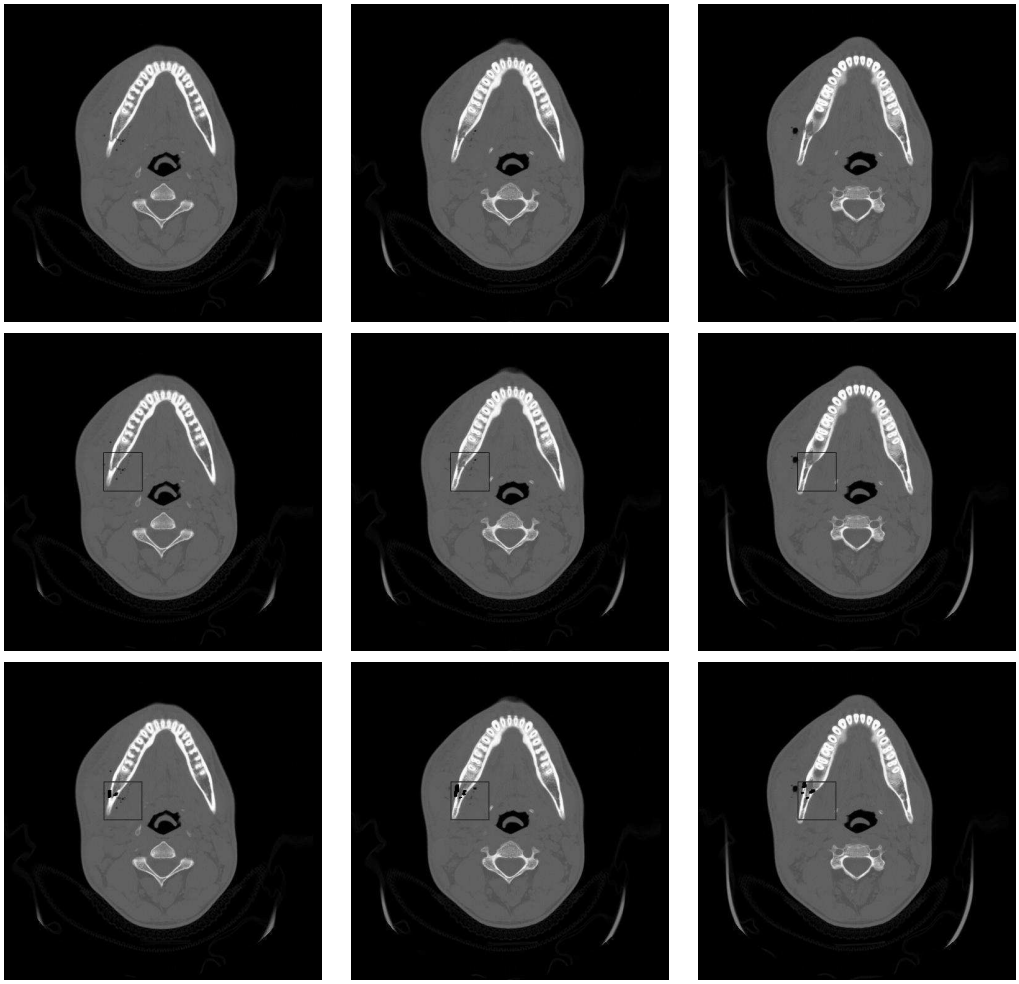

Figure 4.3: Fracture detection for dataset 3 (the top tow shows the input sequence, the middle row shows the localization and the bottom row shows the precise detection of the fracture)

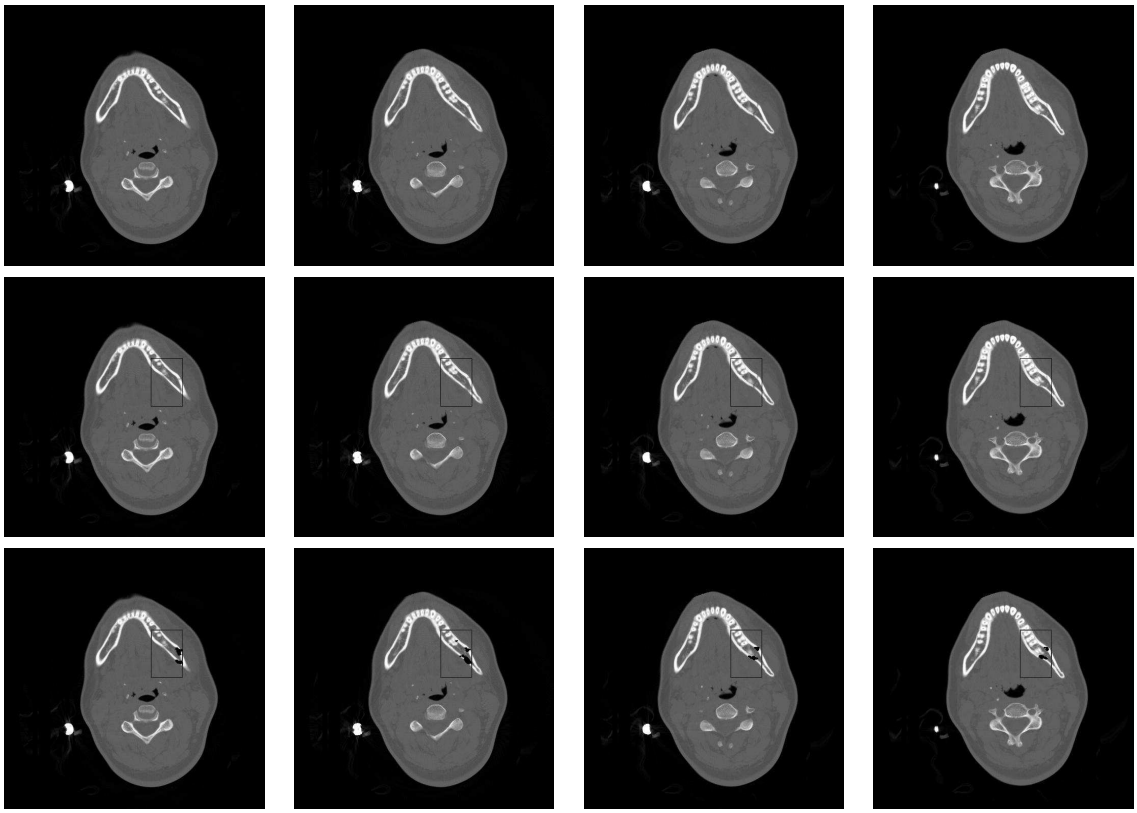

Figure 4.4: Fracture detection for dataset 4 (the top tow shows the input sequence, the middle row shows the localization and the bottom row shows the precise detection of the fracture)

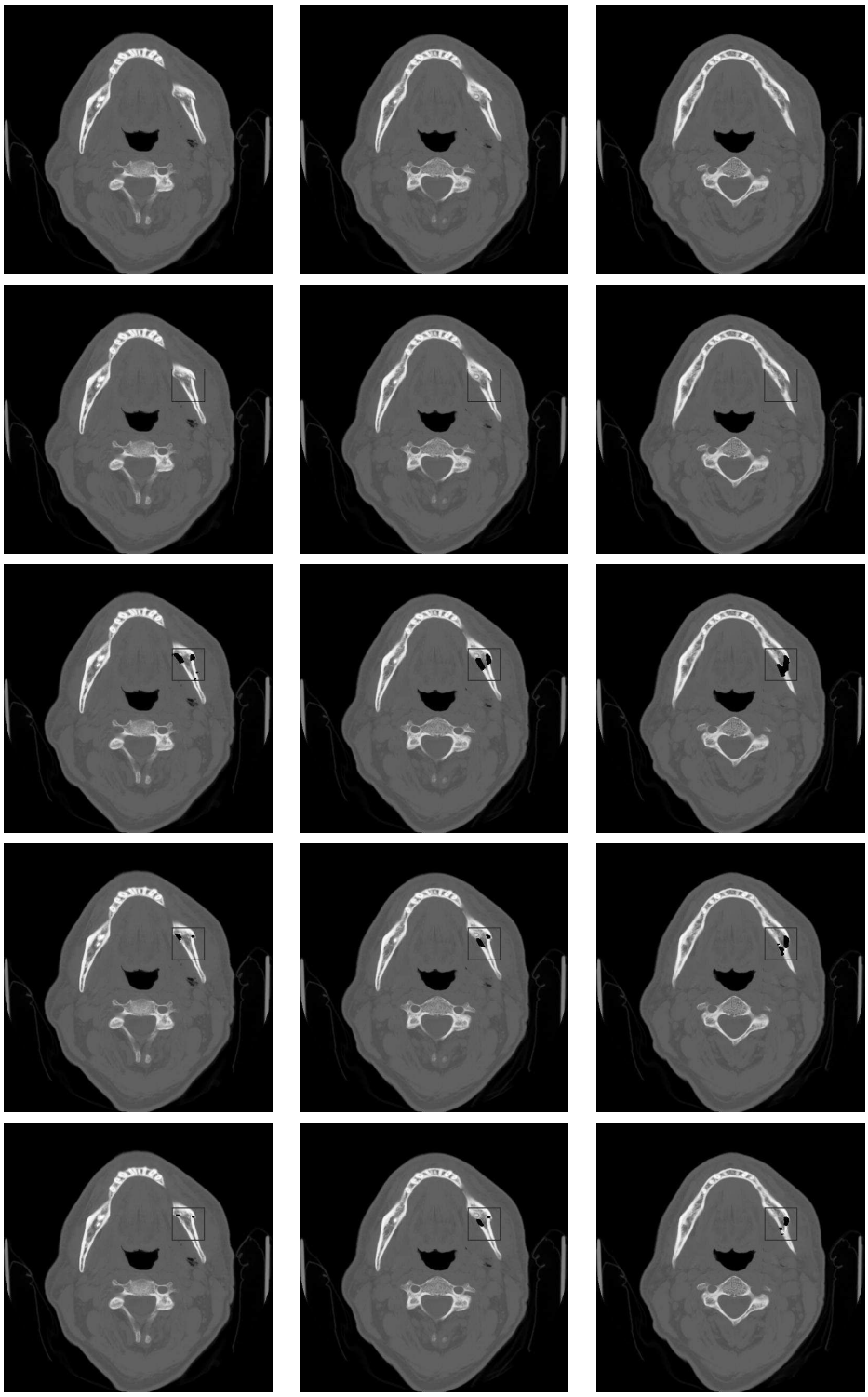

Figure 4.5: Fracture detection for dataset 5 (the topmost tow shows the input sequence, the second row from the top shows the localization of the fracture, the third, fourth and fifth rows show the precise detection and visualization of the fracture with successive increase in the threshold value; the threshold value indicates a difference in intensity between the input and the reconstructed data)

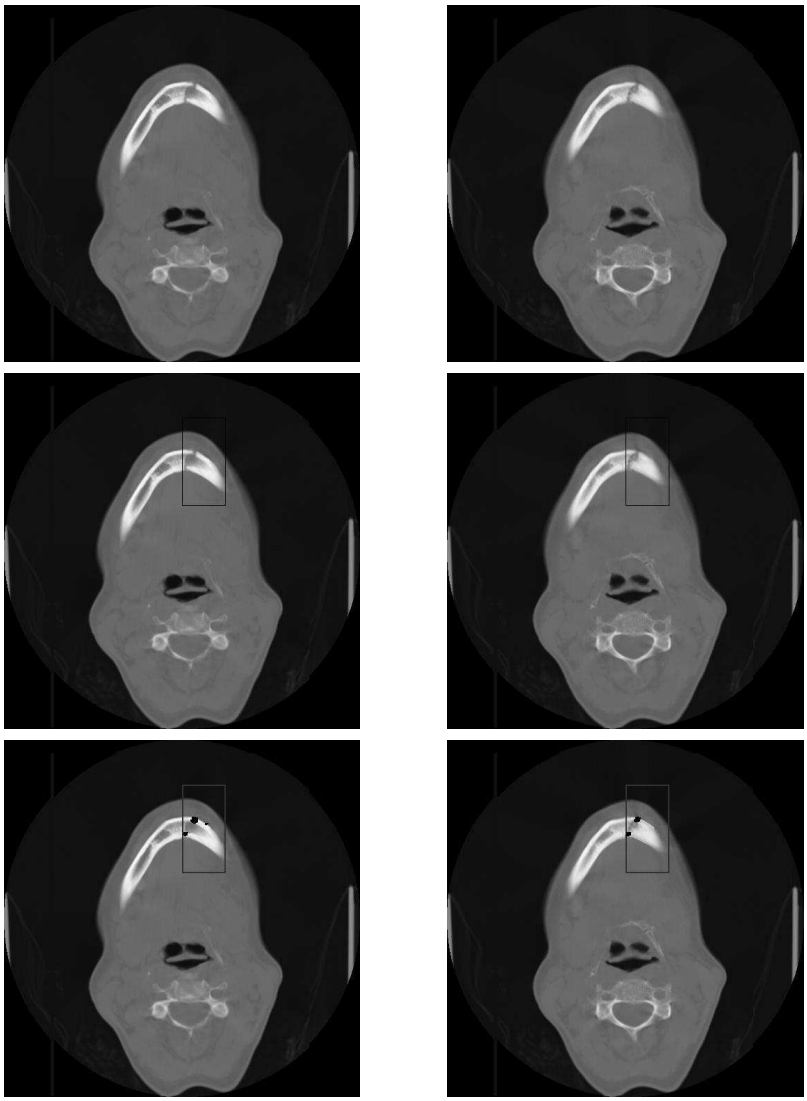

Figure 4.6: Fracture detection for dataset 6 (the top tow shows the input sequence, the middle row shows the localization and the bottom row shows the precise detection of the fracture)

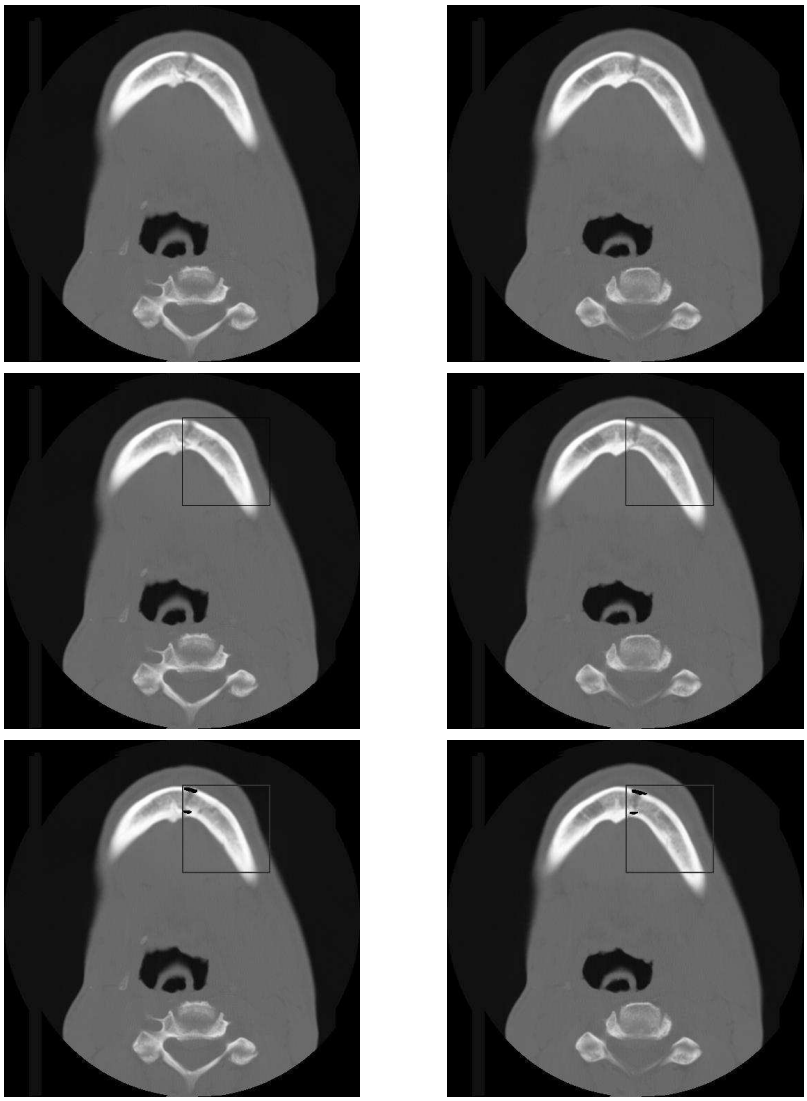

Figure 4.7: Fracture detection for dataset 7 (the top tow shows the input sequence, the middle row shows the localization and the bottom row shows the precise detection of the fracture)

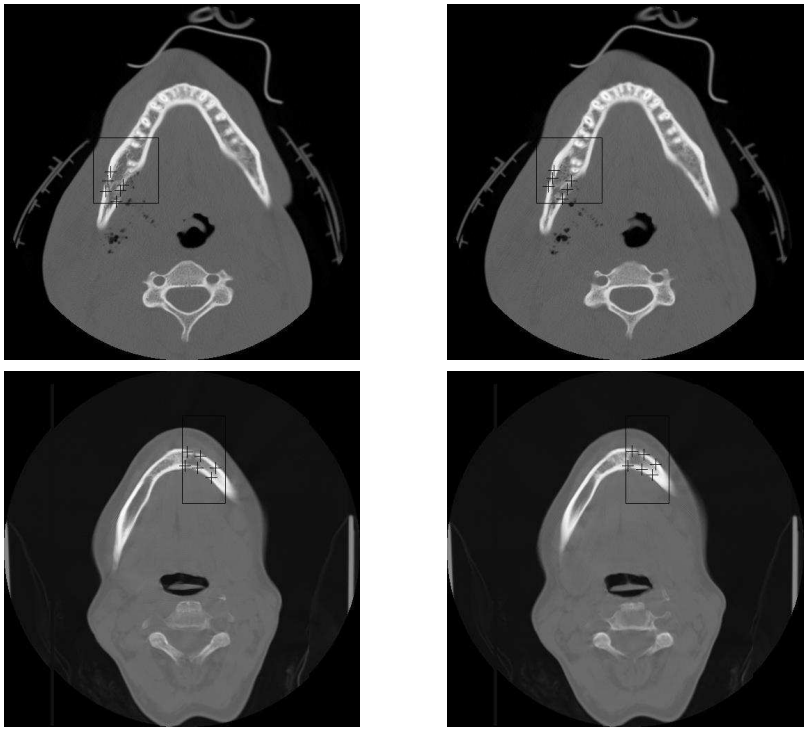

Figure 4.8: Extraction of contour information with mouse clicks (for dataset 1 in the top row and dataset 6 in the bottom row)

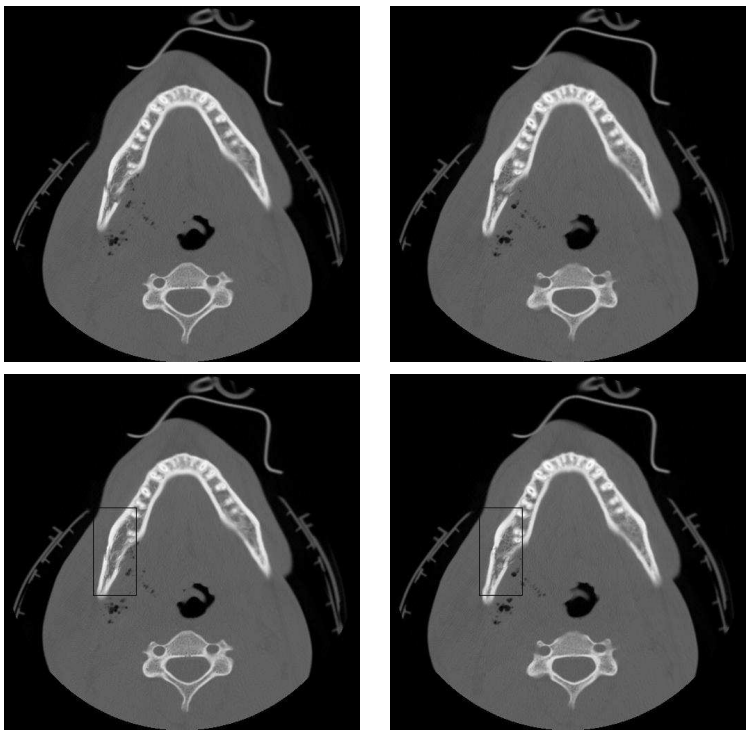

Figure 4.9: Target pattern generation for dataset 1 (the top row shows the fractured jaw and the bottom row shows the reconstructed jaw)

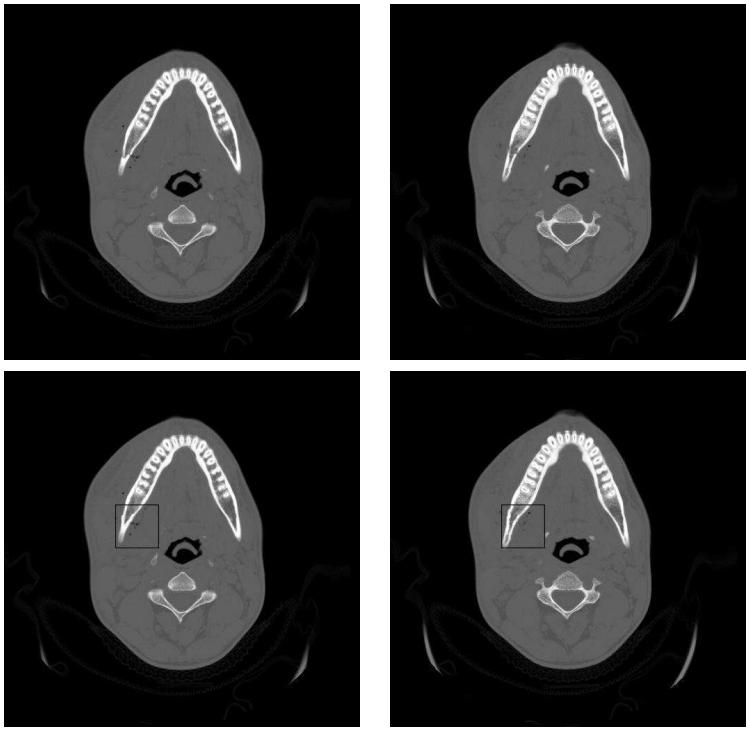

Figure 4.10: Target pattern generation for dataset 3 (the top row shows the fractured jaw and the bottom row shows the reconstructed jaw)

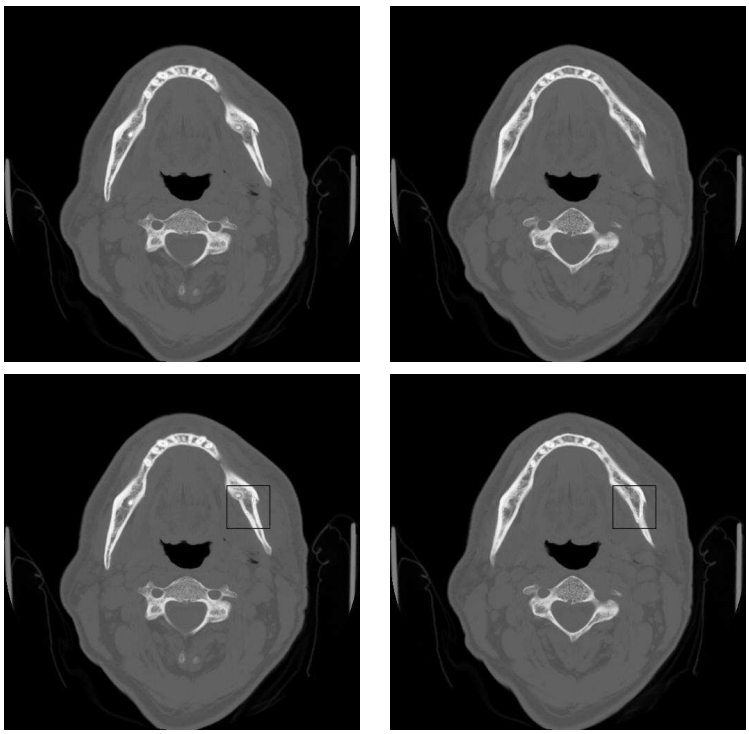

Figure 4.11: Target pattern generation for dataset 5 (the top row shows the fractured jaw and the bottom row shows the reconstructed jaw)

Chapter 5

Stable Fracture Point Detection in Computed Tomography Image Sequences using Bayesian Inference

5.1 Introduction

Introducing automation in various aspects of reconstructive surgery is a highly demanding and technically challenging task. In this work, we employ techniques from computer vision and Bayesian statistics to detect stable fracture points in Computed Tomography (CT) image sequences. The work presented in the chapter constitutes a crucial and integral part of a virtual craniofacial reconstruction scheme. The fracture surface data, which constitute the input to our virtual reconstruction algorithms, were thus far manually extracted with surgeons explicitly identifying the stable fracture points in the CT image sequence. This proved to be a performance bottleneck in attaining the ultimate goal of *in silico* surgery with minimal user intervention. The fracture patterns under consideration are typically characterized by well-displaced broken bone fragments. The proposed scheme reduces considerably the user intervention in the detection of stable fracture points. In addition to the above-mentioned benefit to an important biomedical imaging application, the work has some points of theoretical novelty as well. The Kalman filter, used to check spatial consistency of the observed fracture points is formulated as a Bayesian inference model. Note that the Kalman filter essentially predicts a particular value for a future state (position of a fracture point in the present work) given the present state and the past states. We showed how a limited reliable zone of prediction can be formulated as *Credible Sets* using a Bayesian formulation.

5.2 Literature Review and Our Contribution

In this section, we first discuss various existing techniques for fracture detection and then highlight the novel aspects of the proposed scheme. Existing published literature on fracture detection in X-ray/CT images describes the use of various approaches such as exploitation of anatomical knowledge combined with a *divide-and-conquer* approach by Ozanian and Philips [1]; texture analysis by Yap *et al.* [2]; adaptive interface agent with neural networks by Syiam *et al.* [3]; affine morphological scale space along with iterative peak detection and modified Hough transform by Donnelley and Knowles [4]; probabilistic combination of various classifiers by Lum *et al.* [5] and active contour modeling coupled with shape constraints by Jia and Jiang [6]. As mentioned earlier, the present approach works well for the class of well-displaced fractures. An altogether different approach for detection and localization of minor/hairline fractures using Markov Random Field(MRF) - Maximum A Posteriori probability(MAP) approach can be found in a recent paper by Chowdhury *et al.* [7].

A novel two-step scheme for fracture point identification is proposed in this chapter, which uses computer vision algorithms in conjunction with Bayesian inference. The proposed method is very distinct from any of the aforementioned techniques. In the first stage, we process individual 2D CT slices to extract potential fracture points. Typically, a fracture point is deemed to be a point of high curvature. This initial set of candidate points can be either anatomically correct or spurious. The stability of a fracture point is measured by a figure-of-merit term, where credible sets are used for estimating the spatial consistency. Credible sets are constructed by modeling the standard Kalman filter [8] as a Bayesian inference problem [9]. A preliminary version of the present work appeared in [10], where the experiments were restricted to single-fracture craniofacial phantoms, no detailed statistical analysis was presented and image preprocessing tasks were much more simplified.

The rest of the chapter is organized in the following way: section 5.3 is about image processing, section 5.4 describes the fracture point detection in individual 2D slices, section 5.5 discusses the use of Kalman Filter in a Bayesian Inference paradigm to establish the

spatial consistency of the 2D fracture points in 3D, in section 5.6 we present the experimental results with their analyses and the chapter ends in section 5.7 with a conclusion and outline of future research directions.

5.3 Image Processing

The image processing consists of thresholding and connected component labeling. For, the phantom data, a simple thresholding is sufficient. On the other hand, for real patient data, entropy thresholding is employed to obtain better results. On the thresholded images, connected component labeling along with area based filtering is used. The details are omitted here for avoiding repetition and the reader can go back to section 2.4 for more information.

5.4 Fracture Point Detection in 2D slices

In the first phase of the proposed scheme, we detect the fracture points in the individual 2D CT image slices. This is broadly accomplished in two steps. In the first step, discrete curvature scale space theory is employed to generate an initial pool of potential fracture points. In the second step, the potential fracture points on a component (i.e. bone fragment) in a CT slice are modeled by a cycle graph. A final pool of potential fracture points is selected by coalescing the closely spaced points and filtering out some additional points based on certain geometric constraints.

5.4.1 Generation of an Initial Pool of Fracture Points

As mentioned earlier, a fracture point is essentially a point of high curvature. Thus, we use a simple corner detection technique to generate an initial pool of corners. Throughout the remaining text, the words fracture point and corner will be used synonymously. We follow the discrete curvature scale space based approach for corner detection as outlined in [13]. This method of corner detection is based on estimation of tangent orientation using edge points that are not adjacent in the edge list EL. Let $|EL|$ be the total number of edge pixels of a 2D component, $EL[i]$ be the i^{th} pixel in the edge list EL, k be the number of forward

and backward edge pixels used to determine whether the pixel i is a potential corner, ϕ_{ij} be the angle between any two edge pixels i and j and θ be the threshold angle for corner determination. Note that the value of k determines the scale at which the curvature at an edge point is computed. True corner points can be expected to exhibit sufficiently high curvature values over a substantial range of k (scale) values. The following algorithm detects a corner [13]:

for $i \in [1, |EL|]$
  for $m \in [1, k]$
    $Find\ \phi_{i+m,i-m}$;
    if $(|\phi_{i+m,i-m}| > \theta)$
      $continue$;
    else
      $break$;
    end if ;
  end for ;
  if $\forall m, (|\phi_{i+m,i-m}| > \theta)$
    $mark\ i\ as\ a\ fracture\ point$;
  end if ;
end for ;

Let c be the number of components. Then, the time-complexity of the above algorithm is $O(ck|EL|)$.

5.4.2 Determination of the Final Pool of Fracture Points

By treating each corner as a vertex and assuming an edge between each successive pairs of corners, a weighted cycle graph $G = G(V, E)$ is generated for each component in each 2D CT slice. The weight of the edge connecting any pair of vertices is the Euclidean distance between the corresponding corner points. The closely spaced vertices are coalesced and a corresponding sub-graph $G_1 = G_1(V_1, E_1)$ is constructed. Next, based on a prior knowledge of the range of length and orientation values of an edge that could connect two potential

fracture points; a smaller subgraph $G_2 = G_2(V_2, E_2)$ is constructed. Note that, the lower and upper bounds on length and orientation values of a fractured edge are different for different CT image sequences. After the above values of filtering operations are performed, we are left with a smaller and stronger pool of fracture points. The combined time-complexity of the above two filtering approaches is $O(|E|) + O(|E_1|)$.

5.5 Determination of Stable Fracture Points in a Sequence

In the second phase of our scheme, we establish the consistency of the detected corner points across the CT slices constituting a given CT sequence. Successive 2D CT slices of a given 3D object can be considered as observations at different time instants. Consequently, we track the detected fracture points along successive 2D CT slices and develop a mathematical criterion of spatial consistency.

5.5.1 The Kalman Filter as a Bayesian Inference Process

We first introduce the standard Kalman filter following [8] and then explain how it can be treated as a Bayesian inference problem using [9] and [14]. The state and measurement vectors for a system at a time t are given by the following linear stochastic difference equations respectively [8]:

$$X_t = AX_{t-1} + w_t \tag{5.1}$$

$$Z_t = HX_{t-1} + v_t \tag{5.2}$$

Here $X_t \in \Re^2$ denotes the actual state or parameter vector, and $Z_t \in \Re^2$ denotes the measurement or observation vector. The matrix A in equation (5.1) relates the state vector at the previous time step $t-1$ to the state vector at the current time-step t. Similarly, the matrix H in equation (5.2) relates the state vector to the measurement vector. For the present problem, both A and H are considered as 2×2 identity matrices. We further assume both the process noise w_t and the measurement noise v_t to be normally distributed with zero mean and constant variance Q and R respectively i.e.

$$p(w) \sim \mathcal{N}(0, Q) \tag{5.3}$$

$$p(v) \sim \mathcal{N}(0, R) \tag{5.4}$$

Under the assumption that the initial state vector X_0 is normal with mean μ_0 and variance Σ_0, let us define:

$$\begin{aligned} \mu_{t-1} &= E[X_{t-1}|Z^{t-1}] \\ \\ \Sigma_{t-1} &= var[X_{t-1}|Z^{t-1}] \end{aligned} \tag{5.5}$$

where $Z^{t-1} = [Z_1, ..., Z_{t-1}]$. It is important to note that the Kalman filter leads to a recursive procedure for inference about the state vector X_t. Thus, given the data (measurement) vector $\hat{Z}_t$, inference about X_t can be derived following the well-known Bayes's theorem [9]:

$$\begin{aligned} &Prob.(State\ of\ Nature|Data) \\ &\propto Prob(Data|State\ of\ Nature) \times Prob.(State\ of\ Nature) \\ &which\ can\ be\ mathematically\ written\ as: \\ &P(X_t|Z^t) \propto P(Z^t|X_t, Z^{t-1}) \times P(X_t|Z^{t-1}) \end{aligned} \tag{5.6}$$

In the above equation, the term on the left side represents the *posterior* distribution of X at time t, while the first and the second terms on the right side represent the *likelihood* and *prior* for X, respectively. The *prior* distribution can be written as [14]:

$$(X_t|Z^{t-1}) \sim \mathcal{N}(\mu_{t-1}, \Sigma_{t-1} + Q) \tag{5.7}$$

The *likelihood* function is given by [14]:

$$(Z_t|Z^{t-1}) \sim \mathcal{N}(\mu_{t-1}, \Sigma_{t-1} + Q + R) \tag{5.8}$$

Based on the *prior* density and the *likelihood* given above, the *posterior* distribution can be expressed as [14]:

$$(Z_t|Z^{t-1}) \sim \mathcal{N}(\mu_{t-1} + KF_t(Z_t - \mu_{t-1}), KF_tR) \tag{5.9}$$

KF_t is called the Kalman Filter gain and is given by:

$$KF_t = (\Sigma_{t-1} + Q)(\Sigma_{t-1} + Q + R)^{-1} \tag{5.10}$$

Note that the posterior mean $(\mu_{t-1} + KF_t(Z_t - \mu_{t-1}))$ in equation (5.9) is equal to the prior mean (μ_{t-1}) from equation (5.8) plus an updating term involving the Kalman Filter gain KF_t given by equation (5.10).

5.5.2 Notion of Spatial Consistency

The use of statistical confidence measures is quite ubiquitous in various image processing and computer vision problems including those in the domain of medical imaging. Examples can be found in the works of Ye *et al.* for analyzing and visualizing the performance of two-dimensional parametric shape estimators [15], Subramanian *et al.* for interactive detection and visualization of images of breast lesions from Dynamic Contrast Enhanced Magnetic Resonance Imaging(DCE-MRI) [16], and Simonson *et al.* for binary image registration [17] among several others. We use statistical confidence regions for detecting anatomically stable fracture points in a given CT image sequence. The spatial consistency criterion is developed by introducing the Bayesian prediction intervals. We would prove the following lemmas about the Bayesian prediction intervals:

Lemma 5.1 *The posterior predictive distribution* $(\tilde{Z}_t|Z_t)$ *is given by:*
$(\tilde{Z}_t|Z_t) \sim \mathcal{N}(\mu_{t-1} + KF_t(Z_t - \mu_{t-1}), (KF_t + I)R)$

Proof It can be shown following Gelman *et al.* [18] that the posterior predictive distribution has the same mean as the posterior distribution; whereas its variance is equal to the sum of the prior predictive variance of the model and the variance of the posterior distribution. Thus from equation (5.9), it follows that the posterior predictive mean is given by:
$\mu_{t-1} + KF_t(Z_t - \mu_{t-1})$,
whereas from equation (5.9) and equation (5.4), it follows that the posterior predictive variance is given by:
$(KF_t + I)R$, where I is an identity matrix. $\diamond$

Lemma 5.2 *For the independent univariate case, a* $100(1-\alpha)\%$ *credible prediction square for the state vector* X_t *is given by:*
$\mu_{i(t-1)} + KF_{it}(Z_{it} - \mu_{i(t-1)}) \pm z_{\frac{\tau}{2}}\sqrt{(KF_{it} + I)R_{ii}}, i = 1, 2; \tau = 1 - \sqrt{1-\alpha}$

Proof Note that for a normal random variable Y with mean η and variance σ^2, we can state the following [19]:

$$P[(\eta - z_{\frac{\tau}{2}}) < Y < (\eta + z_{\frac{\tau}{2}})] = 1 - \tau \tag{5.11}$$

where z_β is the upper 100^{th} percentile point of a standard normal distribution. From Lemma 5.1, we can state that the i^{th} component (where $i = 1, 2$; corresponding to the x and y directions) of $(\tilde{Z_{it}}|Z_{it})$ obeys the following normal distribution:

$(\tilde{Z_{it}}|Z_{it}) \sim \mathcal{N}(\mu_{i(t-1)} + KF_{it}(Z_{it} - \mu_{i(t-1)}), (KF_{it} + I)R_{ii})$

Since in the a posteriori distribution the components of the state vector are normally and independently distributed, we get:

$$\begin{aligned}
&P[X_{it} \in (\mu_{i(t-1)} + KF_{it}(Z_{it} - \mu_{i(t-1)}) - z_{\frac{\tau}{2}}\sqrt{(KF_{it} + I)R_{ii}}, \\
&\qquad \mu_{i(t-1)} + KF_{it}(Z_{it} - \mu_{i(t-1)}) + z_{\frac{\tau}{2}}\sqrt{(KF_{it} + I)R_{ii}}),\ i = 1, 2 \mid Z^t] \\
&= \textstyle\prod_{i=1}^{2} P[X_{it} \in (\mu_{i(t-1)} + KF_{it}(Z_{it} - \mu_{i(t-1)}) - z_{\frac{\tau}{2}}\sqrt{(KF_{it} + I)R_{ii}}, \\
&\qquad \mu_{i(t-1)} + KF_{it}(Z_{it} - \mu_{i(t-1)}) + z_{\frac{\tau}{2}}\sqrt{(KF_{it} + I)R_{ii}}) \mid Z^t] \\
&= (1 - \tau)^2 \\
&= (1 - \alpha) \diamond
\end{aligned}$$

Let the Bayesian prediction interval at any time instant t along the i^{th} direction be CS_{it}. Then a fracture point is deemed to be spatially consistent at time point $(t+1)$ if the following condition is satisfied:

$$Z_{i(t+1)} \in CS_{it} \quad where\ i = 1, 2 \tag{5.12}$$

A particular time instant in the present context corresponds to a specific slice in a CT image sequence. In a typical CT image sequence, the fractured mandible appears in a subset of the slices comprising the entire CT image sequence. Since it is assumed that there is no significant bone deformation, the shape of the fracture pattern remains approximately the same over the entire subset. Note that there can be many spurious fracture points detected in the initial pool and some of them may persist after the filtering process. This fact motivates us to perform a spatial consistency check of the observed fracture points across the above subset. Intuitively, the fracture points which conform to the spatial consistency criterion (see equation (5.12))over most of the CT slices in the subset under consideration should be

deemed anatomically stable fracture points for the CT image sequence. A figure-of-merit term (S) is introduced for that purpose. Let n be the total number of slices in the given subset of the original image sequence, m be the number of slices in which a particular fracture point is observed and p be the number of slices in which the fracture point is found to be spatially consistent. Then, S is defined as:

$$S = 0.5(m/n + p/(m-1)) \tag{5.13}$$

The maximum value of S is unity, which occurs when both m/n and $p/(m-1)$ attain their maximum value i.e. unity. The fracture points which yield a high value of S are deemed to be the ones which are anatomically stable and correct. Let us now analyze the expression for S in greater details. Since, the consistency check is performed from the second slice onwards, we have $(m-1)$ instead of m in the denominator of the second term in the equation (5.13). The second term needs a value of p close to $(m-1)$ in order for a fracture point to be anatomically stable and correct. It is important to include the first term i.e. m/n in the expression for the figure-of-merit term S as well. This is because, a fracture point may be found to be consistent in most of the slices in which it appears which results in a high value of $p/(m-1)$. However, the same point may appear in only a few slices which results in a low value of m/n and hence a corresponding low value of S. This fracture point under consideration is definitely not an anatomically true fracture point and the associated low value of S is an indicator of this fact. We deem a corner as stable if its S value exceeds a certain threshold S_{th}. The maximum value for each of the two terms in the equation (5.13) could be 1.0 whereas their minimum values could be 0. So, even if one term assumes a maximum and the other term assumes a minimum value, the overall value of S would be 0.5. Thus S_{th} should be chosen above 0.5 to ensure that a corner point would be stable if and only if it yields a reasonably high value for both the terms constituting the figure-of-merit S.

5.6 Experimental Results and their Analysis

In this section, we present the results of the proposed two-phase fracture detection on one typical phantom and one typical real patient CT image sequence. The total number of

fracture points in the entire sequence, resulting from the application of discrete curvature scale space theory is found to be as high as 642 for the phantom data and 530 for the real patient data (see table (5.1)). After the fracture points in individual CT slices for individual components are modeled as a planar graph and the edge length constraint as well as edge orientation constraint are imposed, the number of potential fracture points is reduced to 136 and 135 for the phantom and the real patient data respectively (see table (5.1)). This is tantamount to about $75-80\%$ reduction of (unreliable) fracture points, which demonstrates the effectiveness of the first phase of corner detection. Note that the above constraints for the edge-length and edge-orientation can be imposed by the user by carefully observing the fracture pattern in the sequence. For example, the edge-length bounds (in pixel distance) for a fracture edge in the planar graph are chosen as 10 and 40 for the real patient data. Similarly, the edge-orientation bounds (in degrees) for a fractured edge in the phantom data are selected as 60 and 90.

Dataset	Nature	Initial Corners	Corners after Phase-I
1	Single Fracture Phantom	642	136
2	Single Fracture Real	530	135

Table 5.1: Typical Corner Statistics after Phase-I

In the second phase of the proposed scheme, we used a Kalman filter modeled along a Bayesian inference paradigm. In the case of the phantom data, upto 8 corners are to appear in different slices of the sequence. We check the consistency of the observed corners using the figure-of-merit term S involving 95% and 99% credible sets. It is important to note that if we choose a very high value of S_{th}, then spurious fracture points are guaranteed to be eliminated but there is a potential risk of missing some stable corners. On the other hand, a low value of S_{th} ensures the detection of true corners along with some additional spurious ones. We have already shown that we need a value of S_{th} to be greater than 0.5. In consideration of the above fact, a value of 0.6 is chosen for S_{th} for both the datasets. It is observed that only 4 out these 8 corners in the phantom CT image sequence have a value of S above 0.6. These are deemed to be anatomically reliable corners (see table (5.2)). The findings are similar in

case of the real patient data as well. In this case we track 9 different corners, out of which 4 are observed to yield values of S higher than S_{th}.

Dataset	Corner No.	S (based on 95% CS)	S (based on 99% CS)
1	1	0.62	0.62
	2	0.84	0.88
(Single	3	0.84	0.86
Fracture	4	0.66	0.69
Phantom)	5	0.46	0.46
	6	0.04	0.04
	7	0.04	0.54
	8	0.06	0.23
$Real-1$	1	0.39	0.39
	2	0.59	0.59
(Single	3	0.63	0.63
Fracture	4	0.12	0.12
Real)	5	0.84	0.90
	6	0.09	0.09
	7	0.88	0.90
	8	0.90	0.93
	9	0.32	0.46

Table 5.2: Typical Corner Statistics after Phase-II

The quantitative results in the tables above (table (5.1) and table (5.2)) are visually supported in figure (5.1) and figure (5.2). A potential fracture point in figures (5.1) and (5.2) marked by a dark cross. The number of potential fracture points are shown for two consecutive phantom and real patient CT slices in figure (5.1) and figure (5.2) respectively.

The value of S remains approximately the same (as expected) when we switch between 95% and 99% credible sets computation. In the case of corner 7 in the phantom dataset, we see a jump in the value of S from 0.04 to 0.54. This sharp change in the value of S is contributed by the second factor in equation(5.13), more specifically by a change in the value of p from 0 to 1. Note that since the higher value of S is still less than S_{th}, the corresponding fracture point is deemed to be unreliable. In a hypothetical case, where the S value for a corner is below S_{th} for a 95% credible set and above S_{th} for a 99% credible set, we take a conservative approach to solve the anomaly. In such situations, we deem the fracture point to be anatomically unstable. The anatomically stable fracture points obtained from

the experimentation are verified by the surgeons. The entire process of fracture detection takes well less than a minute on a 1.73 GHz *Intel*© *Pentium*©*M* Processor.

5.7 Conclusion and Future Directions

A novel two-phase scheme for semi-automatic mandibular fracture detection from CT image sequence is proposed in this chapter. The class of fracture patterns under consideration consist of well-displaced broken fragments. In the first phase of the proposed two-phase approach, discrete curvature scale space theory is employed to identify an initial pool of high-curvature points. This is followed by a filtering technique that exploits a cycle graph-based representation of the fracture points on a bone fragment in a 2D CT slice. In the second phase, we use a Kalman Filter from the Bayesian Inference perspective and construct Bayesian prediction intervals for the verification of spatial consistency. A figure-of-merit term is subsequently introduced, a high value of which indicates an anatomically stable and correct fracture point. The contribution of the chapter from the biomedical imaging perspective lies in enhancing the degree of automation in virtual reconstructive surgery. From a theoretical standpoint, the formulation of the figure-of-merit term, with underlying specification of a reliable zone for spatial consistency using Bayesian Credible Sets, deserves special mention. Future work will aim at extending the proposed scheme for detecting fracture points in a multiple fracture scenario. In addition, we plan to use bivariate analysis for constructing highest posterior density credible sets [18]. We also plan to explore the Extended Kalman Filter [8] and Particle Filter [20] in more complex fracture point tracking scenarios involving clutter and highly nonlinear movement of the fracture points.

5.8 References

[1] T. Ozanian and R. Phillips, “Image Analysis for Computer-Assisted Surgery of Hip Fractures”, Med Image Anal, 4(2) (2000) 137 - 159.

[2] D. W. H. Yap, Y. Chen, W. K. Leow, T.S. Howe, and M. A. Png, “Detecting Femur

Fractures by Texture Analysis of Trabeculae", in Proc. of Int. Conf. on Pattern Recognition (ICPR), Cambridge, UK, 2004, 730-733.

[3] M. Syiam, M.A. El-Aziem and M. El-Mensshawy, "Adgen: Adaptive Interface Agent for X-Ray Fracture Detection", Proc. of IEEE Int. Conf. on Electrical, Electronic and Computer Engineering (ICEEC), Cairo, Egypt, 2004, 354 - 357.

[4] M. Donnelley and G. Knowles, "Automated Bone Fracture Detection", in Proc. of SPIE Medical Imaging, San Diego, USA, 2005, 955 - 966.

[5] V. Lum, W. Leow, Y. Chen, Y. Howe and M. Png, Combining classifiers for bone fracture detection in X-ray images, in Proc. of Int. Conf. on Image Processing (ICIP), Genoa, Italy, 2005, 1149 - 1152.

[6] Y. Jia and Y. Jiang, "Active Contour Model with Shape Constraints for Bone Fracture Detection", in Proc. of European Conf. on Colour in Graphics, Imaging, and Vision (CGIV), Leeds, UK, 2006, 90-95.

[7] A.S. Chowdhury, A. Bhattacharya, S.M. Bhandarkar, G.S. Datta, J.C. Yu and R. Figueroa, "Hairline Fracture Detection using MRF and Gibbs Sampling", in Proc. of IEEE Wkshp. on Applications of Computer Vision (WACV), Austin, TX, 2007, p. 56.

[8] G. Welch and G. Bishop, "An Introduction to the Kalman Filter", Tech. Report, No. 95-041, UNC Chapel Hill, 2004.

[9] R. J. Meinhold and N.D. Singpurwalla, "Understanding the Kalman Filter", Amer Statist, 37(2) (1983) 123-127.

[10] A.S. Chowdhury, S.M. Bhandarkar, G. Datta and J.C. Yu, "Automated Detection of Stable Fracture Points In Computed Tomography Image Sequences", in Proc. of IEEE Int. Symp. on Biomedical Imaging (ISBI), Arlington, VA, 2006, 1320 - 1323.

[11] G.N. Hounsfield, Nobel Award Address, Computed Medical Imaging, Med Phys, 7(4) (1980) 283-290.

[12] P.K. Sahoo, S. Soltani, K.C. Wong and Y.C. Chen, "A Survey of Thresholding Techniques", Comput Vis Graph Image Process, (41) (1988) 233-260.

[13] R. Jain, R. Kasturi and B.G. Schunck, 1995. Machine Vision, McGraw Hill, NY, Chapter 6.

[14] D. Pena and I. Gutman, "Bayesian Approach to Robustifying the Kalman Filter", In Bayesian Analysis of Time Series And Dynamic Models, J. Spall (Ed.), Marcel Dekker, NY, 1988, pp. 227 - 253.

[15] J.C. Ye, Y. Bresler and P. Moulin, "Asymptotic Global Confidence Regions in Parametric Shape Estimation Problems", IEEE Trans Inform Theory, 46(5) (2000) 1881-1895.

[16] K.R. Subramanian, J.P. Brockway and W.B. Carruthers, "Interactive detection and visualization of breast lesions from dynamic contrast enhanced MRI volumes", Comput Med Imaging Graph, 28(8) (2004) 435-444.

[17] K.M. Simonson, S.M. Drescher Jr. and F.R. Tanner, "A Statistics-Based Approach to Binary Image Registration with Uncertainty Analysis", IEEE Trans Pattern Anal Mach Intell, 29(1) (2007) 112-125.

[18] A. Gelman, J.B. Carlin, H.S. Stern and D.B. Rubin, Bayesian Data Analysis, Chapman & Hall, CRC, FL, 2004.

[19] J. Neter, M. Kutner, W. Wasserman and C. Nachsteim, Applied Linear Statistical Models, McGraw Hill, NY, 2002.

[20] P. Perez, J. Vermaak and A. Blake, "Data Fusion for Visual Tracking with Particles", Proc. IEEE, 92(3) (2004) 495-513.

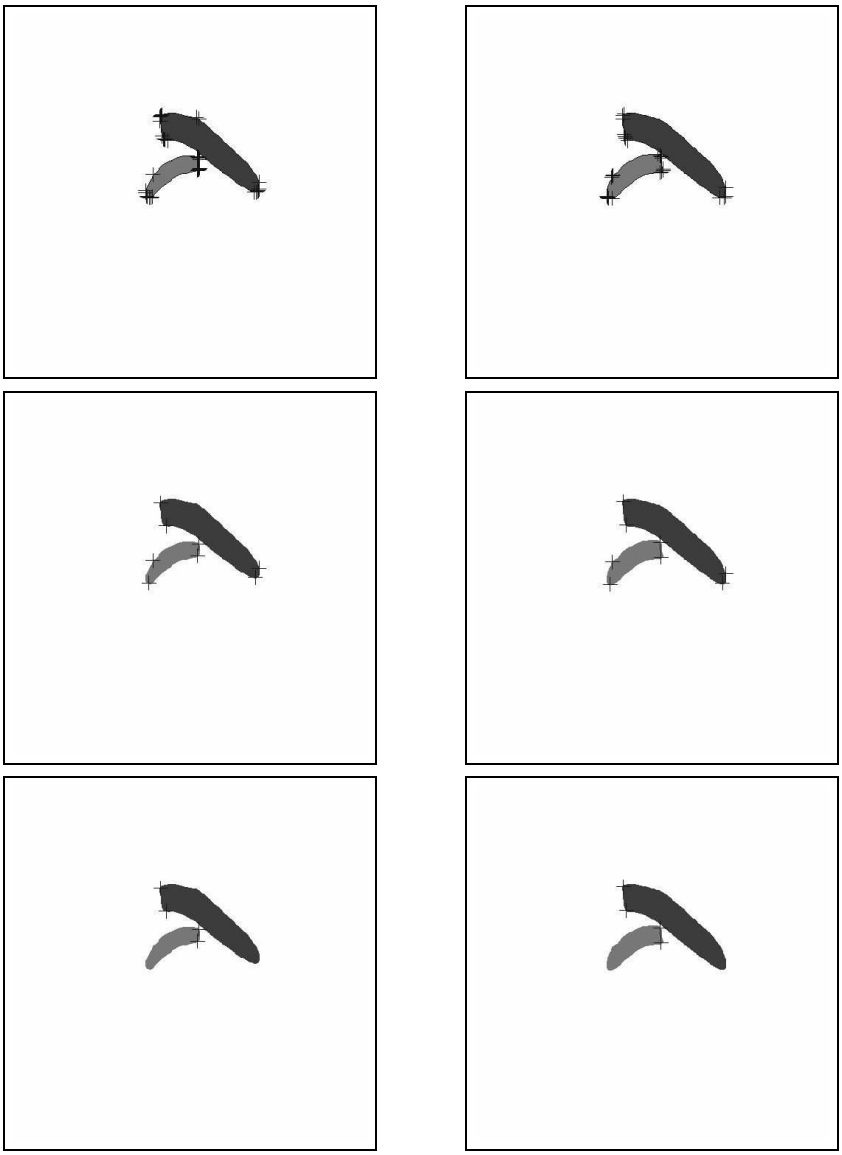

Figure 5.1: The first row shows the result of fracture points identified using discrete curvature scale space theory on two successive phantom CT slices; the second row shows the result of filtered out fracture points (after phase-I) on the same; the third row shows the consistent corners following Bayesian inference (after phase-II) on the same. The centers of the dark crosses indicate a fracture point.

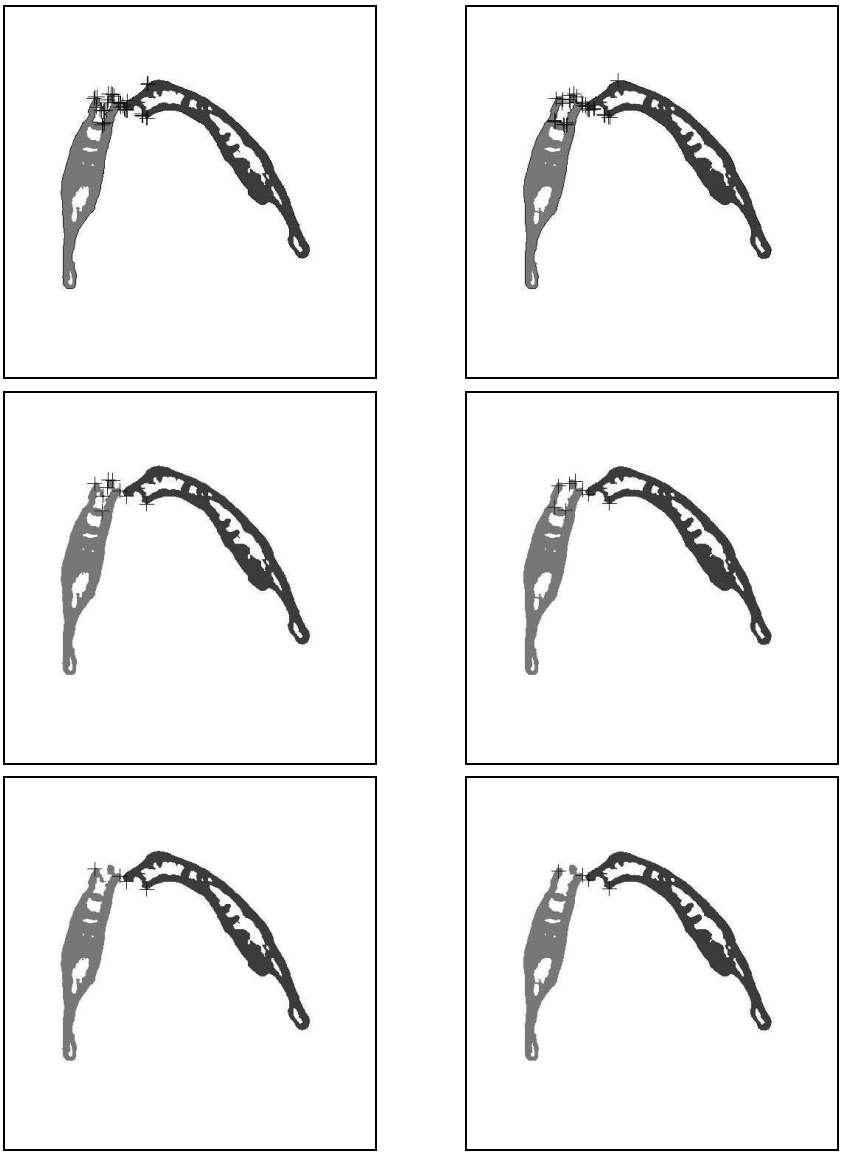

Figure 5.2: The first row shows the result of fracture points identified using discrete curvature scale space theory on two successive real patient CT slices; the second row shows the result of filtered out fracture points (after phase-I) on the same; the third row shows the consistent corners following Bayesian inference (after phase-II) on the same. The centers of the dark crosses indicate a fracture point.

Chapter 6

Mandibular Fracture Detection using Max-Flow Min-Cut

6.1 Introduction

In the present chapter, we apply a different detection technique for mandibular fractures. Mandibular fractures exhibit certain distinct patterns in X-ray or CT images, as described in [1]. As mentioned earlier in this thesis, the fractures could be either a) *hairline/minor* (the broken bone fragments are not visibly out of alignment or have incurred very little relative displacement) or b) *major*(the broken fragments are clearly displaced relative to each other). In chapter 4, we model a minor fracture as a stochastic degradation of a hypothetical intact mandible. Here, we model a fracture as a *discontinuity/cut* in the flow of intensities between two designated points, called the *source* and the *sink*. A fracture is detected by obtaining the minimum cut using the well-known Maximum-Flow Minimum Cut algorithm by Ford and Fulkerson [2]. This approach of fracture identification gives more promising results for minor fractures with very little image pre-processing required. We first treat a sequence of 2D CT image slices as independent 2D graphs and execute the flow algorithm on each such graph. Later, we treat the set of slices with fractured mandible as one complete 3D graph and run the same flow algorithm on it. It appears that use of one complete 3D graph gives better results for visualizing fracture. We also examine the magnitude of the flow as an approximate measure of the extent of the fracture.

The rest of the chapter is organized as follows: in section 6.2, we discuss the related work and highlight our contribution. In Section 6.3 we present key definitions and some results pertaining to network flow. In section 6.4 and 6.5, we describe respectively the fracture detection procedure in individual 2D CT image slices and 3D CT image stack considered as

a whole. Section 6.6 is devoted to the presentation and analysis of experimental results. In section 6.7 the paper is concluded with an outline of future research directions.

6.2 Literature Review and Our Contribution

In this section, we first review previous applications of Graph Cuts in the area of computer vision with special emphasis on medical image analysis. Existing approaches for fracture detection in X-ray/CT images are reviewed next. The use of energy minimization *via* graph cuts was first introduced by Boykov *et al.* [3] for the purpose of image segmentation. Boykov and Jolly [4] presented experimental results of graph cut-based segmentation on abdominal CT images in 2D and 3D. Xu *et al.* [5] enhanced the peformance of graph cuts for image segmentation by the addition of active contours. The capacity function of Boykov and Jolly [4] consisted of intensity of the pixels and distance between the pixels. Freedman and Zhang [6] introduced shape-based priors in their work on graph cut-based segmentation based on the above framework. Funka-Lea *et al.* [7] used graph cuts for automatic heart isolation in their work on CT coronary visualization. Similarly, Song *et al.* [8] used an adaptive version of the graph cut with tissue-based prior for brain MRI segmentation. It is to be noticed that most researchers have employed the framework of Boykov and Jolly [4] with different forms of energy functions. For a recent as well as comprehensive coverage on graph cuts for N-D image segmentation, the reader is referred to the paper by Boykov and Jolly [9].

The extant literature on fracture detection in X-ray/CT images describes use of various approaches. Exploitation of anatomical knowledge was combined with a *divide-and-conquer* approach by Ozanian and Philips [10]. Texture analysis was performed by Yap *et al.* [11] and an adaptive interface agent with neural networks was employed by Syiam *et al.* [12]. An affine morphological scale space along with iterative peak detection and modified Hough transform was used by Donnelley and Knowles [13]. Probabilistic combination of various classifiers was undertaken by Lum *et al.* [14] and an active contour modeling coupled with shape constraints was employed by Jia and Jiang [15]. An example of semi-automated fracture detection scheme for the class of major mandibular fractures can be found in Chowdhury *et al.* [16]. On the

other hand, a MRF-MAP based approach for minor mandibular fractures can be found in another work by Chowdhury *et al.* [17].

In the context of mandibular fracture detection, the focus is on finding discontinuities or cuts in the boundaries of a broken mandible rather than image segmentation exclusively. Our principal contribution lies in the innovative mathematical modeling of the problem of fracture detection. Given a 2D slice, the two condyles in a human mandible seem to be the natural choices for the source and the sink in a network flow-based approach for mandibular fracture detection. In the case of an unbroken mandible, the value of the maximum flow between the two condyles is expected to be very high. For a fractured mandible, there is a considerable drop in the value of the maximum flow. The location of a minimum cut marks the occurrence of a fracture, and the magnitude of the flow provides an indication of the extent of the fracture. To the best of our knowledge, no maximum flow-minimum cut approach has previously been taken for detecting any type of fracture, and certainly not for mandibular fractures.

6.3 Network Flows

In this section, we will describe basic graph theoretic concepts for flow in networks following [18]. Some theorems used for this work are also stated without proof. For proof, the reader can see well-known texts on graph theory such as [18] and [19].

Definition 6.1 *A* **flow network** $G = (V, E)$ *is a directed graph in which each edge* $(u, v) \in E$ *has a nonnegative capacity* $c(u, v) \geq 0$*. Two vertices in the flow network are distinguished as a source* s *and a sink* t*.*

Definition 6.2 *A* **flow** *in* G *is a real-valued function* $f : V \times V \to \Re^+$ *that satisfies the following properties:*

$$\forall u, v \in V,\ f(u, v) \leq c(u, v) \tag{6.1}$$

$$\forall u, v \in V,\ f(u, v) = -f(v, u) \tag{6.2}$$

$$\forall u \in V - \{s, t\},\ \sum_{v \in V} f(u, v) = 0 \tag{6.3}$$

The quantity $f(u, v)$ is called the flow from the vertex u to vertex v.

Definition 6.3 *The* **value** *of a flow is defined as:*

$$|f| = \sum_{v \in V} f(s, v) \tag{6.4}$$

that is, the total flow out of the source.

Definition 6.4 *Given a flow network $G = (V, E)$ and a flow f, the* **residual graph** *of G induced by f is $G_f = (V, E_f)$ where $E_f = ((u, v) \in V \times V : c_f(u, v) > 0)$*

Definition 6.5 *Given a flow network $G = (V, E)$ and a flow f, an* **augmenting path** *p is a simple path from s to t in the residual network G_f.*

Definition 6.6 *A* **cut** *(S, T) of a flow network $G = (V, E)$ is a partition of V into S and $T = V - S$ such that $s \in S$ and $t \in T$.*

Definition 6.7 *The* **capacity** *of a cut (S, T) is the sum of the capacities of the edges from S to T.*

Theorem 6.1 *For any graph the maximum flow value from s to t is equal to the minimal cut capacity of all cuts separating s and t. This is known as* **Max-flow Min-Cut theorem**.

Theorem 6.2 *If the capacity function c is integral valued, there exists a maximal flow f that is also integral valued. This is called the* **Integrity Theorem**.

The above definitions can be extended to multi-source, multi-sink settings. It is then straightforward to prove the following theorem, which establishes an equivalence with a single source single sink problem.

Theorem 6.3 *Maximum flow in a graph with multiple sources $s_1, s_2, ..., s_n$ and multiple sinks $t_1, t_2, ..., t_n$ is induced by a maximum flow in a simple equivalent graph with an added hypersource s^* and a hypersink t^* with capacities $c(s^*, s_i) = \infty$ and $c(t_i, t^*) = \infty$. This is called the* **Multi-Source Multi-Sink Maximum-flow Minimum-cut theorem**.

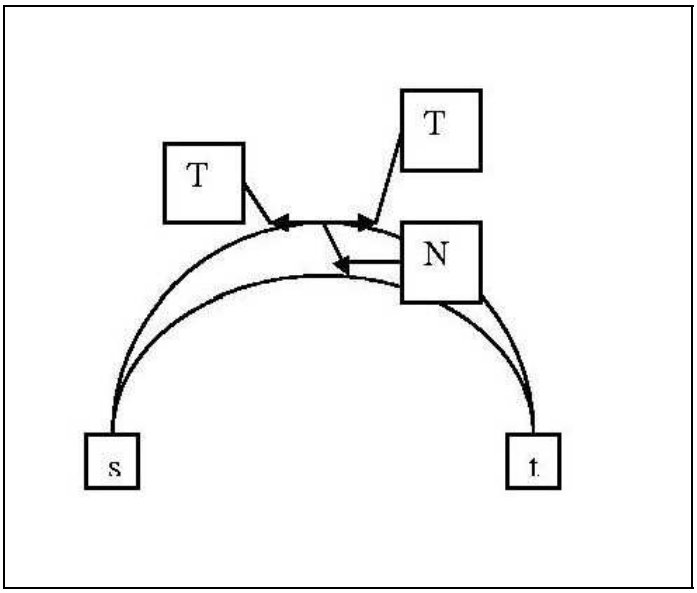

Figure 6.1: A 2D flow network with a source s, a sink t and typical tangential (T) and normal (N) edges.

6.4 Max Flow Min Cut in 2D

In this section, we first discuss the construction of the flow network for a 2D CT slice with suitable choice of vertices, edges and capacity functions as edge weights. We will then justify our claim of correct mathematical modeling of the fracture detection problem as equivalent to identification of a minimum cut in the flow network, as defined above.

6.4.1 Construction of the flow network

In their formulation of flow network, Boykov and Jolly [4] choose all the pixels in an image as the vertices and establish edge connections amongst the 8 pixel neighbors. In the context of fracture detection, we take a different approach to the construction of the flow network $G = (V, E)$. It is noticed that a typical minor fracture appears at the bone contours. Even in the case of a major fracture, a break in the bone contours is prominently visible. This fact motivates us to choose the set of boundary pixels BP on the two mandibular contours (i.e. the inner and the outer contour) as the vertices of the proposed flow network.

We identify the two condyles which are anatomical landmark points at the two terminals of the jaw as natural choices for the source vertex s and the sink vertex t. Thus $V = BP \cup \{s, t\}$. Since the boundary pixels for a mandible are essentially on an arc, we construct *tangential* (T) and *normal* (N) edges. For each boundary pixel on any particular mandibular contour, we create edge links with the immediate forward and backward neighboring pixels. These constitute the T edges. On the other hand, the N edges are established between any two normal (or near-normal) boundary points across the two contours. In addition the first boundary pixel of both the contours (fvt, fvb) are attached to the source (s) and the last boundary pixel of both the contours (lvt, lvb) are attached to the sink (t). Therefore

$$E = T \cup N \cup \{(fvt, s), (fvb, s), (lvt, t), (lvb, t)\}$$

The rationale behind having tangential and normal neighbors are guided by the geometry of the mandible as well as by the fracture pattern. A fracture can occur along the two mandibular contours (covered by tangential edges) or across these contours (covered by normal edges). Let bp_k and bp_l be any two consecutive points on one contour of a mandible with coordinates (bp_{kx}, bp_{ky}) and (bp_{lx}, bp_{ly}) respectively. Then the equation of the line that is normal to the contour at point bp_k is given by:

$$(bp_{lx} - bp_{kx})x + (bp_{ly} - bp_{ky})y + (bp_{kx}(bp_{kx} - bp_{lx}) + bp_{ky}(bp_{ky} - bp_{ly})) = 0 \tag{6.5}$$

In order to be a normal neighbor to the point bp_k, a point on the other contour should ideally satisfy equation (6.5). Since it is not always possible to find the exact normal neighbor (primarily due to sampling error), we compute the distance d_{kN} of any competing candidate point (bp_{kn}) (with coordinates (bp_{knx}, bp_{kny})) and choose the one yielding the minimum value of d_{kN}. From basic coordinate geometry, we can write:

$$d_{kN} = \frac{Abp_{knx} + Bbp_{kny} + C}{\sqrt{A^2 + B^2}} \tag{6.6}$$

where $A = (bp_{lx} - bp_{kx}), B = (bp_{ly} - bp_{ky}), C = (bp_{kx}(bp_{kx} - bp_{lx}) + bp_{ky}(bp_{ky} - bp_{ly}))$. We choose a very simple capacity function as an edge weight between any pixel pair, with intensity and distance as the two parameters. Let I_p and I_q be the intensities of two pixels

p and q and let d_{pq} be the Euclidean distance between them. Then the capacity function c_{pq} is given by:

$$c_{pq} = \frac{I_p I_q}{d_{pq}} \tag{6.7}$$

Since a typical fracture is marked by loss of bone, the intensity at a fracture site has a lower intensity than the surrounding bone. Additionally, the distance between two boundary pixels would be relatively higher if it encompasses a fracture site. Moreover, the influence of tangential neighbors would be greater than that of the normal neighbors due to the incorporation of the (Euclidean) distance in the capacity function. This justifies the choice of the capacity function, as given by equation (6.7). Very high capacity values were assigned to the edges connecting fvt and fvb to source s and sink t to lvt and lvb. By construction, all edges in our flow network have capacity > 0. Schematic diagram of a 2D flow network is shown in figure (6.1).

6.4.2 Correctness of the Modeling

The purpose of this subsection is to provide an intuitive justification about the correctness of our modeling of fracture detection as a graph cut. We follow the framework of Boykov and Jolly [4]. From the definition, every cut C on the flow network G satisfies following two properties:

1. C groups the vertices of G into two disjoint sets.

2. One set will contain the source s and the other set will contain the sink t.

Claim 6.1 *A minimum cut C^* correctly identifies a fracture in our flow-graph G.*

Justification: The justification is based on Theorem 6.1 and the construction of our graph with capacity function given by equation (6.7). We seek to determine the maximum flow between s and t. Using Theorem 6.1, we obtain the minimum cut C^*. The minimum cut will consist of the cut edges in our flow network G. Basically, the cut edges are edges with comparatively low capacity values. From equation (6.7) it is evident that the low capacity edges are edges with relatively lower pixel intensity values and relatively higher distance

values. These are exactly the characteristics of an edge in the vicinity of a fracture site. Thus, identification of a minimum cut corresponds to detection of a fracture. $\diamond$

Note that the importance of Theorem 6.2 lies in making the *Ford-Fulkerson* algorithm finite and is mentioned here for the sake of completeness [19]. The computation of the augmenting path was done using a *breadth-first search*, as outlined in the *Edmonds-Karp* algorithm [18]. This implements the *Ford-Fulkerson* algorithm in worst case time $O(VE^2)$.

6.5 Max Flow Min Cut in 3D

In this section we extend the results of the previous section to 3D. As mentioned earlier, the input to our problem is a 2D CT image sequence of a fractured mandible. We can run the 2D flow algorithm separately for each 2D image slice. In fact, the resolution along the z-axis of the CT sequence is much lower than the 2D resolution, which raises serious doubts about the utility of the 3D model. We use simple volume interpolation along the z-axis to make the voxels cubes instead of rectangular parallelepipeds and the whole sequence a more natural setting for a 3D graph cut.

For the 3D flow network $G_{3D} = (V_{3D}, E_{3D})$, we add a hypersource s^* below the left condyle in the first slice and a hypersink t^* below the right condyle in the last slice. Thus, the new vertex set becomes

$$V_{3D} = \{s^*, t^*\} \cup \bigcup_{i \in ns} V_i$$

where ns is the no. of slices and V_i denotes the set of vertices in the i^{th} slice. For the set of edges, we add a set of axial edges A, edges from s^* to individual 2D sources s_i and edges from the individual 2D sinks t_i to t^*. A very high capacity value was assigned to the edges connecting s^* to the s_i's and t_i's to t^*. The set of axial edges contain edges between pixels on two adjacent slices with same orientation. Thus, the new edge set becomes

$$E_{3D} = A \cup \bigcup_{i \in ns} (\{(s_i, s^*), (t_i, t^*)\} \cup E_i)$$

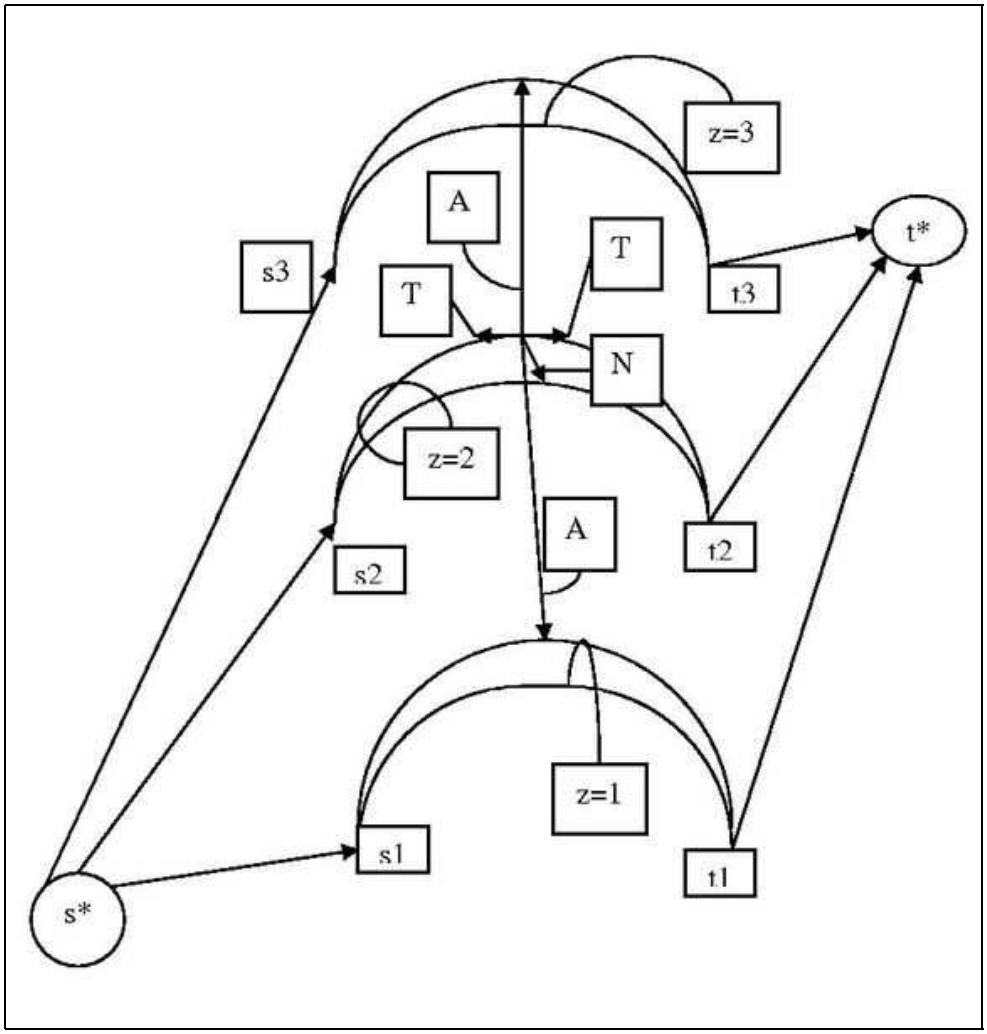

Figure 6.2: A 3D flow network for 3 consecutive slices with a hypersource s^* and a hypersink t^*, individual sources s_1, s_2, s_3 and sinks t_1, t_2, t_3 for the 2D CT slices with $z = 1, z = 2, z = 3$ respectively and typical Tangential (T), Normal (N) and Axial (A) edges.

Schematic diagram of a 3D flow network is shown in figure (6.2). Now, we state the following claim for the 3D flow network, which is an extension of the one used for 2D:

Claim 6.2 *A minimum cut C^{3D*} correctly for our flow network G_{3D} identifies a fracture.*

Justification: Based on Theorem 6.3 the maximum flow problem in a multiple source multiple sink flow network becomes a maximum flow problem in an equivalent graph with a single source and a single sink. Our construction of the 3D flow network already satisfies the construction criterion of Theorem 6.3. Subsequently, we can use the same argument in the justification of Claim 6.1 to complete an intuitive proof for the present claim. $\diamond$

6.6 Experimental Results and Analysis

We begin this section by showing the difference in the maximum flow value between an intact mandible and a fractured mandible. This difference is mainly due to the presence of a fracture. The value of the maximum flow is found to be 44850 for the unbroken and 6201 for the broken mandible respectively (see figure (6.3)).

We next illustrate the impact of the 2D max flow-min cut algorithm for three different sets of mandibles, as shown in figure (6.4). Note that the fractures were identified accurately for all the 3 cases. However, for the mandible in the third row, some additional spurious pixels near the sink were detected as fractures. This calls for a more robust capacity function than the one presented in, which would be one direction of future research.

In figure (6.5) we show how the value of a maximal flow can be used as an approximate measure of the extent of the fracture. The fracture in the second row is simulated by translating one of the fragments by a predetermined distance. The value of the maximum flow is found to be 2470 for the fracture in the second row as compared to a value of 6201 in case of the original fracture in the first row. Thus greater the extent of the fracture, less the magnitude of the maximum flow.

We conclude this section with an example of a 3D graph cut shown in figure (6.6). There are originally 3 image slices containing the fractured mandible in the original CT image sequence. After volume interpolation, the number of slices is increased to 6. The hypersource

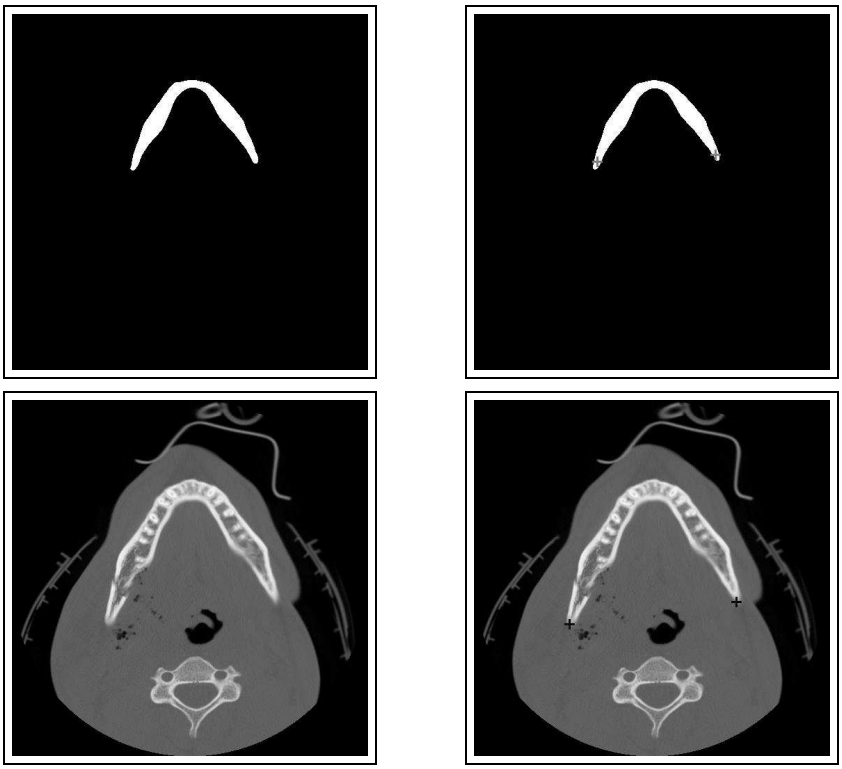

Figure 6.3: The first row shows an unbroken mandible followed by the same with identified source and sink; the second row shows a broken mandible followed by the same with identified source and sink. The centers of the crosses mark the source and the sink.

node is in the first slice and the hypersink node is in the last slice. These are marked by large white crosses. The source and sink vertices in individual CT image slices are marked by the smaller dark crosses. Once again, the fractures are indicated by dark squares. It is found that running the max floe-min cut algorithm over a 3D flow network results in a better visualization of the fractures than running the max flow-min cut algorithm over individual 2D slices. The max flow-min cut algorithm on the 3D graph takes about a minute to complete on a 1.73 GHz $Intel^{©}$ $Pentium^{©}M$ Processor whereas the max flow-min cut algorithm on the 2D graph takes a few seconds to complete its execution on the same machine. A surgeon can opt for sequence of 2D graph cuts to visualize the same fracture by saving more time at the cost of slightly poorer visualization. One can possibly identify the broken fragments by following the augmenting paths in the flow network containing minimum cut edges.

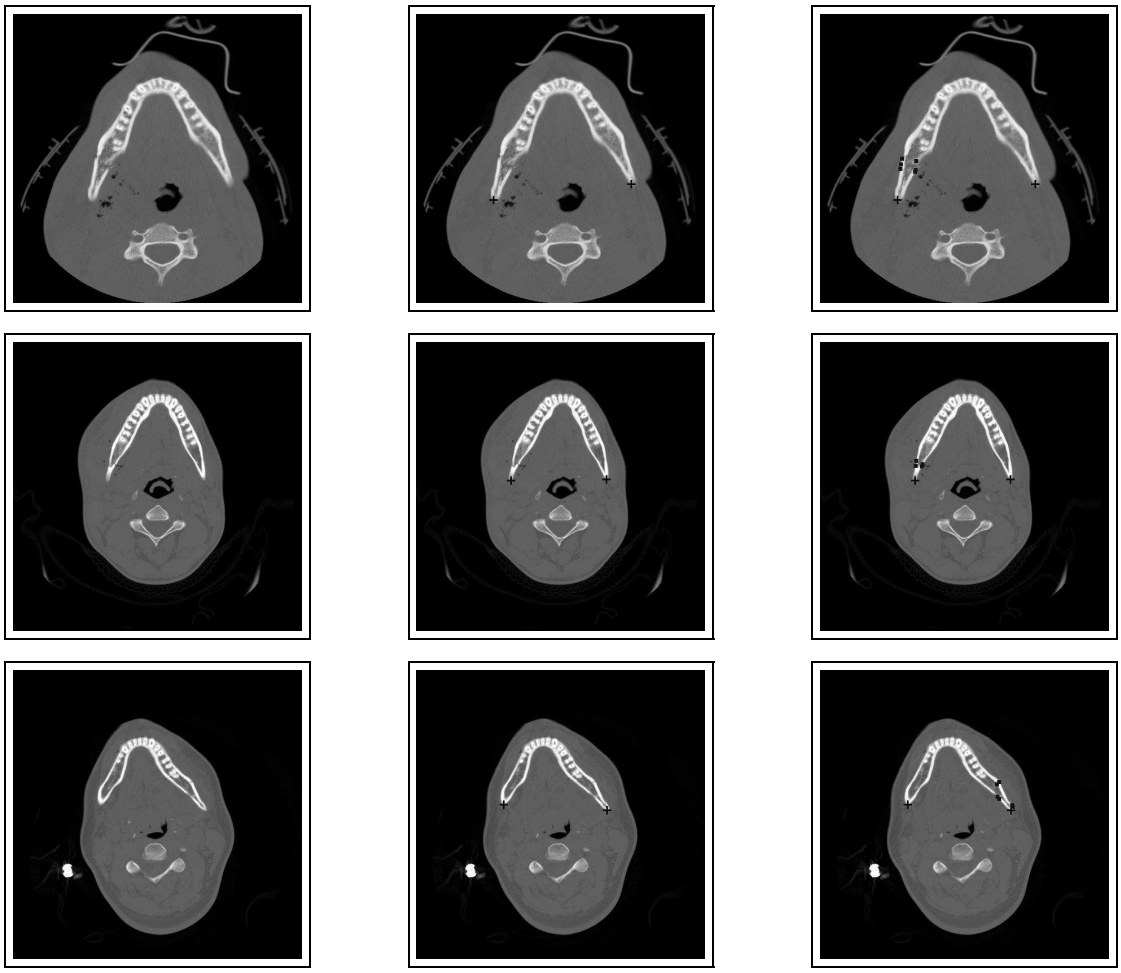

Figure 6.4: The first row shows a fractured mandible, followed by the same with the source and sink vertices identified, followed by the same with fractures identified; the second and third rows convey the same information as the first row for different sets of mandibles. The centers of the crosses mark the source and the sink vertices and the fractures are marked by dark squares

6.7 Conclusion and Future Directions

In this chapter, we present a novel way of detecting mandibular fractures. A fracture is modeled as a minimum cut in the well-known max flow-min cut algorithm by Ford-Fulkerson. The method requires negligible user intervention as identification of the source vertex, sink vertex and flow paths are done automatically. However, the user needs to provide a value for the bone intensity for the purpose of boundary detection. We applied the above algo-

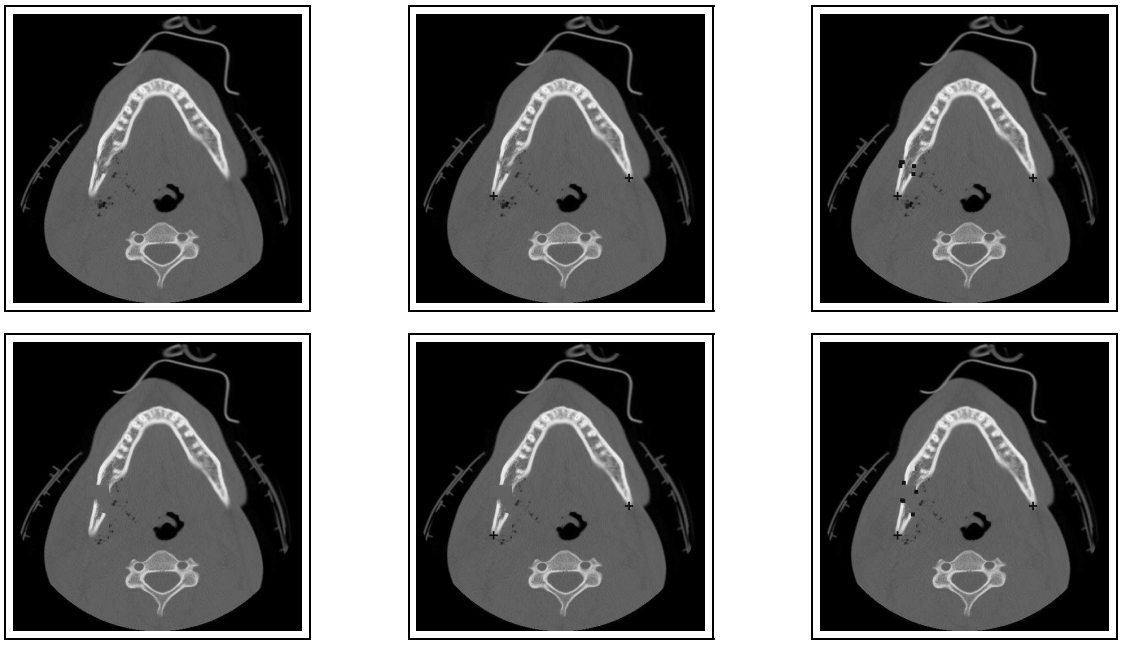

Figure 6.5: The first row shows a broken mandible, followed by the same with identified source and sink, followed by the same with identified fractures; the second rows the above mandible with an increased fracture, followed by the same with identified source and sink, followed by the same with identified fractures. The centers of the crosses mark the source and the sink and the fractures are marked by dark squares

rithm in both 2D and 3D. The flow network is constructed based on the geometry of the human mandible and some knowledge of the fracture pattern. Simple capacity functions were designed as edge weights.

The future work would focus on making the capacity function more robust by incorporation of domain knowledge and shape priors (e.g. see [6]). A mandibular fracture is often associated with tissue swelling and presence of specific low intensity regions called emphysema [20]. For example, we can make the edge weights in the vicinity of an emphysema more inexpensive and thus make them more likely candidates for a minimum cut. We can add some more normal edges by looking within a small solid angle subtended by a particular pixel in 2D and that by a voxel in 3D. The pixels (voxels) lying within the solid angle of any pixel can be considered as approximate normal neighbors. This would make the resulting graph more dense but may yield better results. The 2D graph cut algorithm runs very fast (within

few seconds) but the 3D graph cut algorithm takes about a minute to execute because of its large size. A potential direction of future research would be to use more computationally efficient flow algorithms as proposed by Boykov and Kolmogorov [21]. Last but not the least, we plan to extended our current approach for detecting multiple fractures.

6.8 References

[1] B.O. Ogundare, A. Bonnick and N. Bayley, "Pattern of Mandibular Fractures in an Urban Major Trauma Center", *J. of Oral and Maxillofac. Surg.*, vol. 61, no. 6, pp. 713-718, June 2003.

[2] L.R. Ford, Jr. and D.R. Fulkerson, "Maximum Flow Through a Network", *Canad. J. Math.* vol. 8, pp. 399-404, 1956.

[3] Y. Boykov, O. Veksler and R. Zabih, "Fast Approximate Energy Minimization via Graph Cuts", *IEEE Trans. Pattern Anal. Mach. Intell.*, vol. 23, no. 11, pp. 1222 - 1239, Nov. 2001.

[4] Y. Boykov and M.P. Jolly, "Interactive Graph Cuts for Optimal Boundary & Region Segmentation of Objects in N-D Images", in *Proc. of IEEE Int. Conf. on Computer Vision (ICCV)*, Vancouver, Canada, pp. 105 - 112, July 2001.

[5] N. Xu, R. Bansal and N. Ahuja, "Object Segmentation Using Graph Cuts Based Active Contours", in *Proc. of IEEE Int. Conf. on Computer Vision Pattern Recognition (CVPR)*, Madison, WI, pp. 46 - 53, July 2003.

[6] D. Freedman and T. Zhang, "Interactive Graph Cut Based Segmentation With Shape Priors", in *Proc. of IEEE Int. Conf. on Computer Vision Pattern Recognition (CVPR)*, San Diego, CA, pp. 755 - 762, July 2005.

[7] G. Funka-Lea, Y. Boykov, C. Florin, M.P. Jolly, R. Moreau-Gobard, R. ramaraj and D. Rinck, "Automatic Heart Isolation for CT Coronary Visualization Using Graph-Cuts",

in *Proc. of IEEE Int. Symp. of Biomedical Imaging*, Arlington, VA, pp. 614 - 617, April 2006.

[8] Z. Song, N. Tustison, B. Avants and J. Gee, "Adaptive Graph Cuts with Tissue Priors for Brain MRI Segmentation", in *Proc. of IEEE Int. Symp. of Biomedical Imaging*, Arlington, VA, pp. 762 - 765, April 2006.

[9] Y. Boykov and M.P. Jolly, "Graph Cuts and Efficient N-D Image Segmentation", *Int. J. Comp. Vis.*, Vol. 70, No. 2, pp. 109 - 131, 2006..

[10] T. Ozanian and R. Phillips, "Image Analysis for Computer-Assisted Surgery of Hip Fractures", *Med. Image Anal.*, vol. 4, no. 2, pp. 137 - 159, June 2000.

[11] D. W. H. Yap, Y. Chen, W. K. Leow, T. S. Howe, and M. A. Png", "Detecting Femur Fractures by Texture Analysis of Trabeculae, in *Proc. of ICPR*, Cambridge, UK, pp. 730-733, August 2004.

[12] M. Syiam, M.A. El-Aziem and M. El-Mensshawy, "Adgen: Adaptive Interface Agent for X-Ray Fracture Detection", *Internat. J. of Comput. and Inform. Sci.*, vol. 2, no. 3, pp. 143 - 148, 2004.

[13] M. Donnelley and G. Knowles, "Automated Bone Fracture Detection", in *Proc. of SPIE Medical Imaging*, San Diego, CA, pp. 955 - 966, February 2005.

[14] V. Lum, W. Leow, Y. Chen, T. Howe and M. Png, "Combining classifiers for bone fracture detection in X-ray images", in *Proc. of IEEE ICIP*, Genoa, Italy, pp. 1149 - 1152, September 2005.

[15] Y Jia and Y Jiang, "Active Contour Model with Shape Constraints for Bone Fracture Detection, in *Proc. of IEEE CGIV*, Sydney, Australia, pp. 90-95, July 2006.

[16] A.S. Chowdhury, S.M. Bhandarkar, G. Datta and J.C. Yu, "Automated Detection of Stable Fracture Points In Computed Tomography Image Sequences", in *Proc. of IEEE ISBI*, Arlington, VA, pp. 1320 - 1323, April 2006.

[17] A.S. Chowdhury, A. Bhattacharya, S.M. Bhandarkar, G.S. Datta, J.C. Yu and R. Figueroa, "Hairline Fracture Detection using MRF and Gibbs Sampling", *Proc. of Eighth IEEE Wkshp. on Applications of Computer Vision (WACV)*, Austin, TX, 2007, p. 56.

[18] T.H. Cormen, C.E. Leiserson, R.L. Rivest and C. Stein, *Introduction to Algorithms*, MIT Press, 2001.

[19] L.R. Ford, Jr. and D.R. Fulkerson, *Flows In Networks*, Princeton University Press, 1962.

[20] P. V. Giannoudis and H. Dinopoulos, Current concepts of the inflammatory response after major trauma: an update, *Injury*, vol. 36, no. 1, pp. 229-230, Jan. 2005.

[21] Y. Boykov and V. Kolmogorov, "Fast Approximate Energy Minimization via Graph Cuts", *IEEE Trans. Pattern Anal. Mach. Intell.*, vol. 26, no. 9, pp. 1124 - 1137, Sept. 2004.

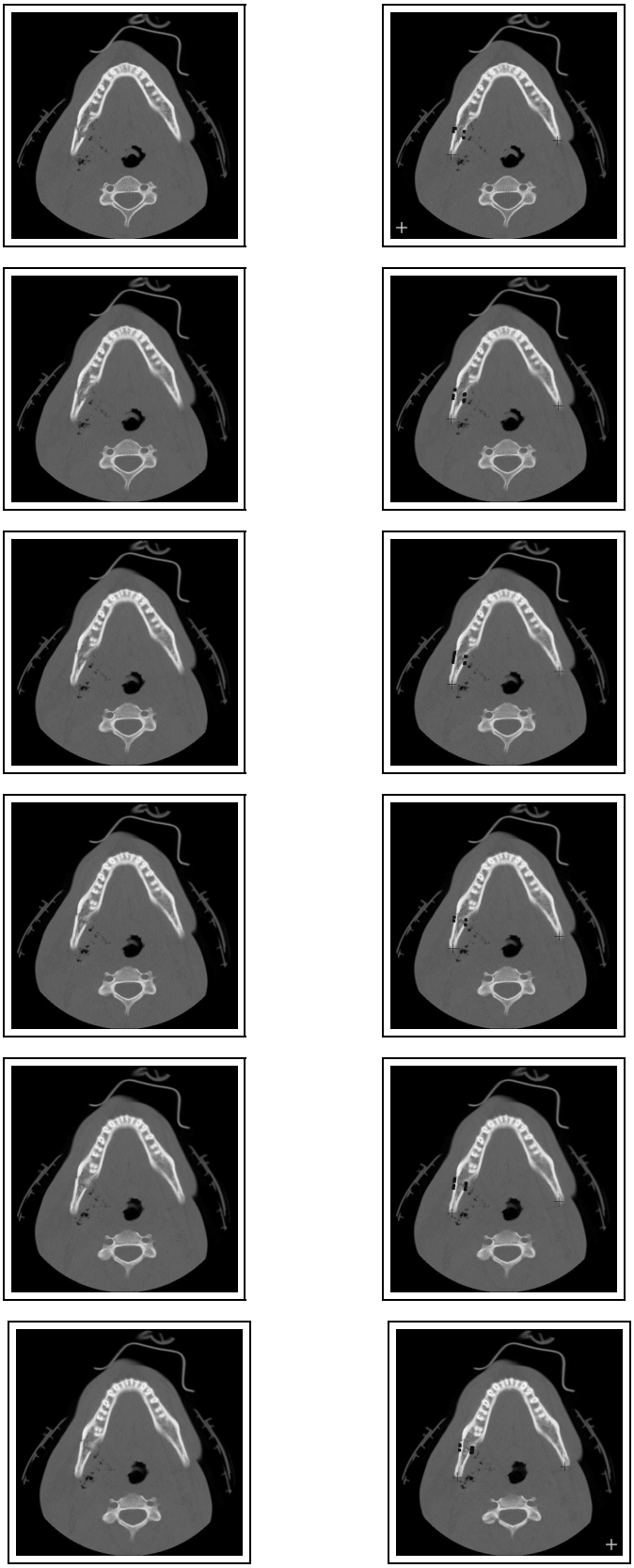

Figure 6.6: Slicewise Fracture detection of a Mandible using 3D graph cut. The first column shows the input and the second column shows the output with identified sources, sinks, hypersource, hypersink and fractures

Chapter 7

Conclusions and Future Research Directions

7.1 Chapter Organization

In this final chapter, we will first summarize what we have achieved thus far. The second section talks about the interdisciplinary research perspective, we have undertaken throughout this work and highlights our contributions in the general area of computer vision-pattern recognition. We end this chapter with a third section, where scope and directions of future research are presented. Note that each of the last five chapters have a separate section on "Conclusions and Future Scope". This chapter is written more from the viewpoint of providing a synopsis of our work, than presenting an aggregation of the individual chapterwise conclusions. A similar approach is taken for outlining the future research directions. This means, we will only state the major future research directions here and for more details, an interested reader is referred to the individual "Conclusions and Future Scope" sections of the last five chapters.

7.2 Summary

The research started with an aim of solving two challenging biomedical imaging problems, namely virtual mandibular reconstruction and computer aided mandibular fracture detection. In case of single fracture reconstruction, we used maximum cardinality minimum weight bipartite graph matching for the closest set computation in the ICP algorithm [1]; proposed a hybrid DARCES-ICP algorithm [2]; employed fuzzy set and surface curvatures to improve reconstruction accuracy [3]; used automorphism for cycle graphs and geometric constraints to have a better initialization for the ICP algorithm [4] and explored anatomical symmetry and biomechanical stability of the human mandible to have a overall better reconstruction

[5]. An extended version of the work presented in [1] and [2] appeared in [6] while a more in-depth version of [5] is currently under submission [7]. For the multi-fracture reconstruction, maximum weight graph matching is used to solve the problem of identification of opposable fracture surfaces in polynomial time. A suitable score matrix, using Hausdorff distance and contour curvature, is designed as an input to the graph matching algorithm and Tanimoto Coefficient based volumetric matching is used to monitor the progress of reconstruction. A preliminary version of the work appeared in [8] and a more thorough version is currently under preparation [9].

MRF-MAP approach is used for target pattern generation and fracture detection in case of a minor/hairline fracture. The research results were initially published in [10] and an extended version with strictly Hierarchical Bayesian image restoration framework and stochastic degradation matrix is currently under review [11]. Major/well-displaced fractures were detected using traditional scale-space theory of corner detection followed by use of Kalman Filter in a Bayesian Inference paradigm. A preliminary version of the work appeared in [12] and a more detailed version is also under review [13]. Maximum Flow-Minimum Cut algorithm is used to detect both major and minor fractures and the results are found to be more promising in the case of minor/hairline fractures. The research results are to be reported soon [14].

This research has already resulted in eight international conference/symposium/workshop papers and one international journal paper. Two more papers are currently under review and three additional papers are under preparation for submission, all in international journals. Please see the bibliography section of this chapter for details about the publications.

7.3 Interdisciplinary Research Perspective and Beyond

As mentioned in the beginning, the two practical problems of *in silico* reconstruction and fracture detection have deep underlying theoretical/mathematical interests. This led to the exploration of different domains like Statistics, Graph Theory and some Applied Mathematics to obtain appropriate solutions. Use of concepts/algorithms from these diverse disciplines

resulted in the following contributions to the general computer vision-pattern recognition research:

1. proposition of a hybrid DARCES-ICP algorithm (in the context of single fracture reconstruction)

2. alternative way of generation of multiple initial states for the ICP algorithm using concepts of Graph Automorphism (in the context of single fracture as well as multi-fracture reconstruction)

3. use of Maximum Cardinality Minimum Weight Bipartite Graph Matching algorithm to solve the correspondence problem in the ICP algorithm (in the context of single fracture as well as multi-fracture reconstruction)

4. use of Maximum Weight Graph Matching algorithm for solving a 3D jigsaw puzzle problem (in the context of multi-fracture reconstruction)

5. solving an image restoration problem with a partially unknown local stochastic degradation using a MRF-MAP based approach(in the context of target pattern generation for hairline/minor fractures)

6. specification of a reliable zone for spatial consistency using Bayesian Credible Sets (in the context of detecting stable fracture points for major fractures)

7. modeling a fracture, which is essentially a discontinuity, as a Minimum Cut in the Ford-Fulkerson's Maximum Flow algorithm (in the context of fracture detection, mainly for the minor fractures)

7.4 Future Research

We have been successful in predicting accurate transformation for bringing the broken mandibular bone fragments under registration. One major direction of future work could be use of a robotic arm to perform the actual surgery. The full process could be monitored by an experienced surgeon. Thus, we can substantially increase the degree of automation in

the entire surgical process with still a human in the loop. Another important research could be along the development of an anatomical model of the human mandible and use of this model guided feedback for further improvement of the overall virtual reconstruction.

We have applied different techniques for detecting minor/hairline and major/well-displaced fractures. It is found that MRF-MAP based method worked only for the class of minor fractures, traditional corner detection techniques performed only for the class of major fractures and max-flow min-cut based approach gave more promising results for the minor fractures. One major challenge is to design an unified scheme for identifying all types of fractures. Another problem is the following: for any given CT image sequence, consisting of several slices, the fractured mandible appears in only a few. In this work, we have manually identified these sets of slices containing the fractured mandible. Our fracture detection methods were then applied to accurately identify the fracture in these particular sets of slices. In order to make the detection process substantially more automated, one can first use some content based image retrieval (CBIR) strategies with shape and intensity information of a mandible to separate out the set of image slices containing one/more fracture(s) and then apply the proposed fracture detection techniques.

7.5 References

[1] S.M. Bhandarkar, A.S. Chowdhury, Yarong Tang, Jack Yu and E.W. Tollner, "Computer Vision for Reconstructive Plastic Surgery", *Proc. of First Int. Conf. on Communication, Devices and Intelligent Systems (CODIS)*, Calcutta, India, Jan. 2004, pp. 604 - 607.

[2] S.M. Bhandarkar, A.S. Chowdhury, Yarong Tang, Jack Yu and E.W. Tollner, "Surface Matching Algorithms for Computer Aided Reconstructive Plastic Surgery", *Proc. of Second IEEE Int. Symp. on Biomedical Imaging (ISBI)*; Arlington, VA, Apr. 2004, pp. 740 - 743.

[3] S.M. Bhandarkar, A.S. Chowdhury, E.W. Tollner, J.C. Yu, E.W. Ritter and A. Konar, "Surface Reconstruction for Computer Vision-based Craniofacial Surgery", *Proc. of Seventh IEEE Int. Workshop on Applications of Computer Vision (WACV)*; pp. 257 - 262;

Breckenridge, CO, Jan. 2005.

[4] A.S. Chowdhury, S.M. Bhandarkar, R.W. Robinson and J.C. Yu, "Novel Graph Theoretic Enhancements To ICP-Based Virtual Craniofacial Reconstruction", *Proc. of Fourth IEEE Int. Symposium on Biomedical Imaging (ISBI)*; pp. 1136 - 1139; Arlington, VA, Apr. 2007.

[5] A.S. Chowdhury, S.M. Bhandarkar, E.W. Tollner, G. Zhang, J.C. Yu and E. Ritter, "A Novel Multifaceted Virtual Craniofacial Surgery Scheme using Computer Vision", *Proc. of Computer Vision for Biomedical Image Applications: Current Techniques and Future Trends, an ICCV Workshop (CVBIA)*; Y Liu, T. Jiang and C. Zhang (Eds.), LNCS 3765, pp. 146 - 159; Beijing, China, Oct. 2005.

[6] S.M. Bhandarkar, A.S. Chowdhury, Yarong Tang, Jack Yu and E.W. Tollner, "Computer Vision Guided Virtual Craniofacial Reconstruction", *Computerized Medical Imaging and Graphics (CMIG)*, 2007. (in press)

[7] A.S. Chowdhury, S.M. Bhandarkar, E.W. Tollner and J.C. Yu, "A Two-phase Virtual Single -fracture Mandibular Reconstruction Scheme using Surface Matching, Shape Symmetry and Biomechanical Stability", (under preparation).

[8] A.S. Chowdhury, S.M. Bhandarkar, R.W. Robinson and J.C. Yu, "Virtual Craniofacial Reconstruction from Computed Tomography Image Sequences Exhibiting Multiple Fractures", *Proc. of Thirteenth IEEE Int. Conf. on Image Processing (ICIP)*; pp. 1173 - 1176; Atlanta, GA, Oct. 2006.

[9] A.S. Chowdhury, S.M. Bhandarkar, R.W. Robinson and J.C. Yu, "A Virtual Multifracture Mandibular Reconstruction Scheme based on Computer Vision and Graph Matching", (under preparation).

[10] A.S. Chowdhury, A. Bhattacharya, S.M. Bhandarkar, G.S. Datta, J.C. Yu and R. Figueroa, "Hairline Fracture Detection using MRF and Gibbs Sampling", *Proc. of*

Eighth IEEE Wkshp. on Applications of Computer Vision (WACV), Austin, TX, 2007, p. 56.

[11] A.S. Chowdhury, A. Bhattacharya, S.M. Bhandarkar, G.S. Datta and J.C. Yu, "Hairline Fracture Detection and Target Pattern Generation using MRF and Bayesian Image Restoration", submitted to *IEEE Transactions on Medical Imaging*.

[12] A.S. Chowdhury, S.M. Bhandarkar, G. Datta and J.C. Yu, "Automated Detection of Stable Fracture Points In Computed Tomography Image Sequences", *Proc. of Third IEEE Int. Symposium on Biomedical Imaging (ISBI)*; pp. 1320 - 1323; Arlington, VA, Apr. 2006.

[13] A.S. Chowdhury, S.M. Bhandarkar, G. S. Datta and J.C. Yu, "Stable Fracture Point Detection in Computed Tomography Image Sequences using Bayesian Inference", submitted to *Pattern Recognition*.

[14] A.S. Chowdhury, S.M. Bhandarkar, R.W. Robinson and J.C. Yu, "Mandibular Fracture Detection using Max-Flow Min-Cut", (under preparation).

Appendix A

Graphical User Interface

A.1 Design Considerations

We have developed a Graphical User Interface (GUI), which can be used both for surgical training and surgical planning. The GUI is built on top of ImageJ, a public domain software developed by NIH for performing various image processing tasks in Java [1]. We named our GUI InSilicoSurgeon (©University of Georgia). Good interface design principles [2] were followed in the development process. Various techniques of fracture detection as well as reconstruction are embedded in corresponding buttons. Considerable importance has been given to various factors such as the orientation of buttons, size of buttons, font-size on the titles of the buttons *etc.* The use of color in the GUI design is intentionally restricted only to gray and black considering the average age group of the users i.e. the surgeons in the present case.

A.2 The Functionalities

As mentioned in the previous section, the GUI consists of several buttons. We categorized a total of 27 buttons into 9 different sections with 3 buttons in each division. A snapshot of the GUI is given in figure (A.1).

In this section, a brief description of each section along with its buttons are given:

1. Single Frac. Recons. (Phase-I): This section is devoted to surface matching algorithms for single fracture reconstruction and also marks the first phase of the two-phase reconstruction process. It consists of following three buttons:

   (a) DARCES: Upon clicking this button, the DARCES algorithm will be executed

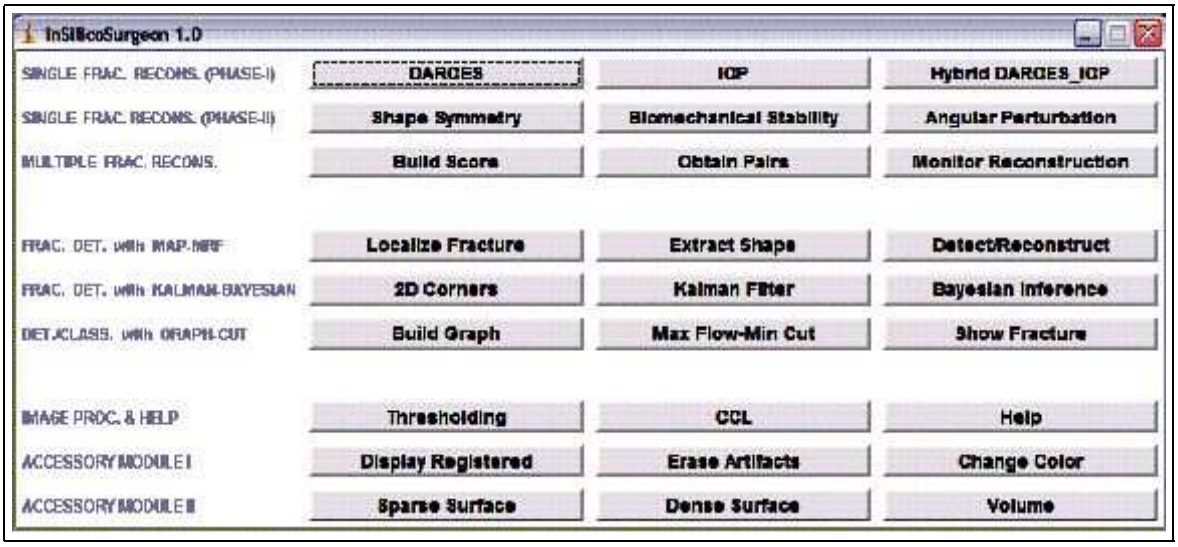

Figure A.1: A snapshot of InSilicoSurgeon: our GUI for the surgeons

(b) ICP: Upon clicking this button, the ICP algorithm will be executed

(c) Hybrid DARCES-ICP: Upon clicking this button, the hybrid DARCES-ICP algorithm will be executed

2. Single Frac. Recons. (Phase-II): This section is for the second phase of the two-phase reconstruction process. It has the following three buttons:

(a) Shape Symmetry: Upon clicking this button, one can obtain a quantitative measure of symmetry when no angular perturbation is applied

(b) Biomechanical Stability: Upon clicking this button, one can obtain a quantitative measure of the biomechanical stability (in terms of surface area) when no angular perturbation is applied

(c) Angular Perturbation: Upon clicking this button, the value of composite reconstruction metric (comprising surface matching, shape symmetry and biomechanical stability) will be obtained for the unperturbed and the best (from a series of) perturbed state

3. Multiple Frac. Recons.: This section allows a surgeon to perform the virtual reconstruction from multiple fractures. The three buttons in this section perform the following tasks:

   (a) Build Score: The scores for the fracture surfaces get computed on clicking this button and a score matrix is generated in the process

   (b) Obtain Pairs: Appropriate sets of opposable fracture surface pairs are generated on clicking this button

   (c) Monitor Reconstruction: This button can be used to monitor the step-by-step reconstruction of the broken fragments. After every two fragments are registered, one can check the correctness by clicking this button.

4. Frac. Det. with MAP-MRF: This section is dedicated to fracture detection and target pattern generation for minor/hairline fractures. The three buttons carry out the following functions:

   (a) Localize Fracture: On clicking this button, the mandibular fracture will be localized within a small geometric area

   (b) Extract Shape: With this button, an user can extract the shape of the fractured contours within the specified area

   (c) Detect/Reconstruct: This button will highlight the fracture and will also show a reconstructed jaw (based on MAP estimate)

5. Frac. Det. with Kalman-Bayesian: With the three buttons in this section, a surgeon will be able to detect the fracture points in case of major/well-displaced fractures. The buttons perform the following tasks:

   (a) 2D corners: On clicking this button, a set of potential fracture points (some of which will be discarded later) will be displayed

   (b) Kalman Filter: With this button, the Kalman Filter will be executed to give a set of predicted fracture points

(c) Bayesian Inference: This button will display the spatially consistent and anatomically correct corners (based on Bayesian Inference)

6. Frac. Det. with Graph Cut: This section enables a surgeon to detect fractures using Maximum Flow - Minimum Cut algorithm. The buttons here execute the following designated tasks:

   (a) Build-Graph: On clicking this button, the graph for the max flow-min cut algorithm is built

   (b) Max Flow-Min Cut: On clicking this button, the Max Flow-Min Cut algorithm will be executed on the already constructed graph

   (c) Show Fracture: This button will display the fracture (which are vertices of the graph constituting the edges with minimum cut)

7. Image Proc. & Help: This section is necessary to perform some basic image processing tasks. It has the following buttons:

   (a) Thresholding: Upon clicking this button, simple or entropy based thresholding methods will be executed to start segmenting human mandible fragments

   (b) CCL: Upon clicking this button, the Connected Component Labeling algorithm in conjunction with area based filtering will run to complete the segmentation process of human mandible fragments

   (c) Help: A user manual will be opened on clicking this button, which would describe the operational details of the entire GUI. This user manual is still under construction.

8. Accessory Module I: This section serves as an accessory module and is needed at various times during the detection and reconstruction process. The three buttons here are:

   (a) Display Registered: The broken fragments will be actually registered upon clicking this button. For example when the user clicks on ICP algorithm followed by this

button, the broken fragments will be registered according to the transformation predicted by the ICP algorithm and so on.

(b) Erase Artifacts: The user has the flexibility to manually remove some undesired artifacts using this button.

(c) Change Color: The user can change the color of some component using this button. This can be used for the purpose of better visualization *etc.*

9. Accessory Module II: This section deals with various types of data extraction. The fracture surface data are used as the inputs to the surface matching algorithms. The volume data for the broken fragments are necessary for volumetric checking during the monitoring process of the multi-fracture reconstruction. The buttons are as follows:

(a) Sparse Surface: This button will enable the user to extract the individual fracture points on the fractured contours, which upon aggregation form the sparse dataset for a fracture surface.

(b) Dense Surface: This button will enable the user to extract all the intervening datapoints on a contour between the actual fracture points, which upon aggregation form the dense/complete dataset for a fracture surface.

(c) Volume: Upon clicking this button, the volume data for a bone fragment is obtained. Unlike a fracture surface, which can be either sparse or dense/complete, the volume data is always dense/complete.

Note that a surface matching algorithm runs faster with a sparse surface data as compared to a dense/complete surface data. On the contrary, complete fracture surface data gives more insights to the nature of a fracture surface over that of the sparse surface data. We are about to replace the manual data extraction process by the fracture data obtained from corner detection followed by the Kalman filter-Bayesian Inference procedure. Some other modifications to the present GUI will involve buttons for the Geometric algorithm, hybrid Geometric-ICP algorithm, Fuzzy Sets and Surface Curvature based pixel information extraction *etc.*

A.3 References

[1] W.S. Rasband, "ImageJ", *U. S. National Institutes of Health*, Bethesda, Maryland, USA, http://rsb.info.nih.gov/ij/, 1997-2006.

[2] Y. Rogers, H. Sharp and J. Preece, *Interaction Design beyond human-computer interaction*, John Wiley & Sons., 2002.